Title: Synapse weakening-induced caspase-3 activity confers specificity to microglia-mediated synapse elimination

Authors: Zhou Yu[1,2†*], Andrian Gutu[1†], Namsoo Kim[1], Erin K. O'Shea[1*]

Affiliations:

[1]Janelia Research Campus, Howard Hughes Medical Institute, Ashburn, VA, USA.

[2]Current address: Brigham and Women's Hospital, Harvard Medical School, Boston, MA, USA.

[†]These authors contributed equally.

[*]Correspondence: zyu3@bwh.harvard.edu, osheae@hhmi.org.

Abstract: During brain development, synapses are initially formed in excess and are later eliminated in an activity-dependent manner, with weak synapses being preferentially removed. Previous studies identified glia as mediators of synapse removal, but it is unclear how glia specifically target weak synapses. Here we show that, in the developing mouse visual pathway, inhibiting synaptic transmission induces postsynaptic activation of caspase-3. Caspase-3 is essential for synapse elimination driven by both spontaneous and experience-dependent neural activity. Synapse weakening-induced caspase-3 activation determines the specificity of synapse elimination mediated by microglia but not astrocytes. Furthermore, in a mouse model of Alzheimer's disease, caspase-3 deficiency protects against synapse loss induced by amyloid-β deposition. Our results reveal caspase-3 activation as a key step in activity-dependent synapse elimination during development and synapse loss in neurodegeneration.

Main Text:

Synapse elimination is the process in which excess synapses formed early during brain development are subsequently eliminated to form mature circuits (*1-3*). A key feature of synapse elimination is that the outcome critically depends on both spontaneous and experience-driven neural activity, and less active synapses are preferentially removed (*2, 4, 5*). Previous studies have established that microglia and astrocytes, two major glial cell types of the brain, engage in synapse engulfment by using phagocytic receptors to detect 'eat-me' signals displayed on synapses (*6-14*). Although both microglia- and astrocyte-mediated synapse elimination are known to be activity-dependent (*7, 10*), it is unclear how the intrinsic strength of a synapse is converted into external molecular cues that can be recognized by glial cells to guide the selective removal of weaker synapses. A recent study proposed a molecular mechanism for activity-dependent synapse elimination in which the JAK2-STAT1 pathway is activated in inactive callosal projection neurons and regulates the removal of synapses and axons (*15*). However, the JAK-STAT pathway canonically functions through transcriptional regulation (*16*), which affects entire cells. If not all synapses made by a neuron are destined for removal (*3*), activation of the JAK2-STAT1 pathway alone may not provide sufficient elimination specificity. Therefore, other unidentified, locally-effective mechanisms likely exist that confer elimination specificity at the synapse level.

Caspase-3 is a protease crucial for the execution of apoptosis (*17*). In hippocampal neurons, transient activation of caspase-3 is required for long-term depression (LTD), a form of synaptic plasticity that induces long-lasting decreases in synaptic strength (*18*). Caspase-3 activation is also known to trigger the display of 'eat-me' signals on apoptotic cells, facilitating their clearance by phagocytes through the engagement of phagocytic

47 receptors (*19, 20*). These findings led us to hypothesize that caspase-3 may link synapse
48 weakening with glial recognition and subsequent synapse removal. Although caspases
49 were previously implicated in dendrite pruning in metamorphosis, degeneration-like axon
50 elimination, and the regulation of hippocampal spine density (*21-24*), the role of caspase-
51 3 in synapse elimination in response to neural activity was not clear. In this work, we
52 identify caspase-3 as a pivotal molecule that is activated in postnatal development in
53 dendritic compartments upon synaptic weakening and is necessary to direct microglia to
54 selectively eliminate weak synapses. Furthermore, we discovered that caspase-3
55 deficiency protects against amyloid-β-induced synapse loss in a mouse model of
56 Alzheimer's disease, highlighting its significance not only in development synapse
57 elimination but also in adult neurodegenerative diseases.
58
59 **Synapse inactivation induces postsynaptic caspase-3 activity**
60 We chose the mouse retinogeniculate visual pathway as a model system to study
61 synapse elimination (*25*). In mice, retinal ganglion cells (RGCs) in each eye send out
62 axons to form retinogeniculate synapses with relay neurons in the dorsal lateral
63 geniculate nuclei (dLGN) of the thalamus on both sides of the brain (Fig. S1) (*25*). The
64 majority of RGC axons from each eye innervate the contralateral (on the side opposite to
65 the originating eye) dLGN while a smaller fraction innervate the ipsilateral (on the same
66 side as the originating eye) dLGN (Fig. S1) (*25*). Regions in each dLGN innervated by the
67 two eyes initially overlap but later segregate into eye-specific territories (Fig. S1). This
68 segregation process is a hallmark of retinogeniculate pathway development at the

69 morphological level and depends on synapse elimination and spontaneous RGC activity
70 (*25-27*).

71 To investigate the role of caspase-3 in activity-dependent synapse elimination, we
72 first needed to establish a method that could manipulate the strength of a selective subset
73 of retinogeniculate synapses. For this purpose, we used adeno-associated-virus (AAV) to
74 deliver a construct expressing tetanus toxin light chain (TeTxLC) under the control of the
75 neuron-specific human synapsin promoter (AAV-hSyn-TeTxLC) (Fig. 1A) (*28*). *In utero*
76 intraocular injection of AAV-hSyn-TeTxLC at embryonic day 15 (E15) leads to TeTxLC
77 expression in RGCs by the time of birth, blocking neurotransmitter release at
78 retinogeniculate synapses by cleaving synaptobrevin (*28, 29*). As anterograde tracers
79 and controls, we used AAV to express a fluorescent protein (mTurquiose2, eGFP, or
80 tdTomato, depending on the experiment) either alone or together with TeTxLC (Fig. 1A).
81 To validate our method, we injected AAV-hSyn-TeTxLC into the right eye of wildtype E15
82 embryos and analyzed eye-specific territories at postnatal day 8 (P8) (see Fig. S2 and
83 text associated with Fig. 3 for details of the analysis), when the segregation process is
84 largely complete (*25*). Consistent with previous results (*26, 27*), inactivating right eye-
85 associated retinogeniculate synapses led to contraction of right eye-specific territories
86 and expansion of left eye-specific territories relative to control animals (Fig. S3A and S3B).
87 In addition, segregation of eye-specific territories in TeTxLC-injected mice was defective
88 (Fig. S3C and S3D), confirming that our method potently inactivated synapses and
89 perturbed activity-dependent refinement of the retinogeniculate pathway.

90 Is caspase-3 activated in response to synapse weakening? To address this
91 question, we injected AAV-hSyn-TeTxLC into the right eyes of E15 embryos and looked

92 for caspase-3 activation in dLGNs of TeTxLC-injected mice at the age of P5 (a time when
93 synapse elimination is most active) (Fig. 1A) (*7, 25*). TeTxLC expression causes a
94 widespread inactivation of retinogeniculate synapses and enhances potential synapse
95 inactivation-induced caspase-3 activity. We measured caspase-3 activity by detecting the
96 cleaved and active form of caspase-3 through immunohistochemistry (*17*). If synapse
97 inactivation leads to caspase-3 activation, we would expect higher levels of caspase-3
98 activity in dLGNs with more inactivated synapses (Fig. 1A). In agreement with this
99 hypothesis, normalized caspase-3 activity in the left dLGN of right eye TeTxLC-injected
100 animals (Fig. 1B and 1E) was significantly higher compared to that in the right dLGN of
101 right eye TeTxLC-injected animals (Fig. 1C and 1E) and compared to that in the left dLGN
102 of Turq-injected control animals (Fig. 1D and 1E). We did not detect differences in
103 caspase-3 activity between the right dLGN of right eye TeTxLC-injected animals and the
104 dLGN of control animals (Fig. 1C, 1D and 1E), presumably due to low levels of synaptic
105 inactivation in the former and/or insufficient signal-to-background ratio. Reassuringly,
106 caspase-3 activities in left and right dLGN of control animals were comparable (Fig. 1E),
107 suggesting that surgical manipulation and viral transduction did not contribute to caspase-
108 3 activation. These findings support the model that inactivation of retinogeniculate
109 synapses induces caspase-3 activation.

110 Does inactivation of retinogeniculate synapses activate caspase-3 pre-synaptically
111 in RGCs or post-synaptically in dLGN relay neurons? Caspase-3 activity in dLGNs of
112 TeTxLC-injected mice was present either as discrete, punctate signals (Fig. 1F) or as
113 staining of the entire cell (Fig. 1B and Fig. S4Bi-iii). Both types of signals were more
114 abundant in dLGNs with strong synapse inactivation than in control dLGNs (Fig. 1B, 1D

115 and 1F). Intriguingly, punctate caspase-3 activity was not found within TeTxLC-expressing
116 RGC axons (Fig. 1G). Instead, punctate caspase-3 activity closely juxtaposed inactivated
117 axon terminals (Fig. 1G) and co-localized with a dendritic marker, MAP2 (Fig. S4A). In
118 the case where caspase-3 was activated in entire cells, the cells were positive for nuclear
119 NeuN (Fig. S4C) and possessed relatively large round somas and multipolar dendritic
120 arbors (Fig. S4Bi-iii), all of which are characteristics of dLGN relay neurons (*30, 31*).
121 These observations suggest that caspase-3 activation triggered by synapse inactivation
122 occurs predominantly in the dendritic compartments of dLGN relay neurons that are
123 postsynaptic to the inactivated synapses. It is important to note that the whole-cell
124 caspase-3 activation observed in TeTxLC-inactivated dLGNs is likely a consequence of
125 strong synapse inactivation and is not a normal developmental phenomenon (compare
126 Fig. 1B and 1D). Consistent with this idea, we observed a transitional state of caspase-3
127 activation where multiple dendrites of a relay neuron were positive for activate caspase-
128 3 without the cell body becoming apoptotic (Fig. S4Biv), suggesting that, in TeTxLC-
129 inactivated dLGNs, strong synapse inactivation causes excessive accumulation of
130 caspase-3 activity in dendrites and eventually leads to caspase-3 activation in entire relay
131 neurons, possibly through caspase-3 mediated feedback amplifications of the apoptosis
132 signaling cascade (*32*).
133

134 **Synapse inactivation-induced caspase-3 activation requires synaptic competition**

135 Is synapse inactivation-induced caspase-3 activity a result of synapse inactivation
136 *per se*, or is it a result of competition between inactive and active synapses? Previous
137 studies have either hyperactivated or inactivated RGCs in one of the two eyes while

138 leaving the other eye unperturbed (*26, 27*). In the scenario involving hyperactivation, both
139 the less active (unperturbed) and the more active (hyperactivated) eye had higher activity
140 than their counterparts in the scenario involving inactivation. However, in both
141 experiments, the dLGN territory of the less active eye contracted while that of the more
142 active eye expanded (*26, 27*), suggesting that relative, rather than absolute, synapse
143 strength determines the outcome of synapse elimination in the retinogeniculate pathway.
144 Consistent with this idea, a recent study demonstrated that elimination of inactive
145 synapses in callosal projections occurred only when other active synapses are present
146 (*28, 33*).

147 To test if synapse inactivation-induced caspase-3 activation requires synaptic
148 competition, we devised two conditions where either one (single inactivation) or both eyes
149 (dual inactivation) were injected with AAV-hSyn-TeTxLC (Fig. 2A). In single inactivation,
150 retinogeniculate synapses originating from different eyes have different strengths and
151 compete within each dLGN (Fig. 2A), whereas in dual inactivation, all retinogeniculate
152 synapses are inactivated and no competition occurs (Fig. 2A). We first confirmed that, in
153 accordance with previous findings (*26, 34*), inactivating RGCs in both eyes with TeTxLC
154 disrupted segregation of eye-specific regions (Fig. S5A-D). We then measured caspase-
155 3 activity in the single- or dual-inactivated dLGNs and in the control dLGN, where
156 retinogeniculate synapses were unperturbed (Fig. 2A). Intriguingly, while single
157 inactivation induced significantly higher levels of caspase-3 activity in the dLGN
158 compared to controls (Fig. 2B and 2C), active caspase-3 signal in the dual-inactivated
159 dLGN was not significantly different from the signal in the control dLGN (Fig. 2B and 2C)
160 and was significantly lower than that in the single-inactivated dLGN (Fig. 2B and 2C).

161 Although not reaching statistical significance, caspase-3 activity on average was still
162 higher in the dLGN in dual inactivation than in the control dLGN (Fig. 2C), possibly due
163 to incomplete inactivation of retinogeniculate synapses, or competition between
164 retinogeniculate synapses and synapses from other pathways, or additional mechanisms
165 that activate caspase-3 independently of synapse competition. These results suggest that
166 competition between active and inactive retinogeniculate synapses is required to induce
167 caspase-3 activity in dendritic compartments of dLGN relay neurons.
168

169 **Caspase-3 is required for segregation of eye-specific territories**

170 Is synapse inactivation-induced caspase-3 activity important for synapse
171 elimination in the retinogeniculate pathway? To address this question, we investigated
172 whether segregation of eye-specific dLGN territories is defective if caspase-3 activation
173 does not occur. As we were unable to find a Cre-expressing mouse line that satisfactorily
174 depletes caspase-3 in dLGN relay neurons, we used full-body caspase-3 deficient
175 (*Casp3*$^{-/-}$) mice (*35, 36*). These mice were backcrossed to congenicity on the C57Bl/6J
176 background and were viable, fertile, and did not exhibit overt abnormalities (*36*).

177 To measure segregation of eye-specific territories, we injected the eyes of
178 *Casp3*$^{+/+}$ and *Casp3*$^{-/-}$ littermate mice at P9 with fluorophore-conjugated cholera toxin
179 subunit B (CTB), using a different fluorophore for each eye. CTB molecules bind to
180 ganglioside molecules on RGC surfaces and anterogradely label RGC axon terminals
181 (*37*). At P10, when CTB labeling and eye-specific segregation were complete (*25, 38*),
182 we collected the brains and imaged eye-specific territories in each dLGN. By visual
183 inspection, eye-specific territories in *Casp3*$^{+/+}$ dLGNs overlapped minimally (Fig. 3A). By

184 contrast, *Casp3*$^{-/-}$ dLGNs showed clear defects in the separation of eye-specific territories
185 (Fig. 3B) (*39*). To quantify the overlap between eye-specific territories in an unbiased
186 manner, we applied a set of increasing thresholds to signals from both eyes (Fig. S2) (*38*).
187 We calculated the percentage overlap of eye-specific territories as the ratio between
188 dLGN area with above-threshold signals from both eyes and the total dLGN area (Fig. S2
189 and Fig. 3C). Percentage overlap in *Casp3*$^{-/-}$ dLGNs was consistently higher than that in
190 *Casp3*$^{+/+}$ dLGNs across all thresholds (Fig. 3C and D). Importantly, the fold difference and
191 statistical significance of the difference in percentage overlap between the two groups of
192 animals increased as the cutoff threshold increased (Fig. 3D), suggesting the defects
193 observed in *Casp3*$^{-/-}$ animals cannot be attributed to artifacts generated from background
194 noise.

195 As RGCs are known to undergo extensive apoptosis during the first week of
196 postnatal development (*40, 41*), we wondered if caspase-3 deficiency might block RGC
197 turnover and result in more RGC inputs in the dLGN, thereby confounding the overlap
198 analysis. To address this concern, we quantified the density of RGCs in whole-mount
199 retinae using a RGC marker, RBPMS (Fig. S6A) (*42*). Reassuringly, RGC densities in
200 retinae of *Casp3*$^{+/+}$ and *Casp3*$^{-/-}$ mice were not different (Fig. S6B), indicating that RGC
201 apoptosis still occurred at normal rates in the absence of caspase-3, presumably through
202 redundant mechanisms. Collectively, our findings suggest that caspase-3 is required for
203 normal segregation of eye-specific territories in dLGN.
204

205 **Caspase-3 is required for retinogeniculate circuit refinement**

206 Segregation of eye-specific territories in the mouse dLGN occurs prior to eye
207 opening (which happens at ~P13) and relies predominantly on spontaneous RGC activity
208 (*25*). After eye opening, sensory-dependent RGC activity drives a second phase of
209 refinement at the circuit level (*25*). At the time of eye opening, each dLGN relay neuron
210 receives numerous weak RGC inputs. With visual experience, a minority of these inputs
211 are strengthened while other weak inputs are eliminated, so that by P30 only a few
212 (typically ≤3) strong RGC inputs innervate each dLGN relay neuron (*25*).

213 To test if caspase-3 is required for visual experience-driven circuit refinement, we
214 prepared acute brain slices from P30 *Casp3*$^{+/+}$ and *Casp3*$^{-/-}$ littermate mice and
215 investigated the electrophysiological properties of retinogeniculate synapses (Fig. S7A)
216 (*43, 44*). We stimulated the optic tract while recording both AMPA receptor (AMPAR)- and
217 NMDA receptor (NMDAR)-mediated excitatory postsynaptic currents (EPSCs) in dLGN
218 relay neurons (Fig. S7A and Fig. 4A-B). Because each RGC axon has a distinct excitation
219 threshold, as we gradually increase the stimulation intensity on the optic tract, we recruit
220 individual RGC axons in a serial manner (Fig. S7A). Excitation of each RGC axon triggers
221 a step increase in the EPSC amplitude (Fig. S7A), allowing us to count the number of
222 steps in both AMPAR- and NMDAR-mediated response curves and infer the number of
223 RGC inputs on each relay neuron (Fig. 4C and S8A). In agreement with previous studies,
224 retinogeniculate circuits in *Casp3*$^{+/+}$ animals were refined, with dLGN relay neurons most
225 frequently receiving 2 strong RGC inputs, and the great majority of neurons receiving no
226 more than 3 inputs (Fig. 4A, 4C and S8A). In contrast, RGC input counts of dLGN relay
227 neurons in *Casp3*$^{-/-}$ animals followed a long-tailed distribution that was significant right-
228 shifted from that of *Casp3*$^{+/+}$ animals (Fig. 4C and S8A). The majority of *Casp3*$^{-/-}$ relay

229 neurons received more than 3 inputs (Fig. 4B-C and S8A), and many inputs elicited only
230 small increments in EPSC amplitude (Fig. 4B). To investigate whether the defects
231 observed in *Casp3*$^{-/-}$ animals could be due to general synaptic dysfunction, we compared
232 AMPAR- and NMDAR-mediated EPSCs in *Casp3*$^{+/+}$ and *Casp3*$^{-/-}$ animals and observed
233 no difference in maximum EPSC amplitude (Fig. S8B and S8C) or the ratio of the two
234 types of EPSCs (Fig. S8D). Additionally, we calculated fiber fraction (FF) as the ratio
235 between the first non-zero response (elicited by a single axon fiber) and the maximum
236 response in each dLGN relay neuron (Fig. S8E). FF increases as RGC inputs are
237 strengthened during development (*44*). We observed comparable FF values in *Casp3*$^{+/+}$
238 and *Casp3*$^{-/-}$ animals (Fig. S8E), which suggests that defective circuit refinement in
239 *Casp3*$^{-/-}$ animals was not due to lack of RGC input strengthening but instead an inability
240 to eliminate weak inputs.

241 An increased number of RGC axons innervating dLGN relay neurons in *Casp3*$^{-/-}$
242 mice should correspond to greater numbers of presynaptic release sites. To infer the
243 number of release sites, we stimulated the optic tract with a pair of stimuli in rapid
244 succession and measured the paired-pulse response ratio (PPR) in dLGN relay neurons
245 (Fig. S7B and Fig. 4D-E) (*43, 45*). In retinogeniculate synapses, the first stimulus
246 significantly depletes the readily releasable pool (RRP) of neurotransmitters and reduces
247 the response to the second stimulus, resulting in a small PPR (calculated as second
248 response over first response) (Fig. S7B) (*43, 45*). If there is an increase in the number of
249 release sites in *Casp3*$^{-/-}$ mice, we expect the RRP to expand, leading to a larger second
250 response and PPR (Fig. S7C) (*45*). Indeed, we found that the PPR was significantly
251 greater in *Casp3*$^{-/-}$ dLGN relay neurons than in controls (Fig. 4D-E), suggesting that the

252 inability to eliminate weak inputs resulted in an increase in the number of release sites
253 from RGC inputs in *Casp3*$^{-/-}$ mice. Taken together, our results demonstrate that caspase-
254 3 is required for experience-driven retinogeniculate circuit refinement. In the absence of
255 caspase-3, weak RGC inputs cannot be eliminated, and dLGN relay neurons remain
256 multiply innervated.
257
258 **Microglia-mediated synapse elimination depends on caspase-3**
259 Our results reveal activity-dependent caspase-3 activation at synapses as a key
260 molecular event that directs synapse elimination in the retinogeniculate pathway but do
261 not identify the cell types involved. Previous studies have demonstrated that both
262 microglia and astrocytes participate in synapse elimination by engulfing synaptic material
263 (*7, 10*). It is possible that caspase-3 activation at synapses might induce the display
264 apoptosis-related cell surface markers that can be recognized by microglia and astrocytes
265 for synapse elimination.
266 If microglia-mediated synapse elimination depends on caspase-3 activation, then
267 microglia in *Casp3*$^{-/-}$ mice should engulf less synaptic material. Similar to a previous study
268 (*7*), we utilized the *Cx3cr1-Gfp* transgenic mouse line to visualize microglia *in vivo.* In this
269 line, a *Gfp* transgene is expressed under the control of the native *Cx3cr1* promoter to
270 enable specific labeling of microglia in the brain (Fig. 5A) (*46*). As a proxy for labeling
271 retinogeniculate synapses, we labeled presynaptic RGC axon terminals by injecting
272 *Casp3*$^{+/-}$; *Cx3cr1-Gfp*$^{+/-}$ and *Casp3*$^{-/-}$; *Cx3cr1-Gfp*$^{+/-}$ littermate pups (*Casp3*$^{+/-}$ instead of
273 *Casp3*$^{+/+}$ mice were used to enable more efficient breeding) at the age of P4 with
274 fluorophore-conjugated CTB in the two eyes and harvested the brains at P5 (Fig. 5A) (*7*).

275 We used automatic segmentation to isolate volumes corresponding to microglia and RGC
276 axon terminals (Fig. 5B) from regions in the dLGN where RGC inputs from both eyes were
277 present (Fig. 5A). The presence of small soma and thin processes of microglia in *Casp3*$^{-}$
278 $^{/-}$; *Cx3cr1-Gfp*$^{+/-}$ mice indicates that caspase-3 deficiency did not result in microglial
279 activation (Fig. 5B), which is further validated by immunohistochemical analysis of
280 microglia in caspase-3 deficient mice (Fig. S9A-D). To quantify synapse engulfment, we
281 calculated the volume of labeled RGC terminals that were fully enclosed in each microglia
282 (Fig. 5C). As expected, we observed that microglia in *Casp3*$^{-/-}$; *Cx3cr1-Gfp*$^{+/-}$ mice
283 engulfed significantly less axonal material compared to those of *Casp3*$^{+/-}$; *Cx3cr1-Gfp*$^{+/-}$
284 littermates (Fig. 5B-C). The same trend was observed when RGC axon terminals
285 originating from the two eyes were analyzed separately (Fig. S10A-B), suggesting that
286 defects in microglia-mediated synapse engulfment in *Casp3*$^{-/-}$ mice affect inputs from both
287 eyes. As the engulfment capacity of microglia is limited by their size, we normalized the
288 volume of engulfed synaptic material in each microglia to the microglial volume (Fig. 5D).
289 Microglia in both groups of mice are comparable in size (Fig. S10C), and the defect in
290 synaptic engulfment observed in *Casp3*$^{-/-}$ mice persisted after normalization to microglial
291 volume (Fig. 5D). Our results demonstrate that microglia-mediated synapse elimination
292 depends on caspase-3.

293 Astrocytes utilize phagocytic receptors MerTK and Megf10 to eliminate synapses
294 (*10*). Both receptors have been implicated in the clearance of apoptotic cells (*47, 48*). We
295 asked whether caspase-3 activation is also required for astrocyte-mediated synapse
296 elimination. To visualize astrocytes, we used the *Aldh1l1-Gfp* transgenic mouse line,
297 where a *Gfp* transgene under the control of the promoter of *Aldh1l1* is specifically

298 expressed in astrocytes (Fig. S11A) (*49*). We again labeled RGC axon terminals in
299 *Casp3*$^{+/-}$; *Aldh1l1-Gfp*$^{+/-}$ and *Casp3*$^{-/-}$; *Aldh1l1-Gfp*$^{+/-}$ littermate mice with intraocular
300 injection of CTB conjugates (Fig. S11A). Astrocytes were present in the P5 dLGN at a
301 much higher density than microglia and possess very fine processes (Fig. S11A). To
302 ensure segmentation fidelity, we only analyzed astrocyte cell bodies and their proximal
303 processes (Fig. S11B). Unexpectedly, we found that the volume of axonal material
304 engulfed by astrocytes was comparable in the two groups of mice (Fig. S11C). On
305 average, astrocytes in caspase-3 deficient mice did engulf less axonal material (Fig.
306 S11C), but the effect size appears too small to be biologically relevant, and the statistical
307 significance was small considering that the sample size was large (Fig. S11C). The same
308 trend was observed when we normalized the volume of engulfed synaptic material to
309 astrocyte volume (Fig. S11D-E). It is possible that a more pronounced difference would
310 be observed if *Casp3*$^{+/+}$ mice were used for comparison. Nevertheless, the differential
311 response to caspase-3 deficiency between microglia- and astrocyte-mediated synapse
312 elimination raises the possibility that the two cell types may target distinct sets of
313 synapses for elimination (see discussion).
314

315 **Caspase-3 activation determines synapse elimination specificity**

316 Our data demonstrate that caspase-3 is activated at weak/inactive synapses, and
317 that microglia eliminate less synaptic material when caspase-3 activation is blocked.
318 Combining the two observations, we hypothesize that activity-dependent caspase-3
319 activation at synapses is a key molecular event that directs microglia to specifically

320 eliminate weaker synapses. This model predicts that in caspase-3 deficient mice,
321 microglia should lose the ability to preferentially target weaker synapses.

322 To test this model, we inactivated retinogeniculate synapses originating from right
323 eyes in *Casp3*$^{+/+}$ and *Casp3*$^{-/-}$ mice with AAV-hSyn-TeTxLC injections (Fig. 6A). A group
324 of control animals was included for each genotype that received AAV-hSyn-Turq injections.
325 We then labeled RGC axon terminals from both eyes with CTB conjugates in all animals
326 and analyzed microglia-mediated synapse engulfment (Fig. 6B-G). According to our
327 model, in TeTxLC-injected *Casp3*$^{+/+}$ mice, microglia should preferentially engulf inactive
328 retinogeniculate synapses originating from the right eye (Fig. 6A), whereas in TeTxLC-
329 injected *Casp3*$^{-/-}$ mice, synapses from the right and the left eye should be engulfed at
330 similar levels regardless of their strength (Fig. 6A). To quantitatively detect preferential
331 synapse engulfment by microglia, a comparison between TeTxLC-injected and control-
332 injected animals is necessary (Fig. 6B, C, and F). We first calculated the ratio between
333 the volume of right eye-originated RGC axon terminals and left eye-originated terminals
334 that were engulfed by each microglia. Then, by comparing this right-to-left engulfment
335 ratio computed in TeTxLC-injected and control-injected animals, preferential engulfment
336 of inactivated synapses from right eyes could be detected as higher engulfment ratios in
337 TeTxLC-injected animals (Fig. 6F). It is worth noting that microglia-related confounding
338 factors, such as possible alterations in microglia physiology due to caspase-3 deficiency
339 or surgical manipulations, cancel out when calculating engulfment ratios, allowing
340 information pertaining only to substrate preference to be isolated.

341 Consistent with previous studies (*7*), in *Casp3*$^{+/+}$ mice inactivation of
342 retinogeniculate synapses from the right eye led to enhanced microglia-mediated

343 engulfment of right eye-originated RGC axon terminals but not left eye-originated
344 terminals (Fig. S12A-B), resulting in a significant increase in right-to-left engulfment ratios
345 in microglia of TeTxLC-injected animals compared to control-injected animals (Fig. 6B, C,
346 and F). In contrast, engulfment ratios were similar between TeTxLC-injected and control-
347 injected *Casp3*$^{-/-}$ mice (Fig. 6D, E and G and Fig. S12C-D), suggesting that microglia
348 could no longer distinguish between strong and weak synapses in the absence of
349 caspase-3 activation. Summing the evidence obtained thus far, we propose the activity-
350 dependent caspase-3 activation is a crucial signaling event that integrates upstream
351 information about synaptic activity, takes place at weak/inactive synapses, and recruits
352 downstream microglia to eliminate synapses in an activity-dependent manner.
353

354 **Caspase-3 deficiency protects against amyloid-β-induced synapse loss**

355 Lastly, we wanted to test if caspase-3 regulates synapse loss in neurodegenerative
356 diseases through mechanisms analogous to its role in activity-dependent synapse
357 elimination. To this end, we focused on Alzheimer's disease (AD). AD is the most common
358 cause of dementia (*50*), and synapse loss is the strongest correlate of cognitive decline
359 in AD patients (*51*). Accumulation and deposition of oligomeric or fibril amyloid-
360 β (Aβ) peptide has been proposed to be the cause of neurodegeneration in AD (*50*).
361 Intriguingly, oligomeric Aβ impairs long-term potentiation (LTP) (*52*), and this suppression
362 of LTP requires caspase-3 activation (*53*). Additionally, caspase-3 activation has been
363 linked to early synaptic dysfunction in an AD mouse model (*54*).

364 To test if synapse loss in AD requires caspase-3, we utilized the APP/PS1 mouse
365 line, in which amyloid precursor protein (APP) and presenilin 1 (PS1) carrying mutations

366 associated with early-onset familial AD are overexpressed in CNS neurons (*55*). We
367 observed that female *App/Ps1*$^{+/-}$ mice developed amyloid deposits in the hippocampus
368 and cortex by 5 months (Fig. S13Aii), and the amyloid burden worsened by 6 months (Fig.
369 S13Aiii). In male *App/Ps1*$^{+/-}$ mice, amyloid deposits only became apparent at 6 months
370 and occurred at a lower level compared to age-matched females (Fig. S13Aiv-v). We
371 focused on analyzing *App/Ps1*$^{+/-}$ female mice in subsequent experiments to obtain robust
372 phenotypes. To quantify synapse loss, we labeled presynaptic and postsynaptic
373 compartments in the dentate gyrus of 6 month-old *App/Ps1*$^{-/-}$ and *App/Ps1*$^{+/-}$ littermates
374 by detecting synaptic vesicle protein 2 (SV2) and Homer1, respectively, and selected
375 multiple fields of interest per animal for imaging analysis while avoiding regions adjacent
376 to amyloid deposits (Fig. S14). We fitted ellipsoids to SV2 and Homer1 signals to identify
377 pre- and post-synaptic puncta and defined synapses as Homer1-SV2 punctum pairs that
378 were less than 300 nm apart (Fig. 7A). We observed that synapse density in *App/Ps1*$^{+/-}$
379 mice was significantly reduced compared to that in *App/Ps1*$^{-/-}$ littermate controls (Fig. 7A-
380 B), and that this reduction could be attributed to lower densities of both pre- and post-
381 synaptic puncta in *App/Ps1*$^{+/-}$ mice (Fig. S15A-B). We then crossed APP/PS1 mice to
382 caspase-3 deficient mice and quantified synapse density in 6 month-old *Casp3*$^{-/-}$;
383 *App/Ps1*$^{-/-}$ and *Casp3*$^{-/-}$; *App/Ps1*$^{+/-}$ littermate mice (Fig. S14). We observed that, in the
384 caspase-3 deficient background, overexpression of mutant APP and PS1 no longer
385 resulted in a reduction in the density of synapses (Fig. 7C-D) or pre-/post-synaptic puncta
386 (Fig. S15C-D), suggesting that caspase-3 activity is required for Aβ-induced synapse loss
387 in the APP/PS1 mouse model. Intriguingly, levels of amyloid deposition were comparable
388 between *App/Ps1*$^{+/-}$ and *Casp3*$^{-/-}$; *App/Ps1*$^{+/-}$ mice (Fig. S13Avi and B), and reactive

389 microglia were observed near amyloid deposits regardless of caspase-3 deficiency (Fig.
390 S16), indicating that protection conferred by caspase-3 deficiency against Aβ-induced
391 synapse loss might not require inhibition of amyloid accumulation or microgliosis. We also
392 investigated whether Aβ accumulation induced elevated levels of caspase-3 activity. We
393 analyzed 4, 5, and 6 month-old *App/Ps1*$^{-/-}$ and *App/Ps1*$^{+/-}$ mice but only observed robust
394 upregulation of caspase-3 activity in the dentate gyrus of a subset of 4 month-old
395 *App/Ps1*$^{+/-}$ mice (Fig. S17A-C). Upregulated caspase-3 activity in these mice remained in
396 a punctate pattern without inducing neuronal death (Fig. S17D-F). It is possible that Aβ
397 transiently induces caspase-3 activation in *App/Ps1*$^{+/-}$ mice, but stochasticity in the onset
398 and duration of such induction prevents reliable detection with our sample size and
399 temporal resolution. Overall, our results demonstrate caspase-3 as an important regulator
400 of Aβ-induced synapse loss and a potential therapeutic target for AD treatment.
401

402 ## Discussion:

403 **A model for caspase-3 dependent synapse elimination**

404 Our findings support a model where competition between strong/active synapses
405 and weak/inactive synapses in the retinogeniculate pathway triggers caspase-3 activation
406 in the postsynaptic compartments of weaker synapses. This activation signals microglia
407 to selectively eliminate these weaker synaptic connections, thereby facilitating the
408 establishment of mature circuits in the visual pathway.
409

410 **Mechanisms of activity-dependent caspase-3 activation**

411 In the experiment where we demonstrated activity-dependent caspase-3 activation,
412 we inactivated all retinogeniculate synapses from one eye to induce sufficiently high
413 caspase-3 activity that can be discerned from background. It is important to note that this
414 degree of inactivation is not typical for normal development. Consequently, caspase-3
415 activation in entire dLGN relay neurons observed in this experimental setting should not
416 be interpreted as a physiological outcome of activity-dependent synapse elimination. In
417 fact, apoptotic neurons were infrequently observed in the dLGN of control animals (Fig.
418 1D and 2B), suggesting that during normal development, activity-dependent caspase-3
419 activation is predominantly localized and generally does not lead to neuronal death.
420 Previous studies have proposed ubiquitin-dependent proteasomal degradation as a
421 mechanism that can restrain caspase-3 activity to local sites in dendrites (*24, 56, 57*).
422 Intriguingly, synaptic inactivation in our experiment was achieved through TeTxLC
423 expression in presynaptic RGCs, but caspase-3 activation was observed in postsynaptic
424 relay neurons. Conversely, while caspase-3 is activated in the postsynaptic compartment,
425 we were able to detect defects in synapse elimination using assays that measure
426 presynaptic inputs. These observations suggest that activity-dependent caspase-3
427 activation requires synaptic transmission, and that caspase-3 dependent synapse
428 elimination is not strictly axonal or dendritic but involves both pre- and post-synaptic
429 compartments. An important limitation of this study is that experiments in full-body *Casp3*$^{-}$
430 $^{/-}$ mice cannot query the roles of caspase-3 in presynaptic and postsynaptic compartments
431 separately. Future experiments that perturb caspase-3 activation and other signaling
432 events specifically in the pre- or post-synaptic compartments are needed to reveal more
433 detailed mechanisms of activity-dependent synapse elimination.

434 The observation that activity-dependent caspase-3 activation requires synaptic
435 competition resonates with previous research demonstrating that relative synaptic
436 efficacy biases the outcome of synapse elimination during development of neuromuscular
437 junctions and the callosal pathway (*15, 33, 58, 59*). However, the mechanisms linking
438 synaptic competition with caspase-3 activation remains elusive. During LTD, caspase-3
439 is activated through mitochondrial release of cytochrome-c (*18*). Whether synaptic
440 competition could induce caspase-3 activation via mechanisms such as calcium signaling,
441 which regulates both neurotransmission and cytochrome-c release (*60*), is an outstanding
442 question.
443
444 **Roles of microglia and astrocytes in synapse elimination**
445 The differential impact of caspase-3 deficiency on microglia- and astrocyte-
446 mediated synapses elimination in the visual pathway suggest that the two glial cell types
447 have nonidentical substrate specificities when engulfing synaptic material. Indeed,
448 considering that astrocytes are present at nearly ten-fold greater density than microglia
449 in the developing dLGN (Fig. 5A and S11A) and have comparable engulfing capacities
450 (Fig. 5D and S11D), contribution from microglia in synapse elimination would be negligible
451 if the two cell types target the same substrates, which contradicts previous findings (*7,*
452 *14*). A recent study discovered that during clearance of apoptotic neurons in adult brains,
453 microglia engulf the soma and proximal dendrites while astrocytes target distal dendrites,
454 and this difference in substrate preference is at least partially attributed to differential
455 kinetics in binding and engulfing substrates by the two cell types (*61*). Investigating

456 whether a similar division-of-labor exists during development could provide critical
457 insights into the mechanisms of activity-dependent, glia-mediated synapse elimination.
458 It is often assumed in the literature that microglia directly engulf intact synapses,
459 but existing data also support an alternative model where microglia indirectly contribute
460 to synapse elimination by engulfing synaptic debris that is shed through neuron-
461 autonomous mechanisms (*62*). The observation that synaptic activity instructs microglial
462 engulfment through caspase-3 activation raises the possibility that weakened synapses
463 partially disintegrate through apoptosis-like mechanisms prior to being engulfed by
464 microglia. Further studies are needed to elucidate the intermediate steps between
465 caspase-3 activation and microglial engulfment of synapses.
466
467 **Molecular link between caspase-3 activation and microglial engulfment**
468 How does caspase-3 activation at synapses recruit microglia for engulfment?
469 Caspase-3 activation is known to trigger the display of apoptosis markers that can be
470 recognized by phagocytes (*19*). One of the best understood markers is
471 phosphatidylserine (PtdSer), a phospholipid that translocates from the cytoplasmic leaflet
472 of the plasma membrane to the exoplasmic leaflet during apoptosis (*19*). Importantly,
473 caspase-3 directly regulates the enzymes that translocate PtdSer through enzymatic
474 cleavage (*63, 64*). Two recent studies demonstrated that PtdSer is displayed on
475 retinogeniculate synapses during postnatal development, and microglia use the exposed
476 PtdSer as a cue to target and engulf synapses (*8, 9*). Whether PtdSer exposure is
477 upregulated in response to synapse weakening and whether caspase-3 activity is
478 required for such exposure are important questions that require further investigation.

479 The complement protein C1q has been observed to bind to PtdSer on apoptotic
480 cells and facilitate phagocytic clearance (*19*). Additionally, a previous study found
481 caspase-3 activity in C1q-bound synaptosomes (*65*), suggesting that C1q may bridge
482 caspase-3 activation and synapse elimination. However, we investigated C1q expression
483 and localization in the dLGN of P5 TeTxLC-injected mice but did not observe upregulation
484 of C1q abundance or colocalization between C1q and caspase-3 activity (data not shown).
485

486 **Caspase-3 as a potential target for AD treatment**

487 Our findings suggest that caspase-3 deficiency confers protection against Aβ-
488 induced synapse loss in a mouse model of AD. Notably, the absence of caspase-3 does
489 not seem to affect Aβ deposition or microglia reactivity, indicating that caspase-3 depletion
490 may mitigate synapse loss by directly countering Aβ-induced synaptic toxicity. Given the
491 prominence of Aβ and inflammation as targets for AD drug development (*66*), inhibiting
492 caspase-3 activity offers a potential alternative therapeutic strategy that could
493 complement and enhance current treatment approaches. Therefore, it is important to test
494 whether pharmacological inhibition of caspase-3 can effectively slow synapse loss and
495 cognitive decline in both mouse models of AD and human patients.
496

497 **Acknowledgement:** We thank Crystall Lopez, Benjamin Gantz, and Brooke Groff for help
498 with animal husbandry and breeding. We thank Sarah Lindo, Colin Morrow, Claire Boyer,
499 and Rae Demars for help with surgery. We thank Monique Copeland, Amy Hu, Morgan
500 Clarke, and Benjamin Foster for help with histology. We are also grateful to Sarah
501 Kivimaki and the Viral Tools team of Janelia Core Services for help with AAV preparation.

502 We thank Dr. Cagla Eroglu, Dr. Richard Axel, and Dr. David Clapham for comments on
503 the manuscript. This work is supported by the Howard Hughes Medical Institute.

504

505 ## References:

506 1. M. Kano, K. Hashimoto, Synapse elimination in the central nervous system. *Curr Opin*
507 *Neurobiol* **19**, 154-161 (2009).
508 2. T. E. Faust, G. Gunner, D. P. Schafer, Mechanisms governing activity-dependent synaptic
509 pruning in the developing mammalian CNS. *Nat Rev Neurosci* **22**, 657-673 (2021).
510 3. M. M. Riccomagno, A. L. Kolodkin, Sculpting neural circuits by axon and dendrite pruning.
511 *Annu Rev Cell Dev Biol* **31**, 779-805 (2015).
512 4. L. C. Katz, C. J. Shatz, Synaptic activity and the construction of cortical circuits. *Science* **274**,
513 1133-1138 (1996).
514 5. J. Y. Hua, S. J. Smith, Neural activity and the dynamics of central nervous system
515 development. *Nat Neurosci* **7**, 327-332 (2004).
516 6. B. Stevens *et al.*, The classical complement cascade mediates CNS synapse elimination.
517 *Cell* **131**, 1164-1178 (2007).
518 7. D. P. Schafer *et al.*, Microglia sculpt postnatal neural circuits in an activity and
519 complement-dependent manner. *Neuron* **74**, 691-705 (2012).
520 8. T. Li *et al.*, A splicing isoform of GPR56 mediates microglial synaptic refinement via
521 phosphatidylserine binding. *Embo J* **39**, e104136 (2020).
522 9. N. Scott-Hewitt *et al.*, Local externalization of phosphatidylserine mediates developmental
523 synaptic pruning by microglia. *Embo J* **39**, e105380 (2020).
524 10. W. S. Chung *et al.*, Astrocytes mediate synapse elimination through MEGF10 and MERTK
525 pathways. *Nature* **504**, 394-400 (2013).
526 11. D. K. Wilton, L. Dissing-Olesen, B. Stevens, Neuron-Glia Signaling in Synapse Elimination.
527 *Annu Rev Neurosci* **42**, 107-127 (2019).
528 12. W. S. Chung, N. J. Allen, C. Eroglu, Astrocytes Control Synapse Formation, Function, and
529 Elimination. *Cold Spring Harb Perspect Biol* **7**, a020370 (2015).
530 13. Q. Li, B. A. Barres, Microglia and macrophages in brain homeostasis and disease. *Nat Rev*
531 *Immunol* **18**, 225-242 (2018).
532 14. R. C. Paolicelli *et al.*, Synaptic pruning by microglia is necessary for normal brain
533 development. *Science* **333**, 1456-1458 (2011).
534 15. M. Yasuda, S. Nagappan-Chettiar, E. M. Johnson-Venkatesh, H. Umemori, An activity-
535 dependent determinant of synapse elimination in the mammalian brain. *Neuron* **109**,
536 1333-1349 e1336 (2021).
537 16. R. L. Philips *et al.*, The JAK-STAT pathway at 30: Much learned, much more to do. *Cell* **185**,
538 3857-3876 (2022).
539 17. D. R. McIlwain, T. Berger, T. W. Mak, Caspase functions in cell death and disease. *Cold*
540 *Spring Harb Perspect Biol* **5**, a008656 (2013).

541 18. Z. Li *et al.*, Caspase-3 Activation via Mitochondria Is Required for Long-Term Depression
542 and AMPA Receptor Internalization. *Cell* **141**, 859-871 (2010).
543 19. S. Y. Park, I. S. Kim, Engulfment signals and the phagocytic machinery for apoptotic cell
544 clearance. *Exp Mol Med* **49**, (2017).
545 20. L. A. Trouw, A. M. Blom, P. Gasque, Role of complement and complement regulators in the
546 removal of apoptotic cells. *Mol Immunol* **45**, 1199-1207 (2008).
547 21. D. W. Williams, S. Kondo, A. Krzyzanowska, Y. Hiromi, J. W. Truman, Local caspase activity
548 directs engulfment of dendrites during pruning. *Nat Neurosci* **9**, 1234-1236 (2006).
549 22. C. T. Kuo, S. Zhu, S. Younger, L. Y. Jan, Y. N. Jan, Identification of E2/E3 ubiquitinating
550 enzymes and caspase activity regulating Drosophila sensory neuron dendrite pruning.
551 *Neuron* **51**, 283-290 (2006).
552 23. D. J. Simon *et al.*, A caspase cascade regulating developmental axon degeneration. *J*
553 *Neurosci* **32**, 17540-17553 (2012).
554 24. A. Erturk, Y. Wang, M. Sheng, Local pruning of dendrites and spines by caspase-3-
555 dependent and proteasome-limited mechanisms. *J Neurosci* **34**, 1672-1688 (2014).
556 25. L. Liang, C. Chen, Organization, Function, and Development of the Mouse
557 Retinogeniculate Synapse. *Annu Rev Vis Sci* **6**, 261-285 (2020).
558 26. A. A. Penn, P. A. Riquelme, M. B. Feller, C. J. Shatz, Competition in retinogeniculate
559 patterning driven by spontaneous activity. *Science* **279**, 2108-2112 (1998).
560 27. D. Stellwagen, C. J. Shatz, An instructive role for retinal waves in the development of
561 retinogeniculate connectivity. *Neuron* **33**, 357-367 (2002).
562 28. M. Yasuda, S. Nagappan-Chettiar, H. Umemori, In utero intraocular AAV injection for early
563 gene expression in the developing rodent retina. *STAR Protoc* **2**, 100742 (2021).
564 29. G. Schiavo *et al.*, Tetanus and botulinum-B neurotoxins block neurotransmitter release by
565 proteolytic cleavage of synaptobrevin. *Nature* **359**, 832-835 (1992).
566 30. T. E. Krahe, R. N. El-Danaf, E. K. Dilger, S. C. Henderson, W. Guido, Morphologically distinct
567 classes of relay cells exhibit regional preferences in the dorsal lateral geniculate nucleus
568 of the mouse. *J Neurosci* **31**, 17437-17448 (2011).
569 31. J. G. Parnavelas, E. J. Mounty, R. Bradford, A. R. Lieberman, The postnatal development of
570 neurons in the dorsal lateral geniculate nucleus of the rat: a Golgi study. *J Comp Neurol*
571 **171**, 481-499 (1977).
572 32. S. McComb *et al.*, Efficient apoptosis requires feedback amplification of upstream
573 apoptotic signals by effector caspase-3 or -7. *Sci Adv* **5**, eaau9433 (2019).
574 33. S. Nagappan-Chettiar, M. Yasuda, E. M. Johnson-Venkatesh, H. Umemori, The molecular
575 signals that regulate activity-dependent synapse refinement in the brain. *Curr Opin*
576 *Neurobiol* **79**, 102692 (2023).
577 34. F. M. Rossi *et al.*, Requirement of the nicotinic acetylcholine receptor beta 2 subunit for
578 the anatomical and functional development of the visual system. *Proc Natl Acad Sci U S A*
579 **98**, 6453-6458 (2001).
580 35. K. Kuida *et al.*, Decreased apoptosis in the brain and premature lethality in CPP32-
581 deficient mice. *Nature* **384**, 368-372 (1996).
582 36. C. Houde *et al.*, Caspase-7 expanded function and intrinsic expression level underlies
583 strain-specific brain phenotype of caspase-3-null mice. *J Neurosci* **24**, 9977-9984 (2004).

37. L. De Haan, T. R. Hirst, Cholera toxin: a paradigm for multi-functional engagement of cellular mechanisms (Review). *Mol Membr Biol* **21**, 77-92 (2004).
38. C. L. Torborg, M. B. Feller, Unbiased analysis of bulk axonal segregation patterns. *J Neurosci Meth* **135**, 17-26 (2004).
39. N. Otsu, A Threshold Selection Method from Gray-Level Histograms. *IEEE Transactions on Systems, Man, and Cybernetics* **9**, 62-66 (1979).
40. R. W. Young, Cell death during differentiation of the retina in the mouse. *J Comp Neurol* **229**, 362-373 (1984).
41. B. Dreher, R. A. Potts, M. R. Bennett, Evidence that the early postnatal reduction in the number of rat retinal ganglion cells is due to a wave of ganglion cell death. *Neurosci Lett* **36**, 255-260 (1983).
42. A. R. Rodriguez, L. P. de Sevilla Muller, N. C. Brecha, The RNA binding protein RBPMS is a selective marker of ganglion cells in the mammalian retina. *J Comp Neurol* **522**, 1411-1443 (2014).
43. C. Chen, W. G. Regehr, Developmental remodeling of the retinogeniculate synapse. *Neuron* **28**, 955-966 (2000).
44. B. M. Hooks, C. Chen, Distinct roles for spontaneous and visual activity in remodeling of the retinogeniculate synapse. *Neuron* **52**, 281-291 (2006).
45. W. G. Regehr, Short-term presynaptic plasticity. *Cold Spring Harb Perspect Biol* **4**, a005702 (2012).
46. S. Jung *et al.*, Analysis of fractalkine receptor CX(3)CR1 function by targeted deletion and green fluorescent protein reporter gene insertion. *Mol Cell Biol* **20**, 4106-4114 (2000).
47. T. Iram *et al.*, Megf10 Is a Receptor for C1Q That Mediates Clearance of Apoptotic Cells by Astrocytes. *J Neurosci* **36**, 5185-5192 (2016).
48. G. Lemke, Biology of the TAM receptors. *Cold Spring Harb Perspect Biol* **5**, a009076 (2013).
49. S. Gong *et al.*, A gene expression atlas of the central nervous system based on bacterial artificial chromosomes. *Nature* **425**, 917-925 (2003).
50. D. S. Knopman *et al.*, Alzheimer disease. *Nat Rev Dis Primers* **7**, 33 (2021).
51. S. Meftah, J. Gan, Alzheimer's disease as a synaptopathy: Evidence for dysfunction of synapses during disease progression. *Front Synaptic Neurosci* **15**, 1129036 (2023).
52. G. M. Shankar *et al.*, Amyloid-beta protein dimers isolated directly from Alzheimer's brains impair synaptic plasticity and memory. *Nat Med* **14**, 837-842 (2008).
53. J. Jo *et al.*, Abeta(1-42) inhibition of LTP is mediated by a signaling pathway involving caspase-3, Akt1 and GSK-3beta. *Nat Neurosci* **14**, 545-547 (2011).
54. M. D'Amelio *et al.*, Caspase-3 triggers early synaptic dysfunction in a mouse model of Alzheimer's disease. *Nat Neurosci* **14**, 69-76 (2011).
55. J. L. Jankowsky *et al.*, Mutant presenilins specifically elevate the levels of the 42 residue beta-amyloid peptide in vivo: evidence for augmentation of a 42-specific gamma secretase. *Hum Mol Genet* **13**, 159-170 (2004).
56. Y. Suzuki, Y. Nakabayashi, R. Takahashi, Ubiquitin-protein ligase activity of X-linked inhibitor of apoptosis protein promotes proteasomal degradation of caspase-3 and enhances its anti-apoptotic effect in Fas-induced cell death. *Proc Natl Acad Sci U S A* **98**, 8662-8667 (2001).

57. Y. E. Choi *et al.*, The E3 ubiquitin ligase cIAP1 binds and ubiquitinates caspase-3 and -7 via unique mechanisms at distinct steps in their processing. *J Biol Chem* **284**, 12772-12782 (2009).
58. M. Buffelli *et al.*, Genetic evidence that relative synaptic efficacy biases the outcome of synaptic competition. *Nature* **424**, 430-434 (2003).
59. Y. I. Lee, Developmental neuromuscular synapse elimination: Activity-dependence and potential downstream effector mechanisms. *Neurosci Lett* **718**, 134724 (2020).
60. C. Garrido *et al.*, Mechanisms of cytochrome c release from mitochondria. *Cell Death Differ* **13**, 1423-1433 (2006).
61. E. C. Damisah *et al.*, Astrocytes and microglia play orchestrated roles and respect phagocytic territories during neuronal corpse removal in vivo. *Sci Adv* **6**, eaba3239 (2020).
62. U. Eyo, A. V. Molofsky, Defining microglial-synapse interactions. *Science* **381**, 1155-1156 (2023).
63. J. Suzuki, D. P. Denning, E. Imanishi, H. R. Horvitz, S. Nagata, Xk-Related Protein 8 and CED-8 Promote Phosphatidylserine Exposure in Apoptotic Cells. *Science* **341**, 403-406 (2013).
64. K. Segawa *et al.*, Caspase-mediated cleavage of phospholipid flippase for apoptotic phosphatidylserine exposure. *Science* **344**, 1164-1168 (2014).
65. B. A. Gyorffy *et al.*, Local apoptotic-like mechanisms underlie complement-mediated synaptic pruning. *Proc Natl Acad Sci U S A* **115**, 6303-6308 (2018).
66. P. van Bokhoven *et al.*, The Alzheimer's disease drug development landscape. *Alzheimers Res Ther* **13**, 186 (2021).

Figures:

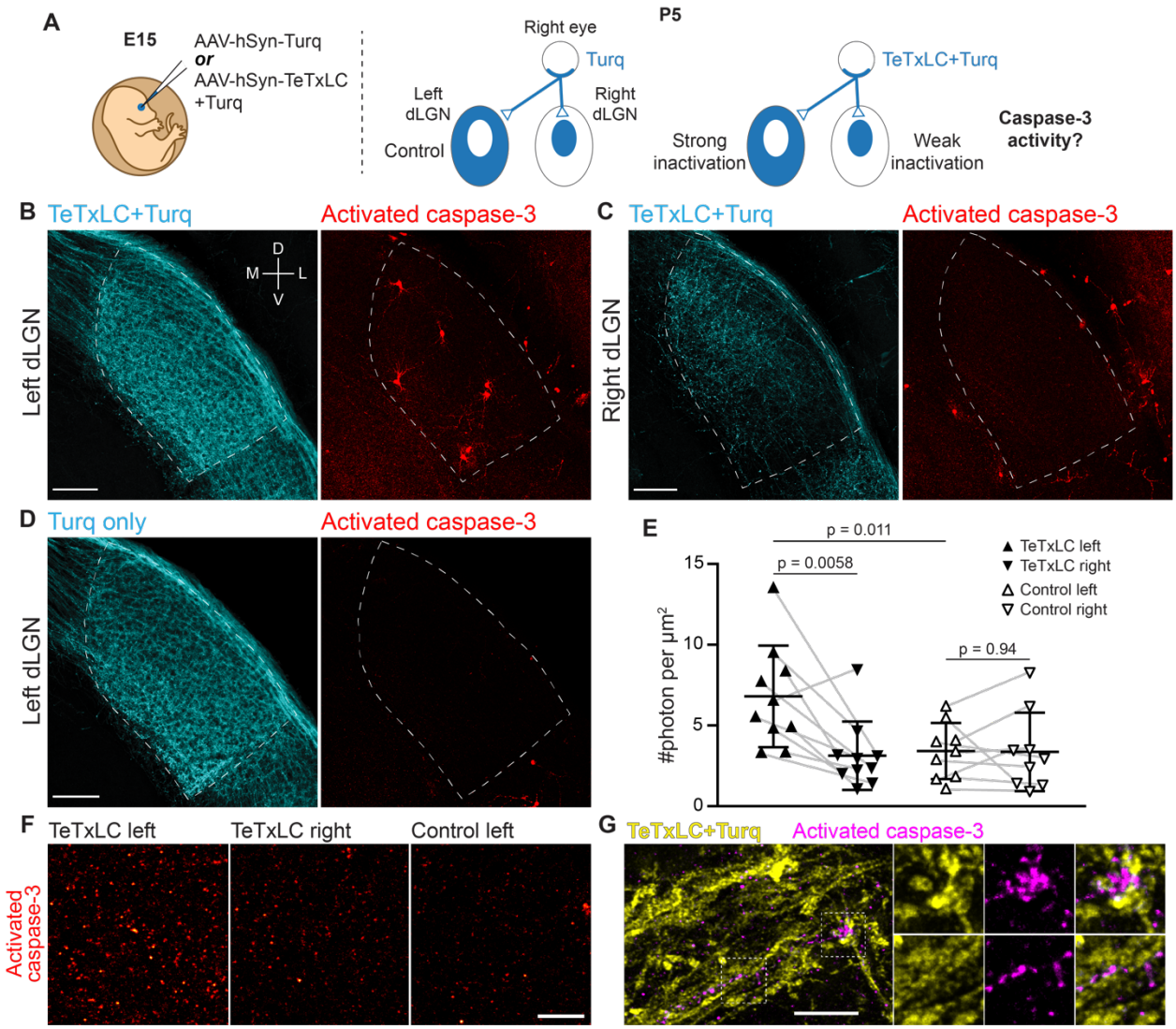

Figure 1. Inactivation of retinogeniculate synapses induces caspase-3 activity. (**A**) Schematics of experimental setup. AAVs expressing tetanus toxin light chain (TeTxLC) and/or mTurquiose2 (Turq) were injected into the right eye of E15 mice (left). By P5, retinogeniculate synapses in dLGN were inactivated to varying extents depending on injection and side (right). (**B**-**D**) Confocal images of Turq (left panels) and activated caspase-3 (right panels) in left dLGN (**B**) and right dLGN (**C**) of a TeTxLC-injected P5 animal and in left dLGN of a control P5 animal (**D**). Images from the same fluorescent channel were adjusted to the same contrast. Dotted lines delineate dLGN boundaries. The compass in **B** marks tissue orientation. Scale-bars: 100 µm. D, dorsal; V, ventral; M, medial; L, lateral. (**E**) Quantification of caspase-3 activity in indicated dLGNs. Activated caspase-3 signals in each dLGN (highlighted areas in **B**-**D**) were summed and normalized to dLGN area. Each point represents the result from one dLGN. Data from two dLGNs of the same animal were paired for analysis (grey lines). n=10 for TeTxLC-injected animals and n=9 for control animals. Mean and standard deviation (S.D.) are shown. P-values were calculated from two-tailed t-tests (paired when applicable). (**F**) Example images showing punctate caspase-3 activities in ventral-medial regions of indicated dLGNs. Images were adjusted to the same contrast. Scale-bar: 20 µm. (**G**) High-resolution images of dLGN showing TeTxLC-expressing RGC axons (yellow) and activated caspase-3 (magenta). Two regions of interest (dotted squares) are magnified to illustrate that caspase-3 activity was found juxtaposing TeTxLC-expressing axon terminals but not within them. Scale-bar: 5 µm.

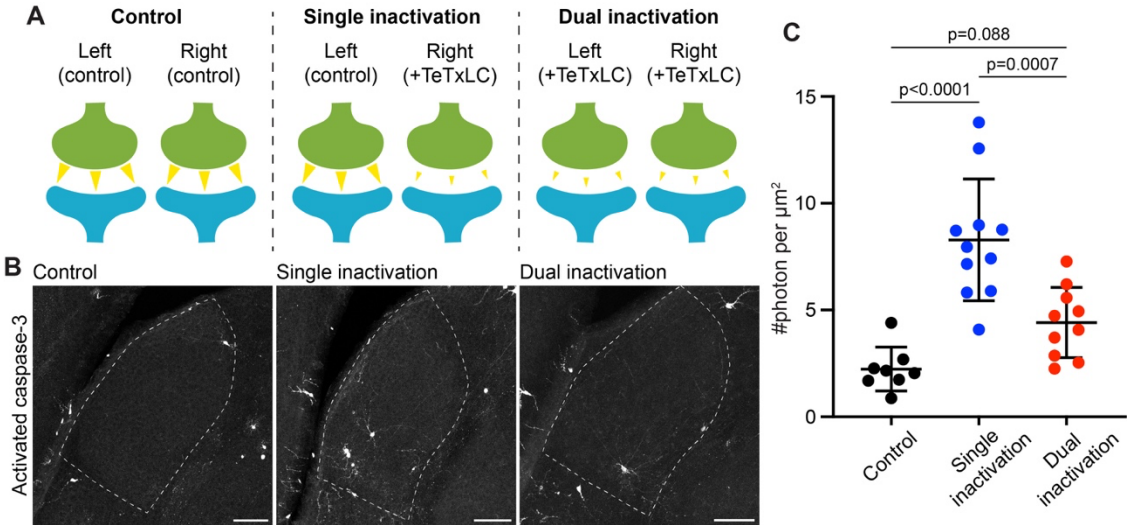

Figure 2. Synapse inactivation-induced caspase-3 activation requires synaptic competition. (**A**) Schematics illustrating different experimental conditions. Presynaptic (green) and postsynaptic (cyan) compartments and synaptic strength (yellow arrowheads) of retinogeniculate synapses are shown. No synapses are inactivated in the control (left); expressing TeTxLC only in right eye inputs results in synapse inactivation and competition (middle); expressing TeTxLC in both eyes results in synapse inactivation but no competition (right). (**B**) Confocal images of dLGNs in the three conditions showing activated caspase-3 signal. The dLGN shown for the single inactivation condition was from the left side. Dotted lines mark dLGN boundaries. Scale-bars: 100 µm. (**C**) Quantification of caspase-3 activity in the dLGN in the indicated conditions. Activated caspase-3 signal in each dLGN were summed and normalized to the dLGN area. For the single inactivation condition, values were from the left dLGN only. For the other two conditions, values from both dLGNs were averaged. n=8 animals for control, n=11 animals for single inactivation, and n=10 animals for dual inactivation. Mean and S.D. are shown. P-values were calculated from Tukey's multiple comparison tests.

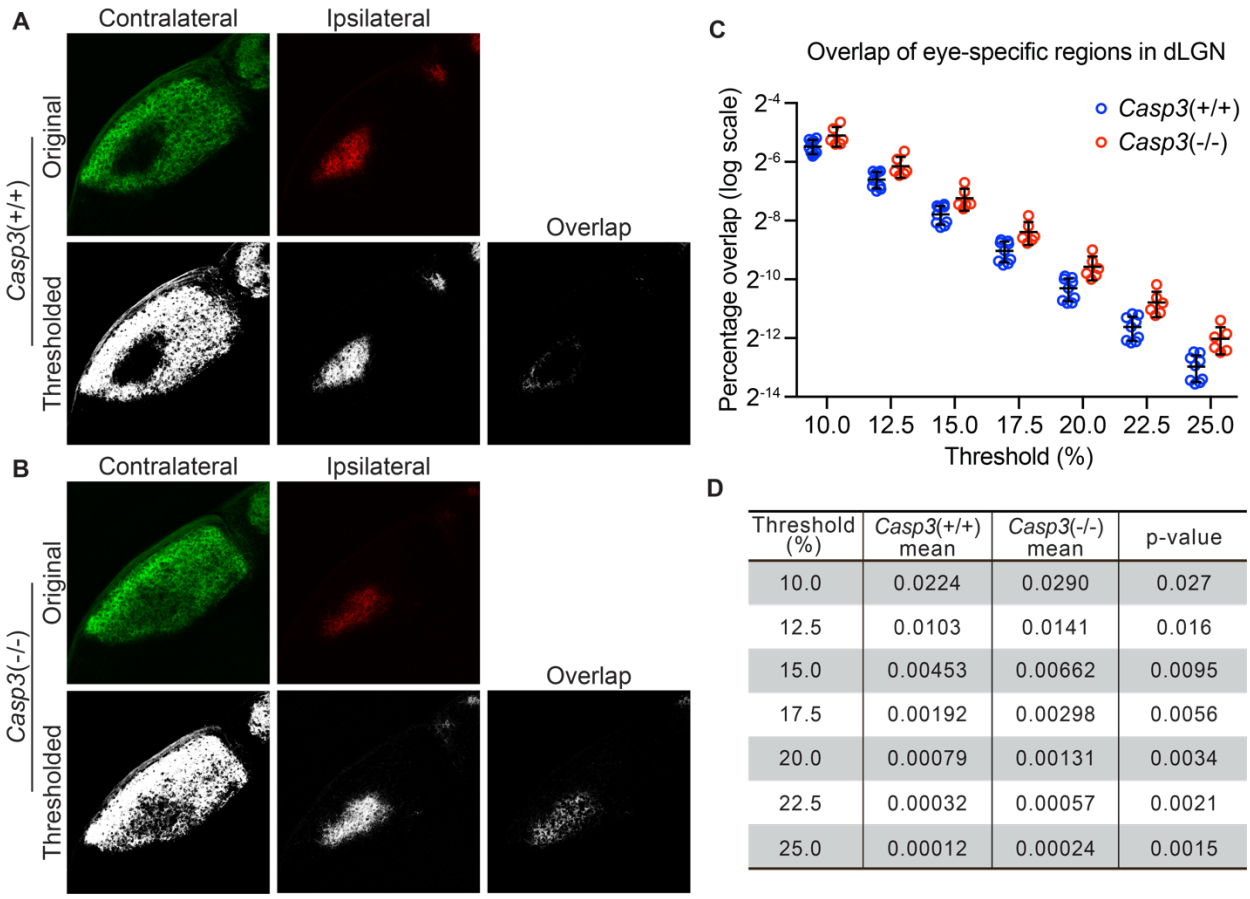

D

Threshold (%)	*Casp3*(+/+) mean	*Casp3*(-/-) mean	p-value
10.0	0.0224	0.0290	0.027
12.5	0.0103	0.0141	0.016
15.0	0.00453	0.00662	0.0095
17.5	0.00192	0.00298	0.0056
20.0	0.00079	0.00131	0.0034
22.5	0.00032	0.00057	0.0021
25.0	0.00012	0.00024	0.0015

Figure 3. Caspase-3 is required for segregation of eye-specific territories. (**A**-**B**) Representative confocal images of retinogeniculate inputs in the dLGN of P10 wild-type (**A**) and *Casp3*$^{-/-}$ (**B**) mice. Contralateral inputs are labeled with AlexaFlour488 (AF488) conjugated cholera toxin subunit B (CTB) and ipsilateral inputs with AF594-CTB. Original images were thresholded into 0-or-1 images using the Otsu method (*34*), and the overlap between thresholded contralateral and ipsilateral inputs is shown. (**C**) Percentage overlap between eye-specific territories in wildtype and *Casp3*$^{-/-}$ mice under a series of increasing signal cutoff thresholds. Note that the percentage overlap is plotted on a log scale. Each circle represents one animal. Mean and S.D. are shown. n=9 for wildtype mice and n=6 for *Casp3*$^{-/-}$ mice. (**D**) Mean percentage overlap values in wildtype and *Casp3*$^{-/-}$ mice and p-values of two-tailed t-tests between the two genotypes are listed for each cutoff threshold.

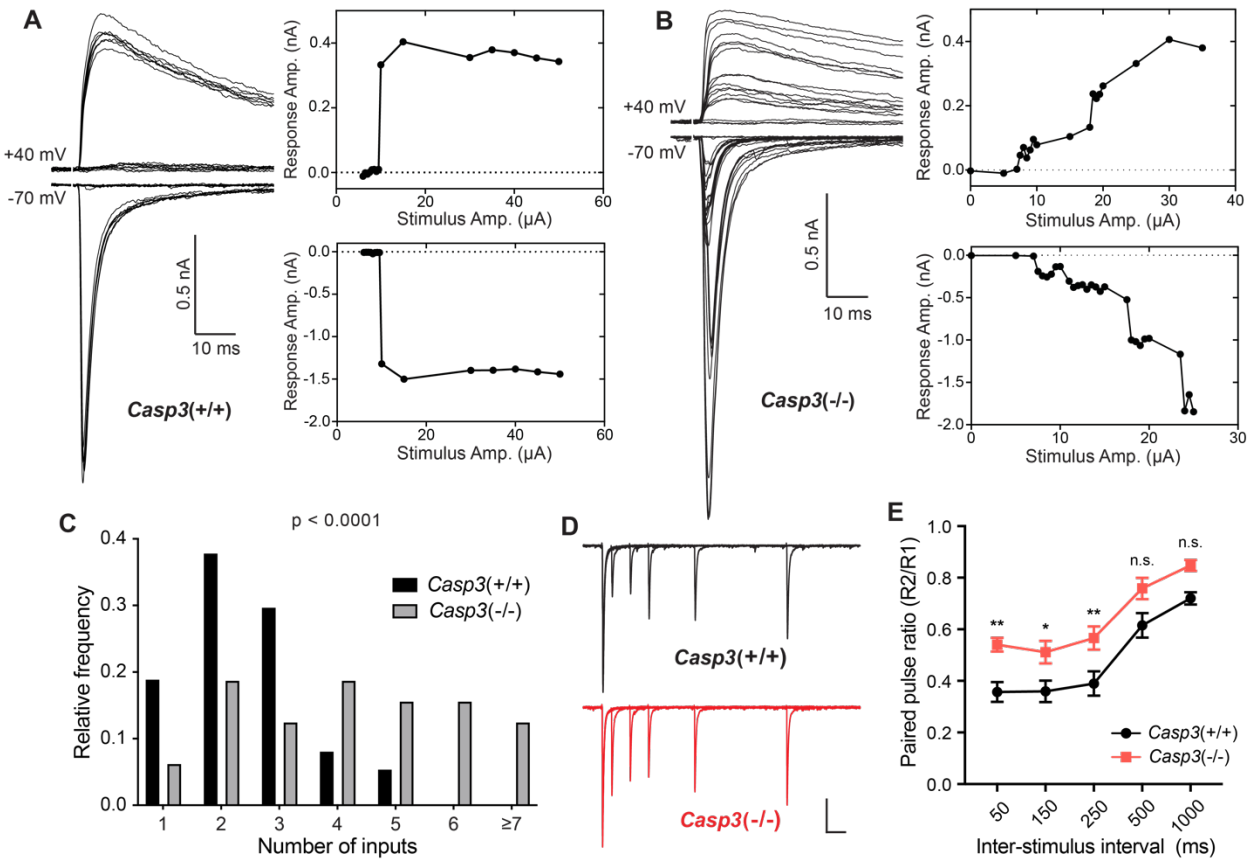

Figure 4. Caspase 3 is required for retinogeniculate circuit refinement. (**A**-**B**) Example recordings of dLGN relay neuron responses in P30 wildtype (**A**) and *Casp3*$^{-/-}$ (**B**) mice. Excitatory postsynaptic currents (EPSCs) were evoked by increasing stimulation currents in the optic tract. Both AMPAR-mediated inward current at -70 mV membrane potential and AMPAR and NMDAR-mediated outward current at +40 mV membrane potential are shown. Peak response amplitudes at each stimulation intensity are plotted to the right of recording traces. Scale bars represent 0.5 nA and 10 ms. (**C**) Distribution of RGC input numbers on individual dLGN relay neurons in wildtype and *Casp3*$^{-/-}$ mice. The number of RGC inputs was inferred by manually counting the number of steps in AMPAR-mediated EPSC response curves (lower right in **A** and **B**) while blind to the genotypes. P-value was calculated from two-tailed t-test. n=37 cells for wildtype mice and n=32 cells for *Casp3*$^{-/-}$ mice. (**D**) Example recordings from paired pulse measurements at -70 mV membrane potential in wildtype and *Casp3*$^{-/-}$ mice. Traces from experiments with 50, 150, 250, 500, and 1000 ms inter-stimulus intervals are overlayed. Stimulus artifacts were removed from the traces for clarity. Scale-bars represent 100 ms (horizontal) and 0.3 nA (vertical). (**E**) Paired-pulse ratio (calculated as peak amplitude of the second response over that of the first response) in wildtype and *Casp3*$^{-/-}$ mice at various inter-stimulus intervals. Mean and standard error of the mean (SEM) are shown. P-values were calculated from Bonferroni's multiple comparison test. p=0.0067 for 50 ms interval, p=0.0369 for 150 ms interval, and p=0.0097 for 250 ms interval. n=16 cells for wildtype mice and n=13 for *Casp3*$^{-/-}$ mice.

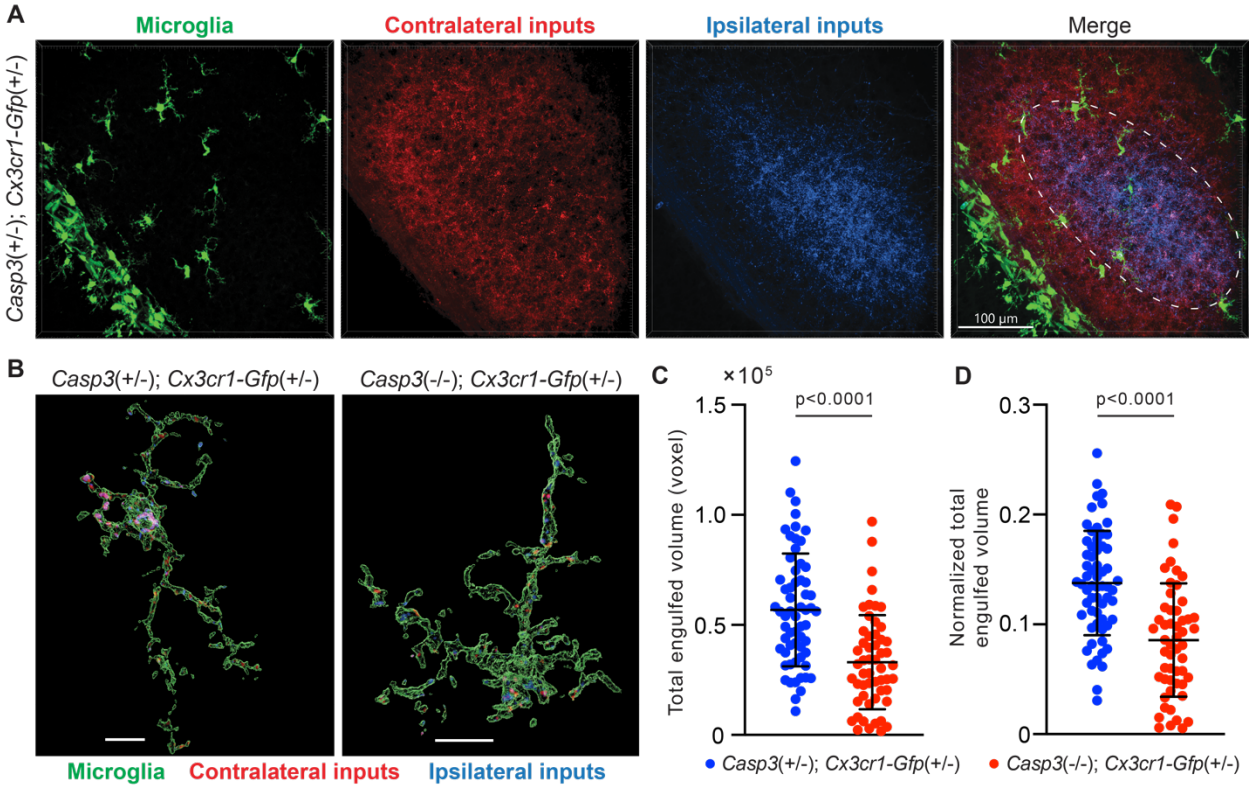

Figure 5. Microglia-mediated synapse elimination depends on caspase-3. (**A**) Representative 3D-reconstructed images of a P5 *Casp3*$^{+/-}$; *Cx3cr1-Gfp*$^{+/-}$ mouse dLGN with microglia displayed in green, contralateral RGC axon terminals in red, and ipsilateral RGC terminals in blue. In the merged image, the region from which microglia are selected for analysis is indicated with the dashed line. The scale-bar represents 100 µm. (**B**) Representative surface rendering of microglia (green) from P5 dLGNs of *Casp3*$^{+/-}$; *Cx3cr1-Gfp*$^{+/-}$ and *Casp3*$^{-/-}$; *Cx3cr1-Gfp*$^{+/-}$ mice. Intracellular contralateral (red) and ipsilateral (blue) RGC axon terminals are shown. Microglia from caspase-3 deficient mice engulf visibly less synaptic material. Scale-bars represent 10 µm. (**C**) Total volume of engulfed synaptic material in individual microglia from *Casp3*$^{+/-}$; *Cx3cr1-Gfp*$^{+/-}$ and *Casp3*$^{-/-}$; *Cx3cr1-Gfp*$^{+/-}$ mice. (**D**) Total volume of engulfed synaptic material in each microglia (from **C**) is normalized to the volume of that microglia. In **C**-**D**, each point represents one microglia. Mean and S.D. are shown. p-values were calculated from unpaired two-tailed t-tests. n=61 microglia from 8 *Casp3*$^{+/-}$; *Cx3cr1-Gfp*$^{+/-}$ mice and n=54 microglia from 5 *Casp3*$^{-/-}$; *Cx3cr1-Gfp*$^{+/-}$ mice.

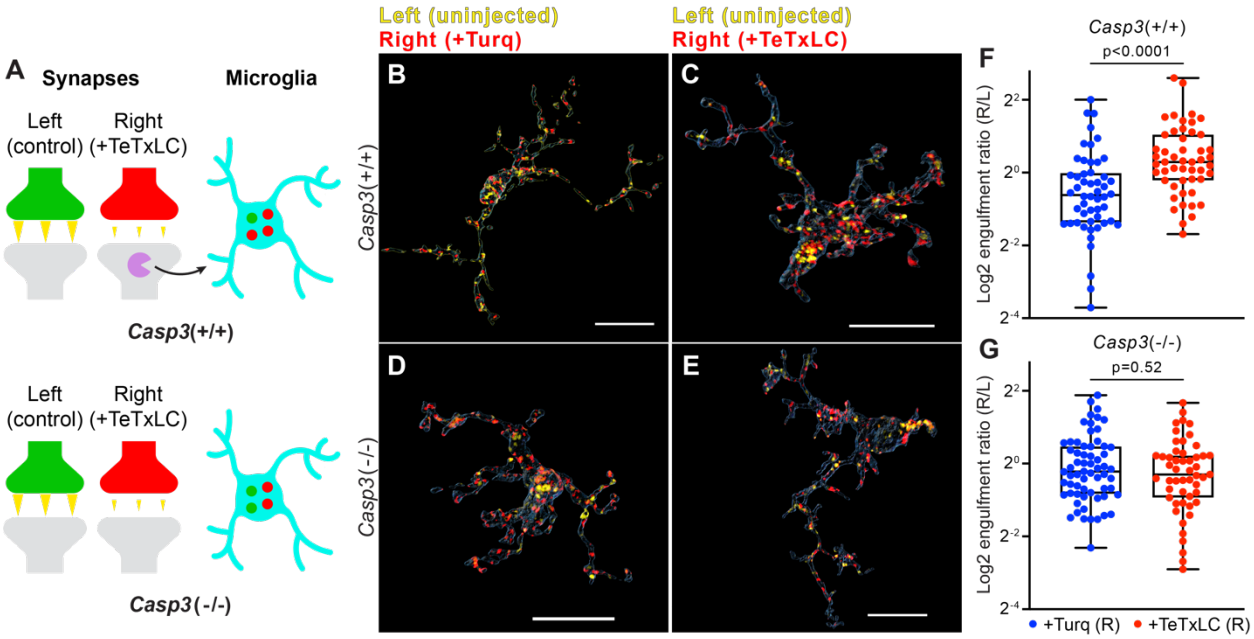

Figure 6. Caspase-3 activation determines specificity of microglia-mediated synapse elimination. (**A**) Schematics illustrating the experimental rationale. In wildtype mice (upper panel), inactivating retinogeniculate synapses from the right eye activates caspase-3 (magenta pie) and recruits microglia to engulf more right eye-originated synapses (red dots) than left eye-originated synapses (green dots). If caspase-3 activation is blocked (lower panel), we expect preferential engulfment of inactive synapses to be attenuated. (**B**-**E**) Surface rendering of representative microglia from P5 left dLGN of *Casp3*$^{+/+}$ (**B**-**C**) or *Casp3*$^{-/-}$ (**D**-**E**) mice injected with AAV expressing mTurquoise2 (**B** and **D**) or TeTxLC (**C** and **E**) in the right eye at E15. RGC axon terminals from the left eye are shown in yellow and terminals from the right eye in red. Scale bars represent 15 μm. (**F**-**G**) Ratio between volumes of right-eye and left-eye-originated synaptic material engulfed by microglia from *Casp3*$^{+/+}$ (**F**) or *Casp3*$^{-/-}$ (**G**) mice injected with AAV expressing mTurquoise2 (blue) or TeTxLC (red). Each dot represents one microglia. Engulfment ratios are displayed on a log scale. 0, 25, 50, 75, and 100 percentiles are shown. p-values were calculated from unpaired two-tailed Mann-Whitney tests. n=52 microglia from 7 Turq-injected *Casp3*$^{+/+}$ mice, n=50 microglia from 8 TeTxLC-injected *Casp3*$^{+/+}$ mice, n=64 microglia from 5 Turq-injected *Casp3*$^{-/-}$ mice, and n=51 microglia from 6 TeTxLC-injected *Casp3*$^{-/-}$ mice.

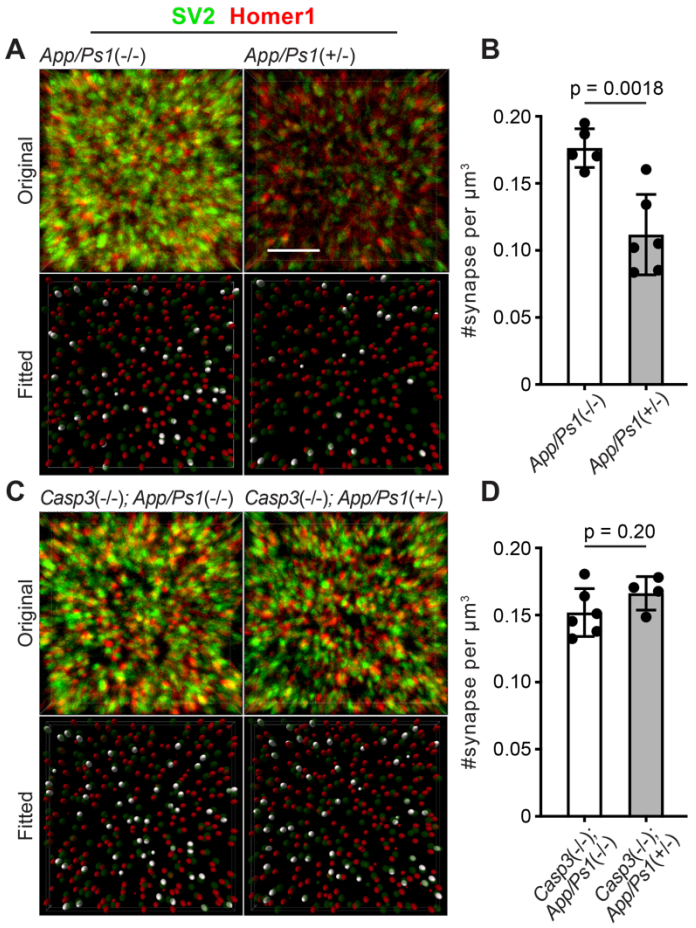

Figure 7. Caspase-3 deficiency protects against Aβ induced synapse loss. (**A** and **C**) Representative 3D-reconstructed images (3 μm in z) showing presynaptic (SV2, in green) and postsynaptic (Homer1, in red) signals in dentate gyrus of female 6 month-old APP/PS1 mice on caspase-3 wildtype (**A**) and deficient (**C**) backgrounds. Ellipsoids were fitted to the original images (upper panels) to isolate pre- (green) and post-synaptic (red) puncta (lower panels). Homer1 ellipsoids found with 300 nm of a SV2 ellipsoid are highlighted in white in the fitted images. Original images are adjusted to the same contrast. For the fitted images, only ellipsoids from the upper half of the z-stack are shown. Scale-bar represents 4 μm. (**B** and **D**) Quantification of synapse density in APP/PS1 mice on caspase-3 wildtype (**B**) and deficient (**D**) backgrounds. Mean and S.D. are shown. p-values were calculated from unpaired two-tailed t-tests. n=5 for *App/Ps1*$^{-/-}$ mice, n=6 for *App/Ps1*$^{+/-}$ mice, n=6 for *Casp3*$^{-/-}$; *App/Ps1*$^{-/-}$ mice, and n=4 for *Casp3*$^{-/-}$; *App/Ps1*$^{+/-}$ mice.

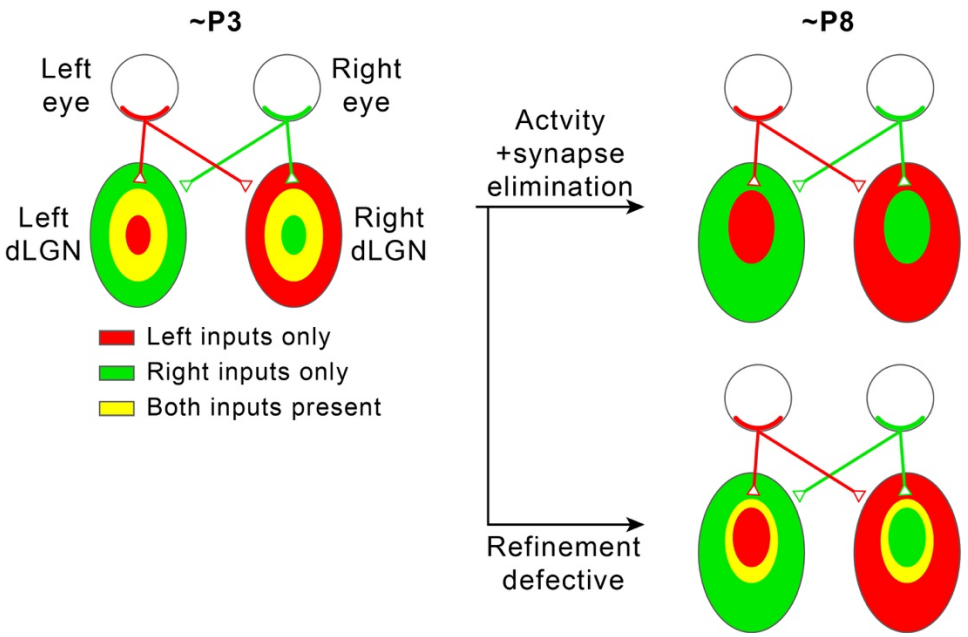

Figure S1. Segregation of eye-specific territories in the mouse retinogeniculate pathway. In the mouse retinogeniculate pathway, retinal ganglion cells (RGCs) in the retina of each eye innervate relay neurons in both the contralateral (opposite side as the originating RGC) dorsal lateral geniculate nucleus (dLGN) and the ipsilateral (same side from the originating RGC) dLGN to form retinogeniculate synapses (upper right). Within each dLGN, the majority of retinogeniculate synapses receive inputs from the contralateral eye, while the minority receive inputs from the ipsilateral eye (upper right). At the age of P3, regions in each dLGN receiving inputs from each of the two eyes overlap significantly (left). Through a process that requires synapse elimination and spontaneous RGC activity, these regions are refined into non-overlapping eye-specific territories by the age of P8 (upper right). If the refinement process is defective because neural activity or synapse elimination is disrupted, eye-specific territories fail to completely segregate, and regions innervated by the two eyes remain overlapping (lower right).

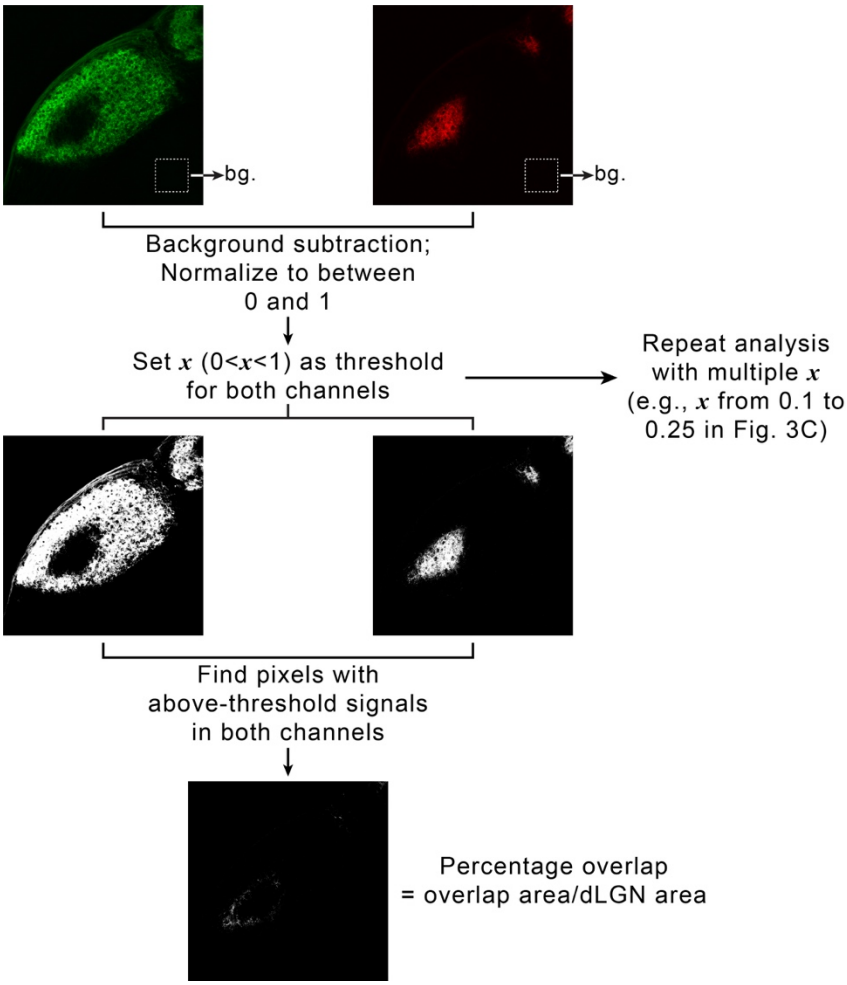

Figure S2. Quantifying eye-specific segregation with multi-threshold overlap analysis. For each dLGN, RGC inputs from the two eyes were imaged using separate fluorescence channels. A small area in the thalamus outside of each dLGN was chosen, and average signal intensity in each channel within that area was calculated and used as background (upper panel). For each channel, background was subtracted, and signals were normalized to between 0 and 1. To calculate overlap between eye-specific territories, a threshold, x, was chosen between 0 and 1 and applied to both channels (middle panel). The overlap between eye-specific territories were defined as the set of pixels with above-threshold signals in both channels. Percentage overlap was then calculated as the ratio between the area of the dLGN where eye-specific territories overlapped and the total area of the dLGN (lower panel). To avoid introducing biases by artificially selecting one threshold, we repeated the analysis with a set of increasingly stringent thresholds (e.g., from 0.1 to 0.25 in Fig. 3C and 3D).

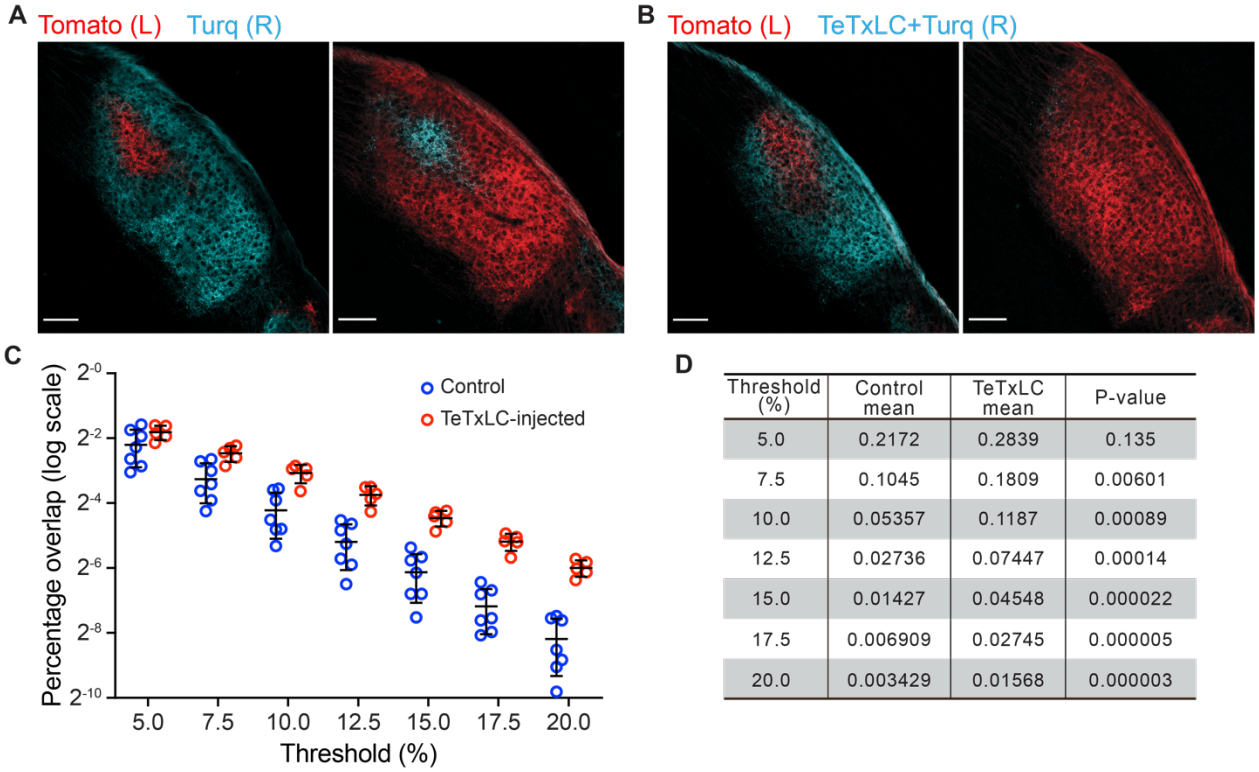

D

Threshold (%)	Control mean	TeTxLC mean	P-value
5.0	0.2172	0.2839	0.135
7.5	0.1045	0.1809	0.00601
10.0	0.05357	0.1187	0.00089
12.5	0.02736	0.07447	0.00014
15.0	0.01427	0.04548	0.000022
17.5	0.006909	0.02745	0.000005
20.0	0.003429	0.01568	0.000003

Figure S3. Blocking spontaneous RGC activity in one eye with TeTxLC disrupts eye-specific segregation in the retinogeniculate pathway. (**A** and **B**) Confocal images of P8 left dLGN (left panels) and right dLGN (right panels) of an animal receiving control injections (**A**) and an animal receiving TeTxLC injection in the right eye (**B**). Eye-specific regions were labeled with tdTomato (red, left eye input) and mTurquiose2 (cyan, right eye input). Right eye territory (cyan) contracted and left eye territory (red) expanded in TeTxLC-injected animals (**B**) compared to controls (**A**). Scale-bars: 100 μm. (**C**) Quantification of overlap between eye-specific territories in dLGN of P8 control and TeTxLC-injected animals. Analysis was done at multiple thresholds to avoid biases introduced with threshold selection. Note that percentage overlap is displayed on a log scale. For details on the analysis, see Fig. S2 and text associated with Fig. 3. n=7 for control animals and 5 for TeTxLC-injected animals. Mean and S.D. are shown. (**D**) Statistics of the overlap analysis at multiple thresholds. Fold difference and the statistical significance of the difference in percentage overlap between the two groups of animals increased as threshold increased. P-values were calculated from two-tailed t-tests. We did not implement multiple comparison corrections as values at different thresholds are derived from the same dataset and are not independent.

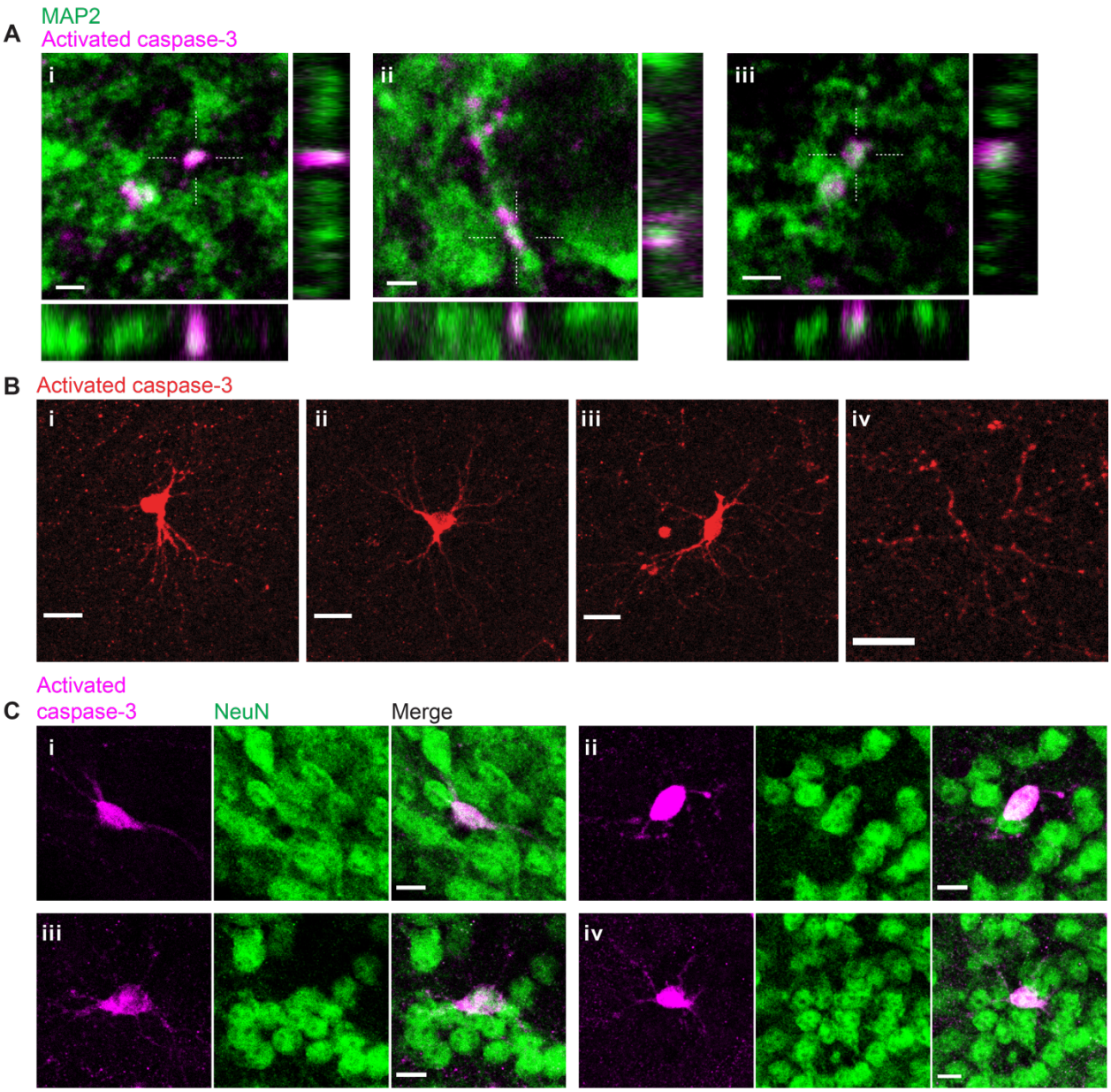

Figure S4. Inactivation of retinogeniculate synapses induces postsynaptic caspase-3 activity in dendritic compartments of dLGN relay neurons. (**A**) High-resolution images of three representative field-of-views (**i-iii**) in P5 TeTxLC-expressing dLGNs showing co-localization of punctate caspase-3 activity (magenta) and a dendritic marker, MAP2 (green). Dotted crosses mark x and y positions where the x-z and y-z cross-sections were generated. Scale-bars: 2 μm. (**B**) Example images showing caspase-3 activity in entire neurons (**i-iii**) or in multiple dendritic branches (but not the soma) of a neuron (**iv**) in P5 TeTxLC-expressing dLGNs. The neurons positive for active caspase-3 (**i-iii**) have relatively large and round somas and multipolar dendritic arbors that are characteristic of dLGN relay neurons. Scale-bars: 20 μm. (**C**) Example images of four representative neurons (**i-iv**) in P5 TeTxLC-expressing dLGNs that are positive for active caspase-3 (magenta) and a neuronal nuclear marker, NeuN (green). Scale-bars: 10 μm.

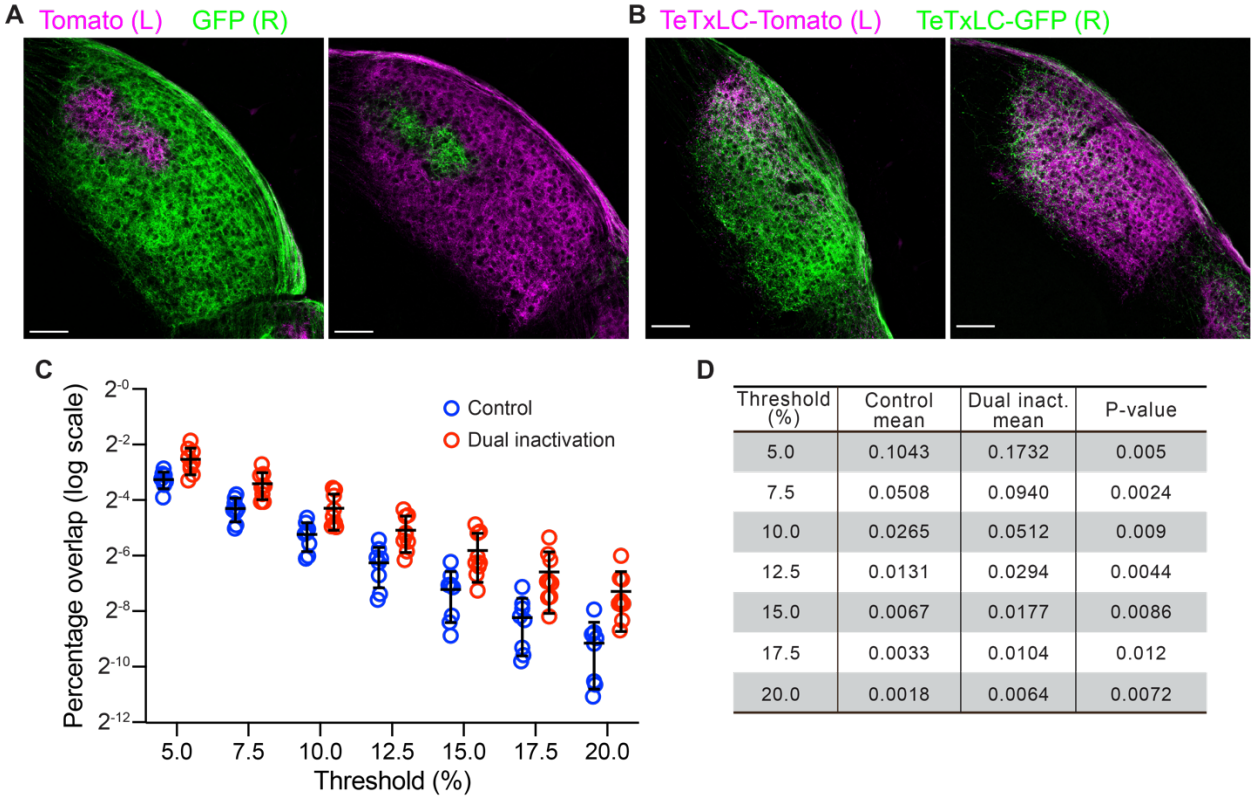

D

Threshold (%)	Control mean	Dual inact. mean	P-value
5.0	0.1043	0.1732	0.005
7.5	0.0508	0.0940	0.0024
10.0	0.0265	0.0512	0.009
12.5	0.0131	0.0294	0.0044
15.0	0.0067	0.0177	0.0086
17.5	0.0033	0.0104	0.012
20.0	0.0018	0.0064	0.0072

Figure S5. Blocking spontaneous RGC activity in both eyes with TeTxLC disrupts eye-specific segregation in the retinogeniculate pathway. (**A** and **B**) Confocal images of the left dLGN (left panels) and right dLGN (right panels) of an animal receiving control injections in both eyes (**A**) and an animal receiving TeTxLC injection in both eyes (**B**). Eye-specific territories were labeled with tdTomato (magenta, left eye input) and eGFP (green, right eye input). In animals injected with TeTxLC in both eyes, territories of the two eyes are similar in size and are more dispersive compared to those in controls, leading to substantial overlap between eye-specific territories. Scale-bars: 100 μm. (**C**) Quantification of overlap between eye-specific territories in the dLGN of control and dual TeTxLC-injected animals. Analysis was done at multiple thresholds to avoid biases introduced with threshold selection. Note that percentage overlap is displayed on a log scale. For details on the analysis, see Fig. S2 and text associated with Fig. 3. n=8 for control animals and n=9 for dually TeTxLC-injected animals. Mean and S.D. are shown. (**D**) Statistics of the overlap analysis at multiple thresholds. Fold difference between the two groups of animals increases as the threshold increases. Statistical significance does not show clear increase with threshold as percentage overlap values are more variable at higher thresholds. P-values were calculated from two-tailed t-tests. We did not implement multiple comparison corrections as values at different thresholds are derived from the same dataset and are not independent.

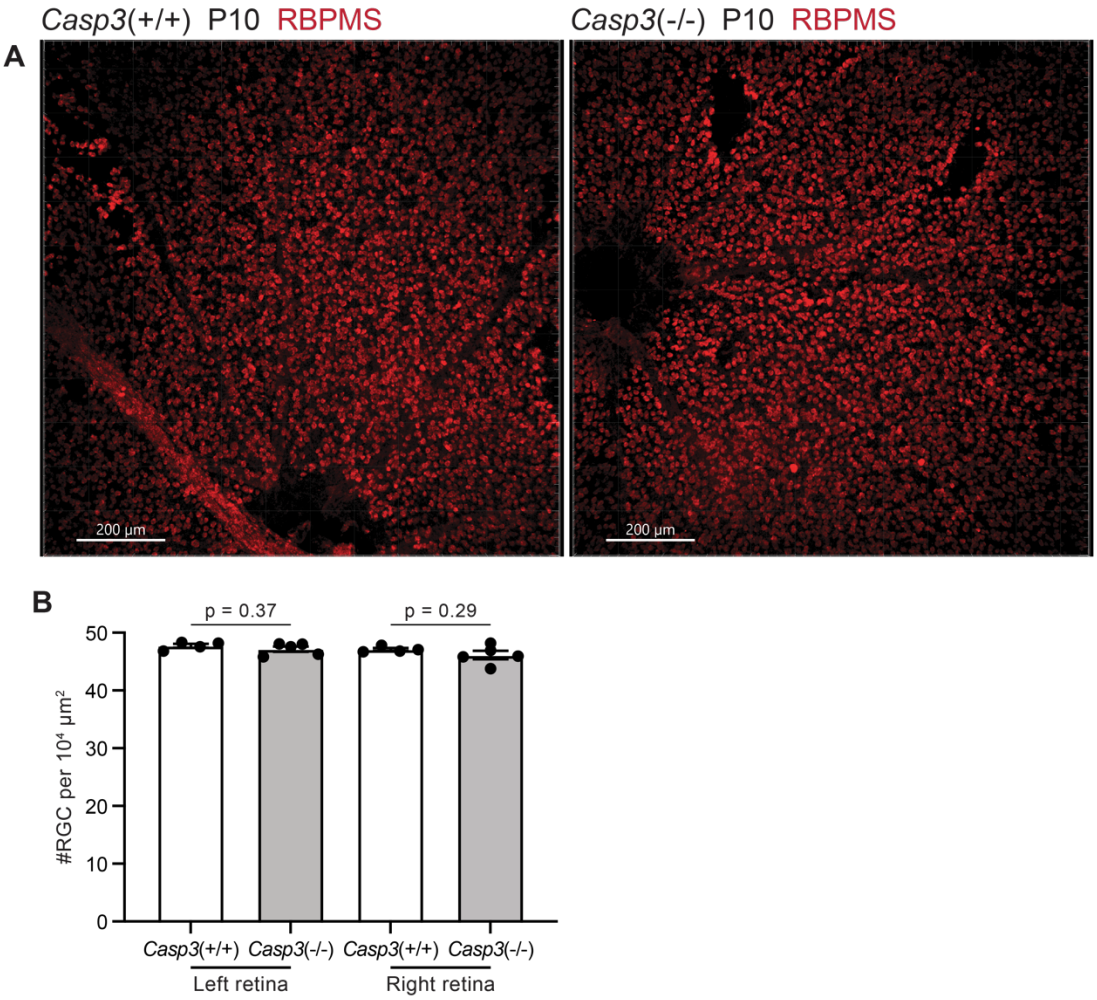

Figure S6. Caspase-3 deficiency does not alter RGC density in the retina. (**A**) Images of whole-mount retinae from P10 *Casp3*$^{+/+}$ (left) and *Casp3*$^{-/-}$ (right) animals. RGCs were labeled in red by immunostaining against an RGC-specific marker, RBPMS (RNA-binding protein with multiple splicing) (*37*). The dark regions on the bottom of the left panel and on the left of the right panel are optic discs. Scale-bars: 200 µm. (**B**) Quantification of RGC densities in retinae of P10 *Casp3*$^{+/+}$ and *Casp3*$^{-/-}$ animals. Each point represents one retina. Left and right retinae were analyzed separately. n=4 animals for *Casp3*$^{+/+}$ mice and n=5 animals for *Casp3*$^{-/-}$ mice. Mean and S.D. are shown. P-values were calculated from unpaired two-tailed t-tests.

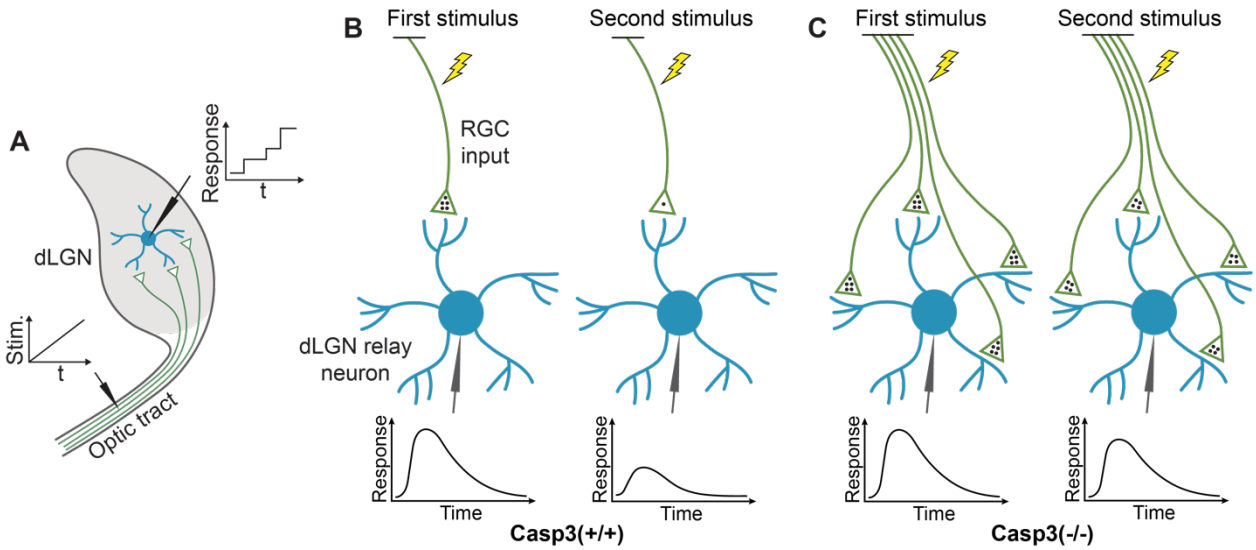

Figure S7. Measuring electrophysiological properties of retinogeniculate synapses. (**A**) Inferring the number of RGC inputs of dLGN relay neurons by measuring stimulation-response curves. To measure relay neuron responses, we prepared acute brain slices from a tilted parasagittal plane in P30 mice (*38*). These slice preparations preserved a long segment of the optic tract and a high level of connectivity between RGC axons and dLGN relay neurons (*38*). We placed a stimulating electrode on the optic tract and patch-clamped individual dLGN relay neurons with a recording electrode. We stimulated the optic tract with a series of gradually increasing currents and recorded excitatory postsynaptic currents (EPSCs) in relay neurons. At low stimulation intensity, no RGC axons were activated. As the stimulus increased, more and more RGC axons were recruited. As different RGC axons have different excitation thresholds, RGC axons were excited one at a time. Whenever a stimulus activated an RGC axon that did not respond to lower stimuli, a step increase in the relay neuron response was detected, and the increment corresponded to the EPSC evoked by the newly recruited RGC axon. We can therefore infer the number of RGC inputs innervating the relay neuron being recorded by counting the number of steps in the response curve of that relay neuron. t: time. Stim.: stimulation intensity. (**B**-**C**) Inferring the number of release sites from RGC inputs by measuring paired-pulse response ratio (PPR). We stimulated the optic tract with two stimuli separated by a short interval and recorded EPSCs in dLGN relay neurons. The stimulus intensity was chosen to evoke maximum response in the relay neuron. In wildtype mice (**B**), the first stimulus triggers the release of a significant fraction of the readily releasable pool (RRP) of neurotransmitters (black dots), evoking a strong response (left). At the time of the second stimulus, the RRP does not have sufficient time to recover and remains depleted, resulting in a weaker second response (right). PPR can be calculated from this experiment by dividing the peak amplitude of the second response with that of the first. PPR is small in wildtype animals. In caspase-3 deficient mice (**C**), if the number of release sites is increased compared to wildtype animals, the RRP should be larger (left), and a smaller fraction of the RRP is released during the first stimulus, leaving more neurotransmitters available for the second stimulus (right), thereby enhancing the second response and PPR. Note that in this model, we made two assumptions. The first assumption is that the average size of the RRP in one release site is similar in *Casp3*$^{+/+}$ and *Casp3*$^{-/-}$ mice, which is supported by the comparable fiber fractions (FFs) in the two groups of animals (see Fig. S8E). The second assumption is that the number of neurotransmitters released during the first stimulus is similar in *Casp3*$^{+/+}$ and *Casp3*$^{-/-}$ mice (4 dots in the illustration), which is supported by the comparable maximum EPSCs in the two groups of animals (see Fig. S8B-C).

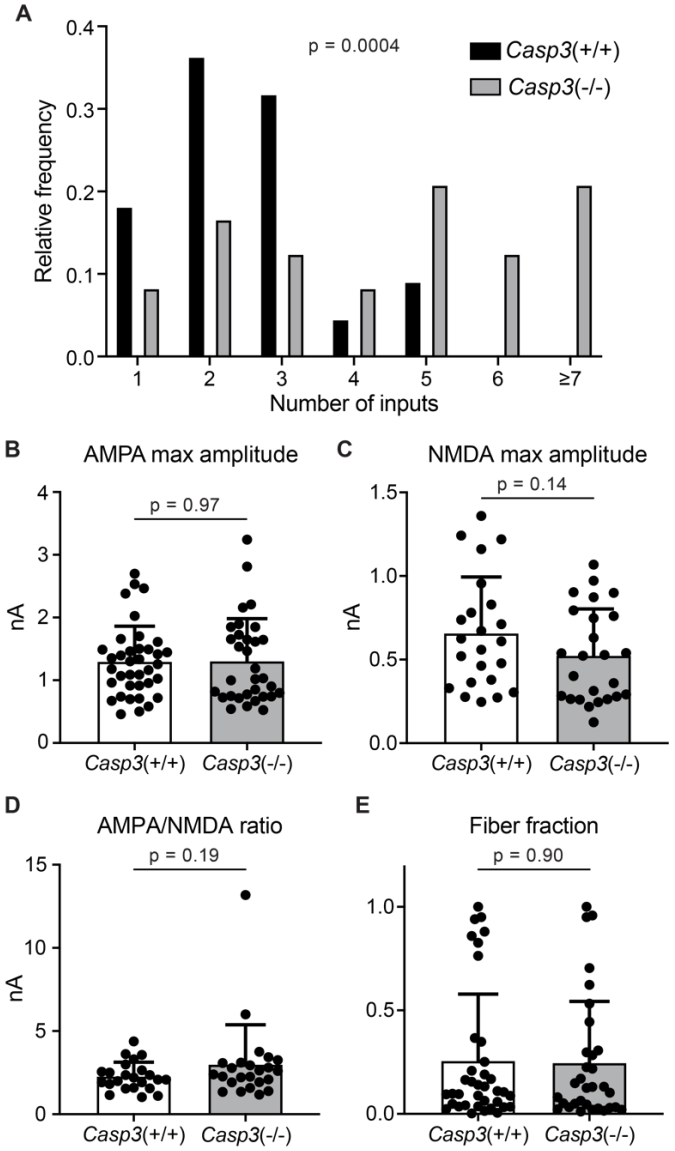

Figure S8. Additional analyses of electrophysiological properties of retinogeniculate synapses in *Casp3*$^{+/+}$ and *Casp3*$^{-/-}$ mice. (**A**) Distribution of RGC input numbers of individual dLGN relay neurons in wildtype and *Casp3*$^{-/-}$ mice measured by counting the number of steps in NMDAR-mediated EPSC response curves (upper right in Fig. 4A and 4B) while blind to genotypes. P-value was calculated from two-tailed t-test. n=22 cells for wildtype mice and n=24 cells for *Casp3*$^{-/-}$ mice. (**B**-**C**) Quantification of maximum amplitudes of AMPAR- (**B**) and NMDAR-mediated (**C**) EPSCs in wildtype and *Casp3*$^{-/-}$ dLGN relay neurons. (**D**) Quantification of the ratio between maximum amplitudes of AMPAR- and NDMAR-mediated EPSCs in wildtype and *Casp3*$^{-/-}$ dLGN relay neurons. (**E**) Quantification of fiber fractions in wildtype and *Casp3*$^{-/-}$ dLGN relay neurons. When stimulation on the optic tract is gradually increased, there will be a lowest stimulation intensity at which a non-zero response is first recorded in the relay neuron (see Fig. S8 for illustration and Fig. 4 for example data). This first response is presumed to be evoked by the activation of a single RGC axon fiber. Fiber fraction is defined as the ratio between this single-fiber response and the maximum response and ranges from 0 to 1. Only the AMPAR-mediated response is used to calculate fiber fractions. In **B**-**E**, mean and S.D. are shown. In **A**-**E**, p-values were calculated from two-tailed t-tests. In **A**, **C**, and **D**, n = 22 cells for wildtype mice and n=24 cells for *Casp3*$^{-/-}$ mice. In **B** and **E**, n=37 cells for wildtype mice and n=32 cells for *Casp3*$^{-/-}$ mice.

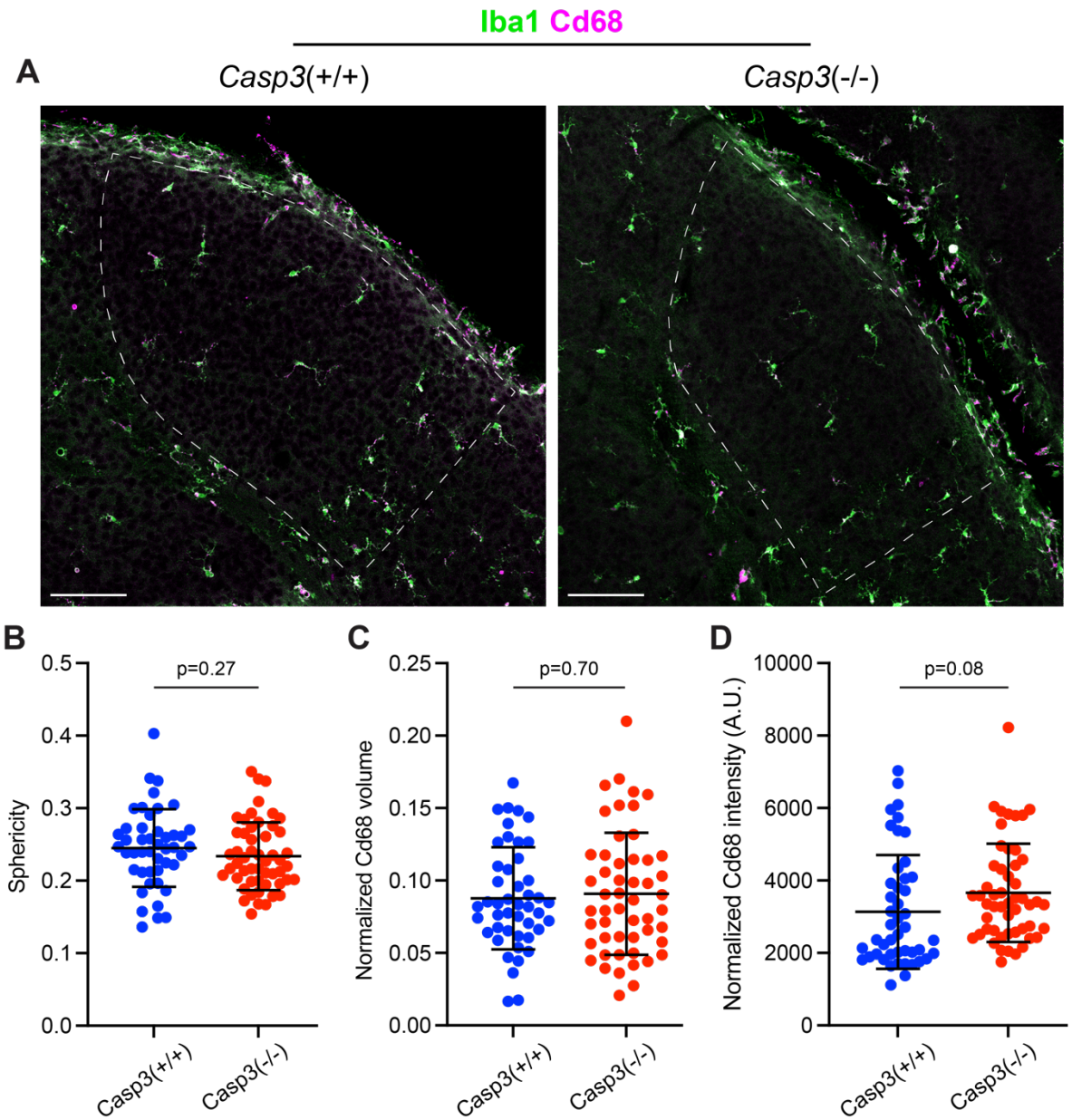

Figure S9. Caspase-3 deficiency does not cause microglia activation. (**A**) Representative images of P5 dLGNs in a *Casp3*$^{+/+}$ mouse (left) and a *Casp3*$^{-/-}$ mouse (right) showing Iba1 (green, a marker for microglia cell body) and Cd68 (magenta, a marker for microglia activation) staining. The dLGN areas are highlighted with dotted lines. Scale-bars represent 100 μm. (**B**) Quantification of microglia morphology in *Casp3*$^{+/+}$ and *Casp3*$^{-/-}$ mice using the sphericity metric. A sphericity of 1 corresponds to a perfect sphere. The smaller the sphericity is, the more ramified the cell is. (**C**-**D**) Quantification of microglia activation by normalizing the total volume of Cd68 signal (**C**) or the total intensity of Cd68 signal (**D**) in each microglia to the volume of that microglia. By both morphology and Cd68 signal, microglia in *Casp3*$^{-/-}$ mice show no evidence of activation. In **B**-**D**, each data point represents one microglia, and mean and S.D. are shown. n=46 microglia from 4 *Casp3*$^{+/+}$ mice and n=52 microglia from 4 *Casp3*$^{-/-}$ mice. P-values were calculated from two-tailed unpaired t-tests.

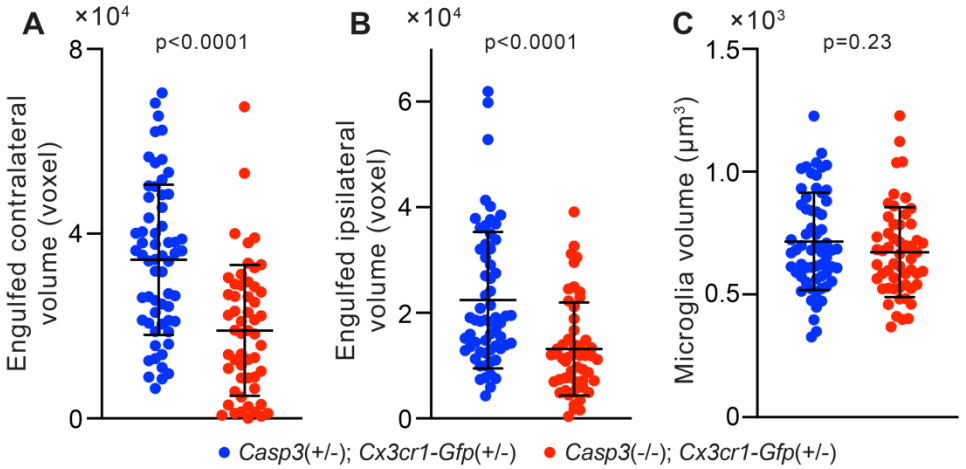

Figure S10. Additional analyses of microglia-mediated engulfment of synaptic material. (**A**-**B**) Volume of contralateral (**A**) and ipsilateral (**B**) RGC axon terminals engulfed by individual microglia in the P5 dLGN of *Casp3*$^{+/-}$; *Cx3cr1-Gfp*$^{+/-}$ and *Casp3*$^{-/-}$; *Cx3cr1-Gfp*$^{+/-}$ mice. (**C**) Volume of individual microglia in the P5 dLGN of *Casp3*$^{+/-}$; *Cx3cr1-Gfp*$^{+/-}$ and *Casp3*$^{-/-}$; *Cx3cr1-Gfp*$^{+/-}$ mice. In **A**-**C**, each point represents one microglia. Mean and S.D. are shown. P-values were calculated from unpaired two-tailed t-tests. n=61 microglia from 8 *Casp3*$^{+/-}$; *Cx3cr1-Gfp*$^{+/-}$ mice and n=54 microglia from 5 *Casp3*$^{-/-}$; *Cx3cr1-Gfp*$^{+/-}$ mice.

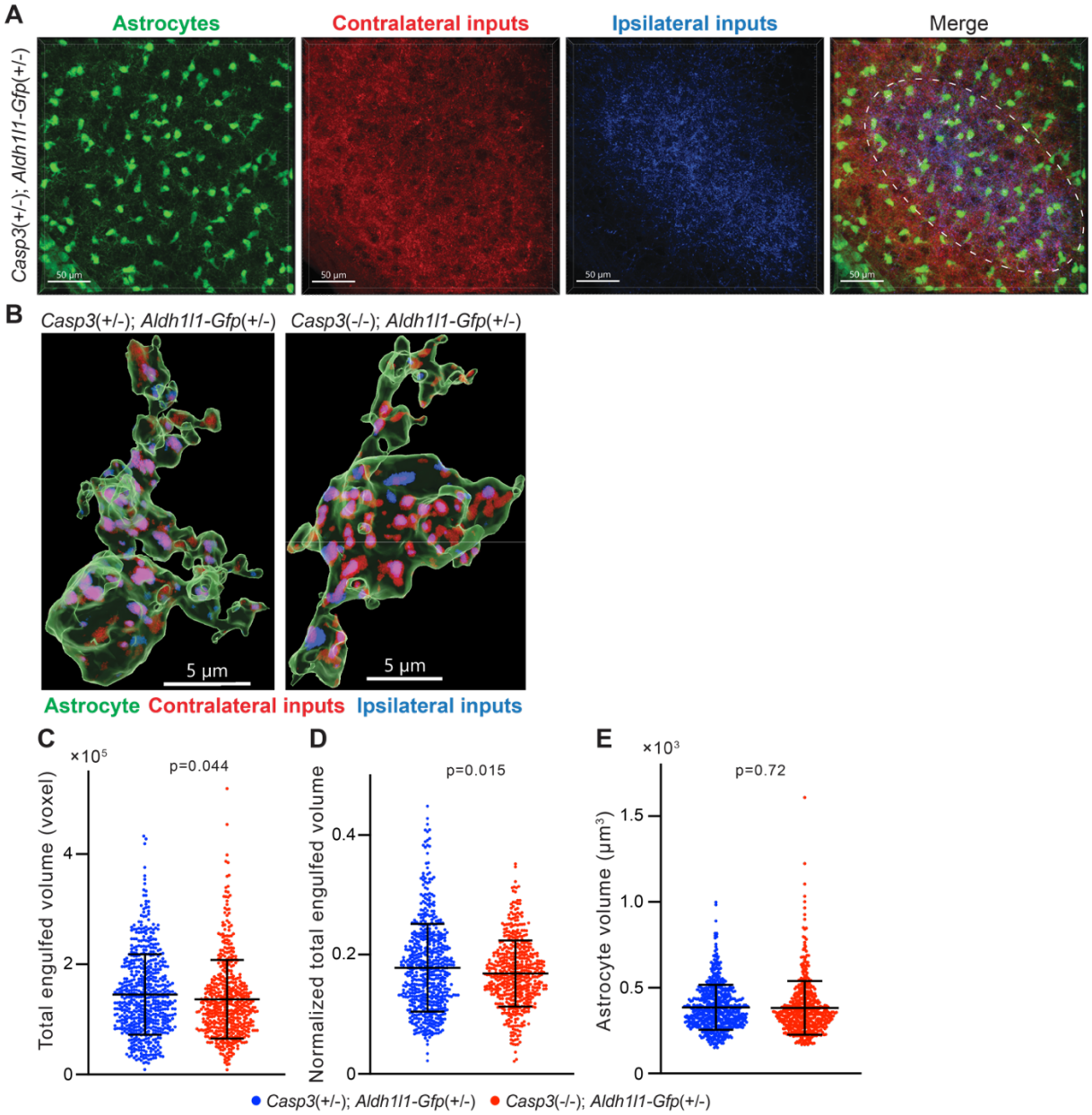

Figure S11. Astrocyte-mediated synapse elimination does not appear to depend on caspase-3. (**A**) Representative 3D-reconstructed images of a P5 *Casp3*$^{+/-}$; *Aldh1l1-Gfp*$^{+/-}$ mouse dLGN with astrocytes displayed in green, contralateral RGC axon terminals in red, and ipsilateral RGC terminals in blue. The region from which astrocytes are selected for analysis is indicated with the dashed line in the merged image. Scale-bars represent 50 µm. (**B**) Representative surface rendering of astrocytes (green) from P5 dLGNs of *Casp3*$^{+/-}$; *Aldh1l1-Gfp*$^{+/-}$ and *Casp3*$^{-/-}$; *Aldh1l1-Gfp*$^{+/-}$ mice. Intracellular contralateral (red) and ipsilateral (blue) RGC axon terminals are shown. Only cell bodies and the base of processes were segmented. We made this segmentation choice because we observed that fine astrocytic processes are largely devoid of engulfed material. Scale-bars represent 5 µm. (**C**) Total volume of engulfed synaptic material in individual astrocytes from *Casp3*$^{+/-}$; *Aldh1l1-Gfp*$^{+/-}$ and *Casp3*$^{-/-}$; *Aldh1l1-Gfp*$^{+/-}$ mice. (**D**) Total volume of engulfed synaptic material in each astrocyte (from **C**) is normalized to the volume of that astrocytes. (**E**) Volume of individual astrocytes from the two groups of mice. In **C**-**E**, each point represents one astrocyte. Mean and S.D. are shown. P-values were calculated from unpaired two-tailed t-tests. n=595 astrocytes from 8 *Casp3*$^{+/-}$; *Aldh1l1-Gfp*$^{+/-}$ mice and n=517 astrocytes from 6 *Casp3*$^{-/-}$; *Aldh1l1-Gfp*$^{+/-}$ mice.

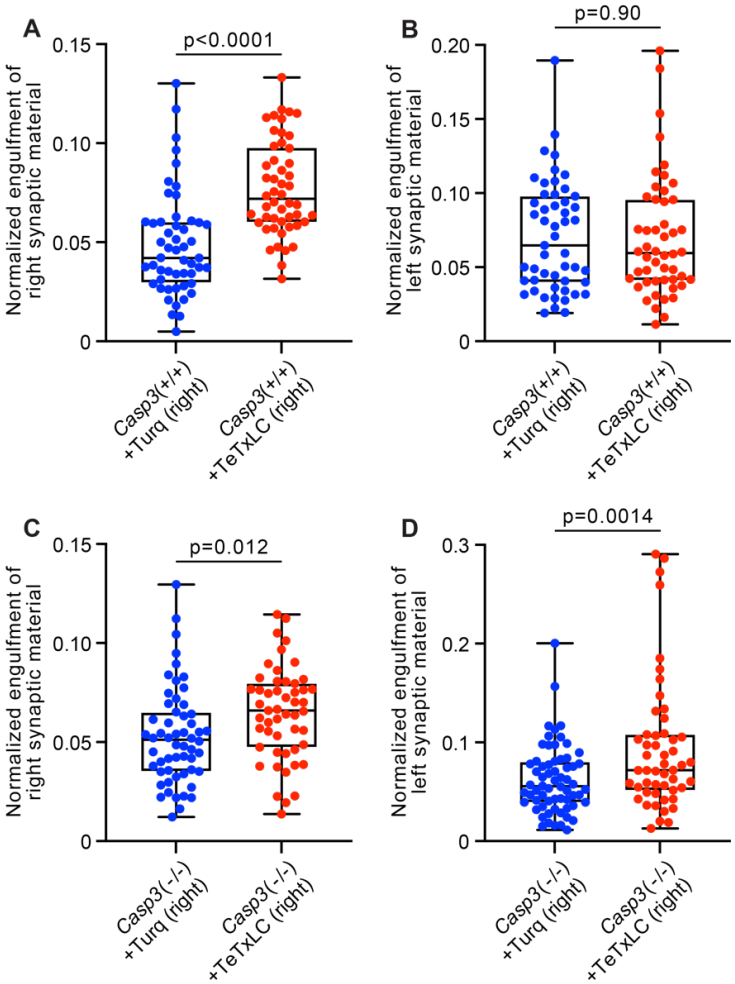

Figure S12. Additional analysis on activity-dependent microglia-mediated engulfment of synapses. (**A**-**D**) Volumes of synaptic material originating from right (**A** and **C**) or left (**B** and **D**) eyes engulfed by individual microglia from the left dLGN of *Casp3*$^{+/+}$ (**A**-**B**) or *Casp3*$^{-/-}$ (**C**-**D**) mice injected with AAV expressing mTurquoise2 (blue) or TeTxLC (red) in right eye were normalized to microglial volume and plotted. In *Casp3*$^{+/+}$ mice, inactivating right eye-originated retinogeniculate synapses specifically enhanced microglia-mediated engulfment of RGC axon terminals from right eyes (**A**) but not left eyes (**B**), resulting in significantly higher engulfment ratios (Fig. 6F). In *Casp3*$^{-/-}$ mice, inactivating right eye-originated synapses upregulated engulfment of RGC terminals from both eyes (**C** and **D**), resulting in no significant change in engulfment ratios (Fig. 6G). In **A**-**D**, 0, 25, 50, 75, and 100 percentiles are shown. p-values were calculated from unpaired two-tailed t-tests. n=52 microglia from 7 Turq-injected *Casp3*$^{+/+}$ mice, n=50 microglia from 8 TeTxLC-injected *Casp3*$^{+/+}$ mice, n=64 microglia from 5 Turq-injected *Casp3*$^{-/-}$ mice, and n=51 microglia from 6 TeTxLC-injected *Casp3*$^{-/-}$ mice. ***Notes on interpretation of C and D***: We observed that in *Casp3*$^{-/-}$ brains, particularly those injected with TeTxLC, microglia in dLGNs tended to increase in volume and have thicker processes. We therefore suspect the non-specific upregulation of synapse engulfment in TeTxLC-injected *Casp3*$^{-/-}$ mice is a consequence of microglial activation rather than synapse inactivation. This microglial activation is likely a ramification of intraocular surgeries, as changes in microglia morphology was more prominent in the left dLGN that received most of the inputs from AAV-injected right eyes, and microglia outside of dLGNs did not show characteristics of activation. We noticed that *Casp3*$^{-/-}$ brains tended to have weak structural integrity. It is likely that repetitive intraocular injections caused damage in the retinogeniculate pathway of *Casp3*$^{-/-}$ mice and activated microglia. Nevertheless, by calculating right-to-left engulfment ratios, substrate preference of microglia in TeTxLC-injected *Casp3*$^{-/-}$ mice can be deduced.

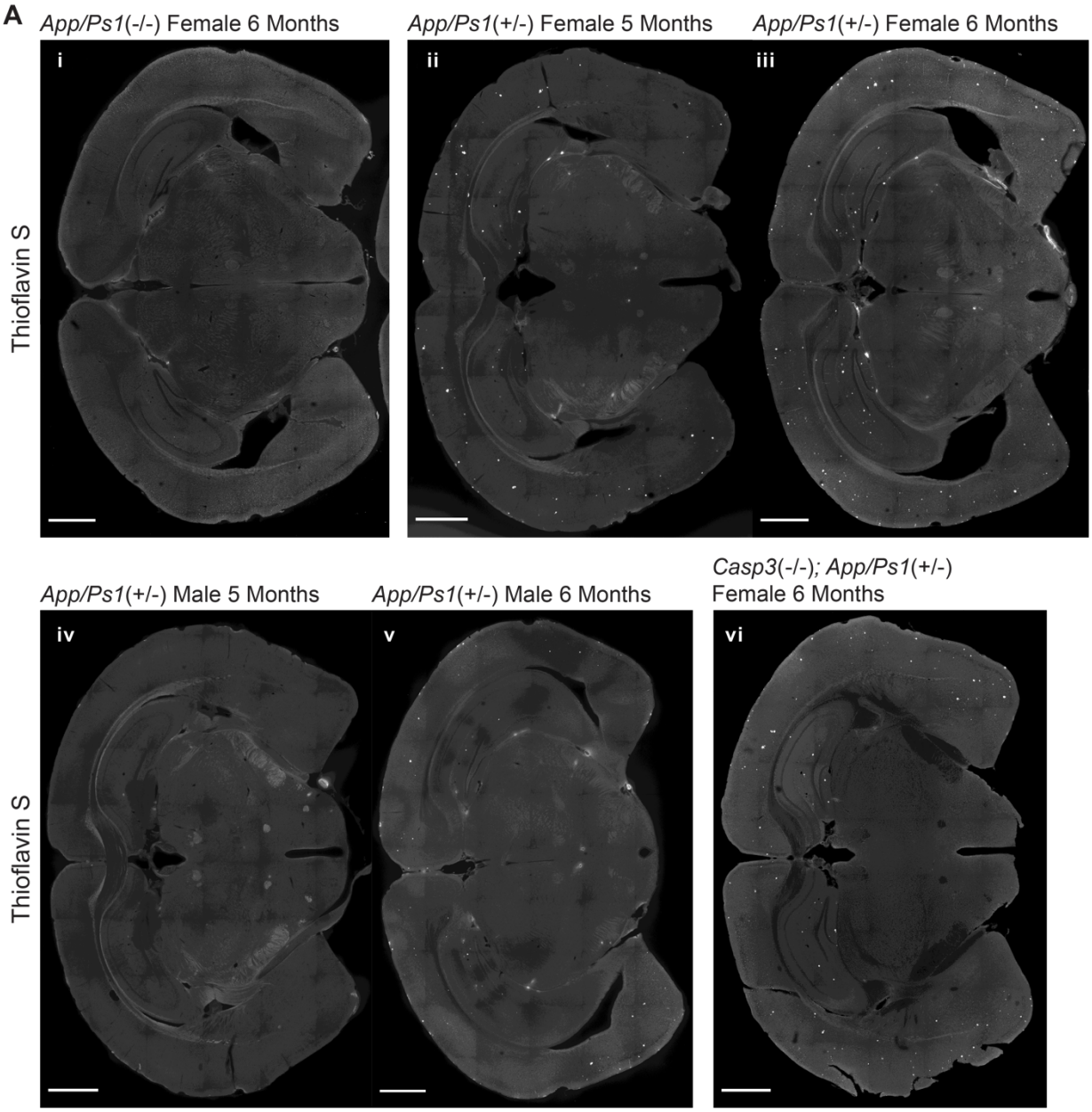
A
App/Ps1(-/-) Female 6 Months
App/Ps1(+/-) Female 5 Months
App/Ps1(+/-) Female 6 Months
Thioflavin S
i
ii
iii
App/Ps1(+/-) Male 5 Months
App/Ps1(+/-) Male 6 Months
Casp3(-/-); App/Ps1(+/-)
Female 6 Months
Thioflavin S
iv
v
vi

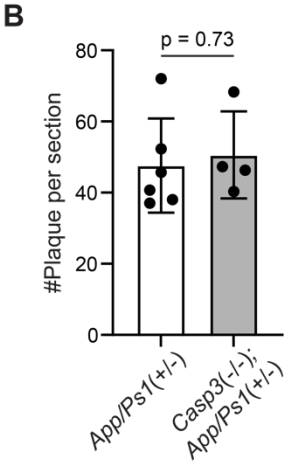
B
p = 0.73
#Plaque per section
0
20
40
60
80
App/Ps1(+/-)
Casp3(-/-);
App/Ps1(+/-)

Figure S13. Amyloid deposition APP/PS1 mouse lines. (**A**) Images of coronal brain sections of a female *App/Ps1*$^{-/-}$ mouse at 6 months (i), female *App/Ps1*$^{+/-}$ mice at 5 months (ii) or 6 months (iii), male *App/Ps1*$^{+/-}$ mice at 5 months (iv) or 6 months (v), and a female *Casp3*$^{-/-}$; *App/Ps1*$^{+/-}$ mouse at 6 months, stained with Thioflavin S to reveal Aβ plaques (bright spots in hippocampus and cortex). Scale-bars represent 1 mm. (**B**) Quantification of the number of plaques per section in female 6 month-old *App/Ps1*$^{+/-}$ and *Casp3*$^{-/-}$; *App/Ps1*$^{+/-}$ mice. Mean and S.D. are shown. p-values were calculated with unpaired two-tailed t-tests. n=6 for *App/Ps1*$^{+/-}$ mice and n=4 for *Casp3*$^{-/-}$; *App/Ps1*$^{+/-}$ mice.

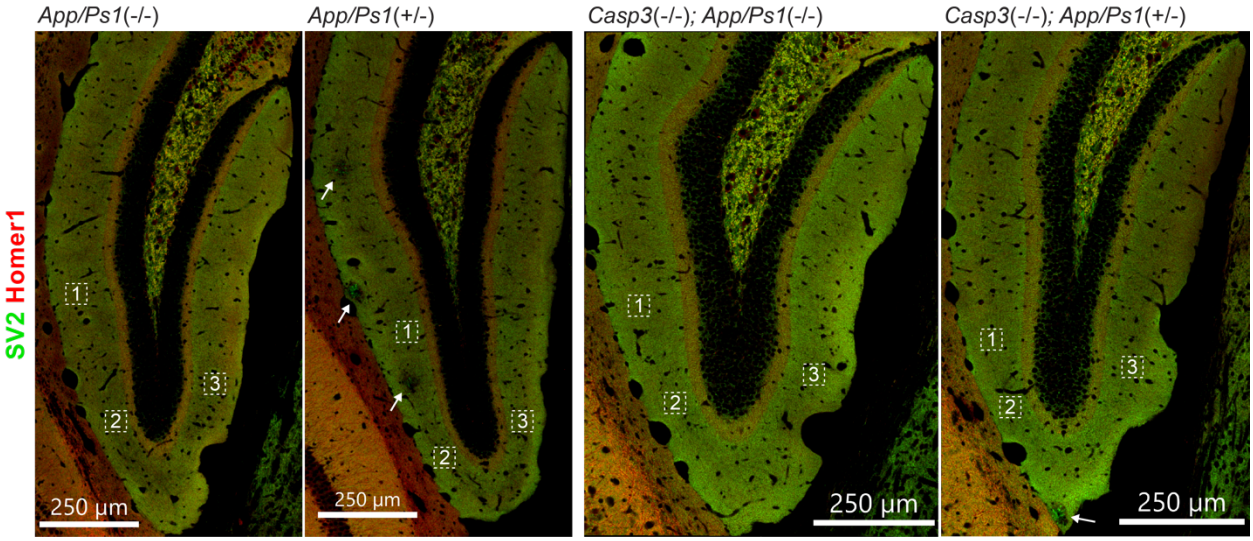

Figure S14. Selection of field of interest for synapse loss analysis. To quantify synapse density, three regions of interest from each dentate gyrus on either side of the brain were chosen for each animal (total of 6 regions per animal). Regions of interest in one dentate gyrus of one animal from each genotype group are highlighted with dotted squares in the overviews above. High resolution images of SV2 (in green) and Homer1 (in red) stains were acquired for each region of interest and used for analysis. In sections from animals overexpressing mutant APP and PS1, we avoided choosing regions of interest from areas surrounding amyloid plaques (highlighted with arrows).

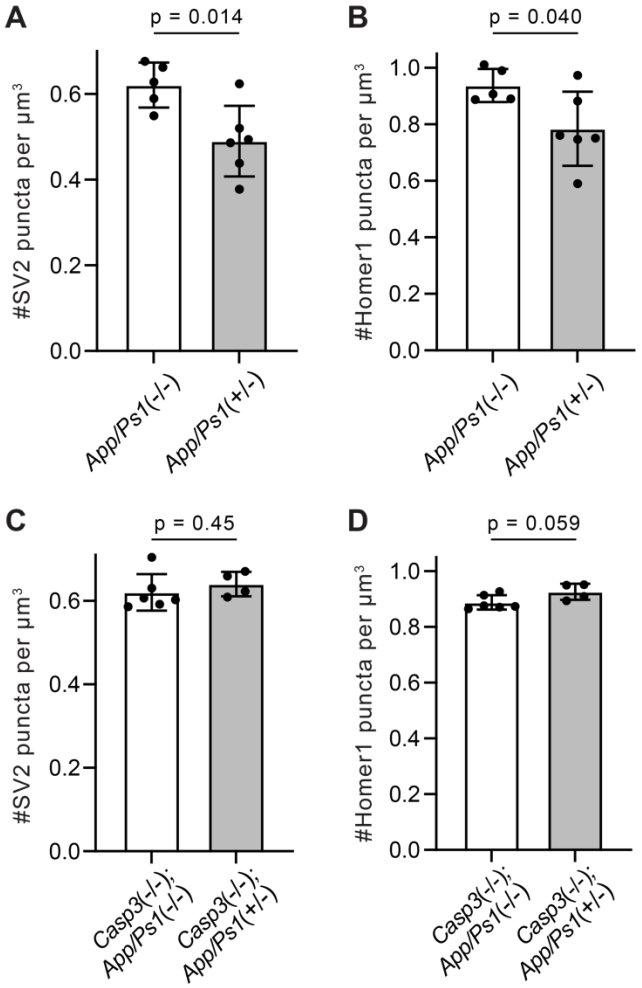

Figure S15. Additional analysis of synapse density in APP/PS1 mouse lines. (**A**-**D**) Quantification of presynaptic (**A** and **C**) and postsynaptic (**B** and **D**) puncta densities in the dentate gyrus of APP/PS1 mice in the caspase-3 wildtype (**A** and **B**) or deficient (**C** and **D**) background. Mean and S.D. are shown. p-values were calculated from unpaired two-tailed t-tests. n=5 for *App/Ps1*$^{-/-}$ mice, n=6 for *App/Ps1*$^{+/-}$ mice, n=6 for *Casp3*$^{-/-}$; *App/Ps1*$^{-/-}$ mice, and n=4 for *Casp3*$^{-/-}$; *App/Ps1*$^{+/-}$ mice.

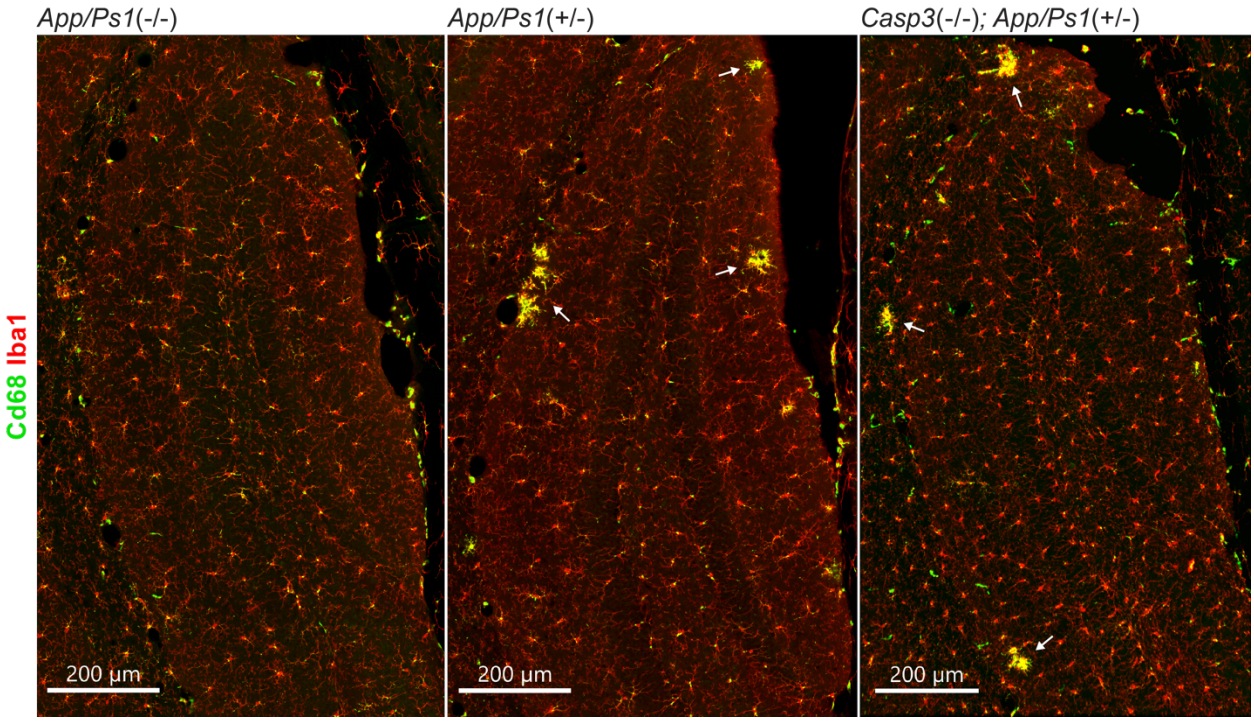

Figure S16. Microgliosis in APP/PS1 mouse lines. Coronal sections from 6 month-old female *App/Ps1*$^{-/-}$ (left), *App/Ps1*$^{+/-}$ (middle), and *Casp3*$^{-/-}$; *App/Ps1*$^{+/-}$ (right) mice were stained for Iba1 (red, to detect microglia) and Cd68 (green, as a microglia activation marker). Dentate gyrus regions are shown in the overviews above. Clusters of reactive microglia surrounding amyloid plaques are highlighted with arrows.

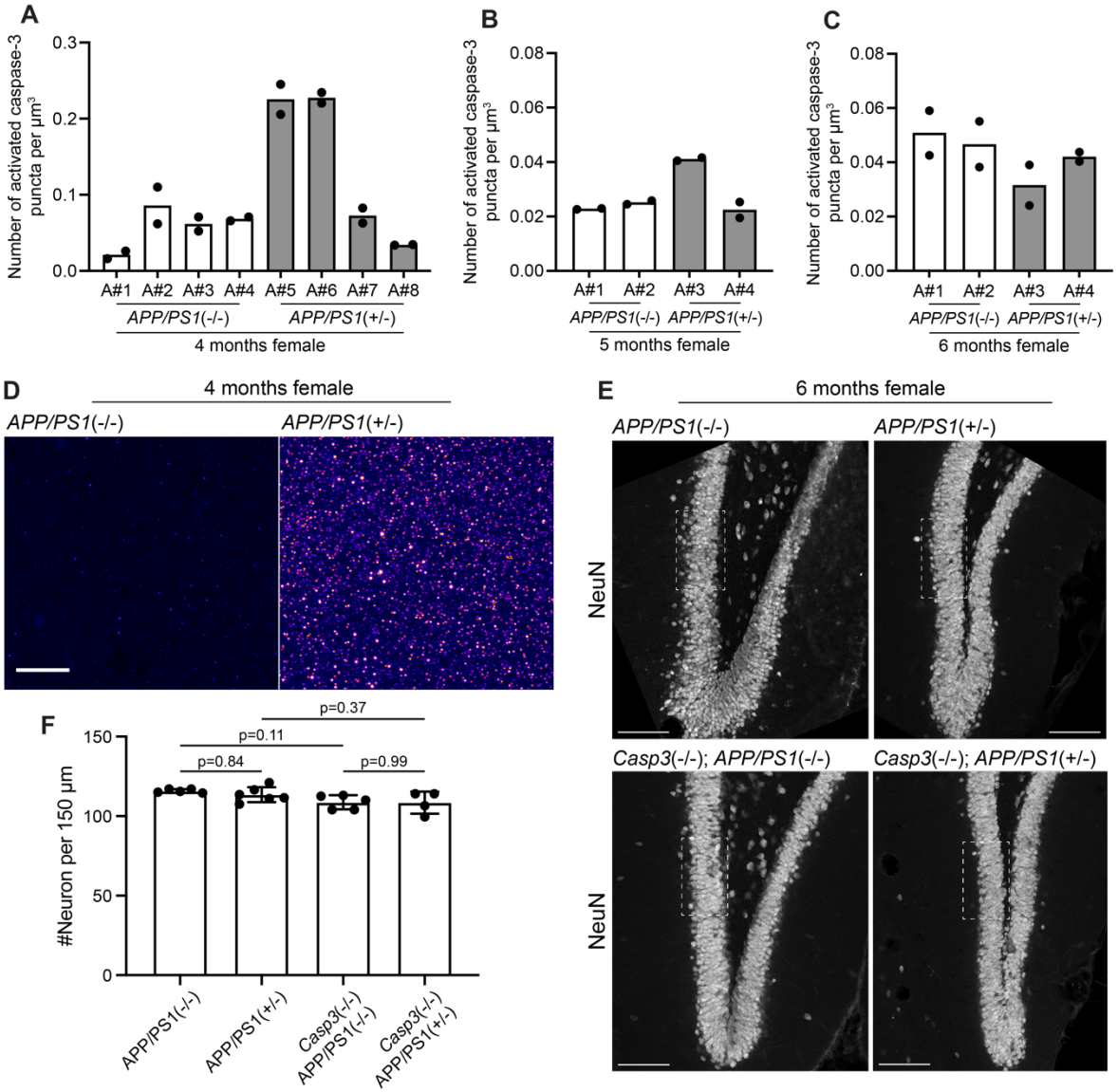

Figure S17. Aβ-induced caspase-3 activity in APP/PS1 mice. (**A**-**C**) Density of activated caspase-3 puncti in the dentate gyrus of 4 month-old (**A**), 5 month-old (**B**), and 6 month-old (**C**) female *App/Ps1*$^{-/-}$ and *App/Ps1*$^{+/-}$ mice. Each column represents one animal, and each dot represent quantification from one dentate gyrus (either from left side or right side). Two out of four 4-month-old *App/Ps1*$^{+/-}$ mice showed robustly upregulation of caspase-3 activity in the dentate gyrus (**A**). No upregulation of caspase-3 activity was observed in 5 month-old or 6 month-old mice. (**D**) Images showing elevated caspase-3 activity in the molecular layer of the dentate gyrus of a 4 month-old female *App/Ps1*$^{+/-}$ mouse (A#5 in **A**). Images were set to the same intensity contrast. Upregulated caspase-3 activity remained in a punctate pattern and no apoptotic cell was observed. Scale-bar represents 10 μm. (**E**) Representative images of the dentate gyrus in 6 month-old female *App/Ps1*$^{-/-}$, *App/Ps1*$^{+/-}$, *Casp3*$^{-/-}$; *App/Ps1*$^{-/-}$, and *Casp3*$^{-/-}$; *App/Ps1*$^{+/-}$ mice that were stained with an anti-NeuN antibody to visualize neurons. The fields of interest used to quantify neuron density are highlighted with dotted rectangles. Scale-bars represent 100 μm. (**F**) Neuron density in the granule cell layer of the dentate gyrus in the four groups of mice shown in **E**. Neither caspase-3 deficiency nor APP/PS1 overexpression caused significant changes in neuron density. Mean and S.D. are shown. p-values were calculated from Tukey's multiple comparisons test. n=5 for *App/Ps1*$^{-/-}$ mice, n=6 for *App/Ps1*$^{+/-}$ mice, n=5 for *Casp3*$^{-/-}$; *App/Ps1*$^{-/-}$ mice, and n=4 for *Casp3*$^{-/-}$; *App/Ps1*$^{+/-}$ mice.

Material and methods

Mouse lines

The *Casp3*$^{-/-}$ mouse line was a generous gift from Dr. Richard Flavell. This mouse line was received as cryopreserved sperm and was rederived using C57Bl/6J oocytes. The resulting colony was maintained by continuous backcrossing to C57Bl/7J mice. We verified that mice in our *Casp3*$^{-/-}$ colony were congenic to the C57Bl/6J background (greater than 99% identity by SNP analysis). It is important to note that regular backcrossing is necessary to maintain phenotype stability in *Casp3*$^{-/-}$ mice. A small fraction of *Casp3*$^{-/-}$ mice displayed varying degrees of hydrocephalus. These animals were excluded from our analyses. *Cx3cr1-Gfp* mice (stock number 005582) were obtained from the Jackson laboratory. *Aldh1l1-Gfp* transgenic mice (stock number 011015-UCD) were obtained from Mutant Mouse Resource and Research Centers (MMRRC) as cryopreserved sperm and rederived using C57Bl/6J oocytes. *App/Ps1* mice were obtained from the Jackson laboratory (stock number 034832). Mice carrying *App/Ps1* transgenes were given DietGel® 76A (ClearH_2O, 72-07-5022) and were euthanized at the age of 6 months if not used in experiments. For experiments associated with Figure 1 and Figure 2, C57Bl/6NCrl mice were obtained from Charles Rive Laboratories (strain code 027). For experiments associated with Figure 6, C57Bl/6J mice were obtained from the Jackson Laboratory (stock number 000664). All animal procedures were carried out according to IACUC approved protocols.

Reagents

22 Reagents were obtained from the following sources: isoflurane liquid (NDC 50989-
23 150-15) was from Vedco; phosphate buffered saline without calcium and magnesium
24 (PBS^-, BP2438) was from Fisher Scientific; bicuculline (0130) and cyclothiazide (0713)
25 were from Tocris Bioscience; PBS with calcium and magnesium (PBS^+, SH30264) was
26 from Cytiva; dimethyl sulfoxide (DMSO, D2650), bovine serum albumin (BSA, A9647),
27 triton X-100 (T8787), Thioflavin S (T1892) were from Millipore-Sigma; paraformaldehyde
28 powder (19200) was from Electron Microscopy Science; RPMI 1640 medium (11875093),
29 DMEM medium (11965092), fetal bovine serum (FBS, 16000044), penicillin/streptomycin
30 (pen/strep, 15140122), CD Hybridoma medium (11279023), GlutaMAX supplement
31 (35050061), protein A/G agarose beads (20421), protein A/G IgG binding buffer (54200),
32 IgG elution buffer (21004), 1M Tris-HCl pH 8.0 (15568025), 10% normal goat serum
33 (50062Z), ProLong™ Gold mounting medium (P36934), Alexa Fluor 546 succinimidyl
34 ester (A20002), cholera toxin subunit beta(CTB) conjugated to AlexaFlour (AF) 488,
35 AF555, AF594 and AF647 (C22841, C22842, C22843, C34778), goat anti-rabbit
36 secondary antibodies conjugated to AF488plus (A32731), AF555plus (A32732),
37 AF594plus (A32740), and AF647plus (A32733), goat anti-chicken secondary antibody
38 conjugated to AF488plus (A32931), goat anti-guinea pig secondary antibody conjugated
39 to AF488 (A11073) and AF594 (A11076) were from ThermoFisher Scientific; anti-cleaved
40 caspase-3 antibody (9661) was from Cell Signaling Technologies; anti-GFP antibody
41 (GFP-1010) was from Aves Lab; anti-MAP2 antibody (NB300-213) was from Novus
42 Biologicals; anti-NeuN antibody (266004) was from Synaptic Systems; anti-RBPMS
43 antibody (1832-RBPMS) was from PhosphoSolutions; anti-Iba1 (ab178846) and anti-
44 Homer1 (Ab97593) antibodies were from Abcam; anti-Cd68 antibody (MCA1957) was

45 from Bio-Rad; hybridoma line producing anti-SV2 antibody (clone name SV2) was from
46 DSHB.

47 **DNA cloning and AAV preparation**

48 To make the pAAV-hSyn-mTurquoise2 plasmid, we ordered the DNA fragment for
49 mTurqouise2 (*1*) as a Gblock from IDT and cloned it via isothermal assembly into a
50 linearized AAV expression plasmid (derived from pAAV-Syn-iCre; Addgene #122518)
51 under the control of human synapsin promoter. To make the pAAV-hSyn-TeTxLC-P2A-
52 mTurqouise2 plasmid, the tetanus toxin light chain (TeTxLC) sequence along with the
53 P2A sequence (2A peptide from porcine teschovirus-1 polyprotein) at the 3' end was
54 obtained via PCR from Addgene plasmid #129102 and fused in-frame with the
55 mTurquoise2 DNA sequence in the same plasmid backbone as the pAAV-hSyn-
56 mTurquoise2 plasmid. Note that in the main text, we used pAAV-hSyn-TeTxLC to refer to
57 pAAV-hSyn-TeTxLC-P2A-mTurquoise2 because AAV carrying this plasmid induced very
58 low levels of mTurquoise2 expression *in vivo*. When we needed endogenous florescence
59 labeling, we chose to premix AAV carrying pAAV-hSyn-TeTxLC-P2A-mTurquoise2 with
60 other AAVs expressing fluorescent proteins (at 1:1 ratio).

61 The pAAV-hSyn-tdTomato plasmid was cloned and provided by Janelia Viral Tools. The
62 pAAV-CAG-GFP plasmid was previously made by Svoboda lab and is available as
63 Addgene #28014.

64 The recombinant AAVs were prepared by Viral Tools of Janelia Core Services. Briefly, two
65 days before transfection, 293T cells were seeded in three 150 mm T/C dishes at 1 x 10^7
66 cells/dish in DMEM medium supplemented with 10% FBS and cultured at 37 °C with 5%

67 CO_2. The cells were transfected with 84 µg of pAAV plasmid, DJ capsid plasmid (*2*), and
68 pHelper plasmid (Agilent 240071) at a ratio of 5:2:3 in polyethylenimine. After 6 to 8 hours,
69 the cells were replenished with serum-free DMEM and further incubated for 3 days. The
70 recombinant AAVs were collected from both the cells and supernatant and purified by two
71 rounds of continuous cesium chloride density gradient centrifugation, dialyzed,
72 concentrated, and filter sterilized. Titer (genome copies per ml) was determined by digital
73 PCR with primers targeting the ITR. For all in vivo experiments a titer of at least 10^{13}
74 genome copies/ml was used.

75 **Intraocular injections**

76 *In utero* intraocular injections were performed as previously described (*3*) with
77 modifications. Briefly, pregnant mouse females with embryos at E15 gestation were
78 anesthetized by 3% isoflurane inhalation, abdomens shaved, eye lube applied to each
79 eye, then transferred to a nose cone and set to maintenance level of 2% isofluorane
80 inhalation anesthesia. Warm fluids (lactated Ringer's solution + 5% dextrose, Strategic
81 Applications Inc.), Buprenorphine (0.1 mg/kg, Butler Animal Health), and Ketoprofen (5
82 mg/kg, Covetrus) were administered subcutaneously just prior to starting surgery. The
83 animal was placed in dorsal recumbency, and the abdomen was cleansed using
84 alternating swabs of 70% ethanol and 4% Chlorhexidine Gluconate (Molnlycke Health
85 Care). A sterile drape was placed over the abdomen and using aseptic technique, the
86 abdominal skin and wall were cut at midline, before gently removing the uterus from the
87 abdomen. While keeping the uterus/embryos hydrated with warm saline sterile solution,
88 the embryos were gently positioned with ring forceps to hold each embryo securely for
89 injection. A previously filled glass pipette (Drummond Scientific), beveled to 30-40 µm at

90 the opening was utilized to deliver constructs utilizing a pre-programmed Nanoject III
91 microinjector (Drummond Scientific). 200-250 nl of AAVs prep was injected through the
92 uterine wall and into each eye at a speed of 50nl per second. To confirm proper targeting
93 within the eye, the AAV solution was pre-mixed with 0.05% Fast Green (Sigma Aldrich).
94 After all injections were completed, the uterus/embryos were carefully placed back into
95 the abdomen and the abdomen was flushed with warm sterile saline. The abdominal wall
96 and skin were sutured, and Marcaine (Hospira) was applied subcutaneously below the
97 skin incision. A small drop of Vetbond (3M) was applied to seal the skin incision. The
98 animal was then removed from the anesthesia apparatus and allowed to recover on a
99 heating pad before being placed back into a clean cage.

100 For intraocular injection at P4 and P9, pups with desired genotypes were
101 anesthetized in an induction chamber filled with 2.5% - 3% isoflurane using a calibrated
102 vaporizer. After the onset of anesthesia, isoflurane is reduced to 1.25%, and the mouse
103 was removed from the chamber and placed under a dissection microscope. Proparacaine
104 ophthalmic solution (0.5%, Sandoz, NDC 61314-016-01) was applied to each eye to be
105 injected. A re-breathing nose cone was used to deliver 1.25% – 2% isoflurane throughout
106 the procedure. A gentle blunt dissection was performed at each eyelid junction utilizing
107 closed No.5 Dumont forceps (Fine Science Tools) to create a 2-3 mm opening. A 33-
108 gauge sharp beveled needle attached to a Hamilton microliter syringe (Hamilton
109 Company) was used to draw up CTB-AF solutions. Just prior to injecting, the eye was
110 proptosed and held securely in place by the Dumont forceps in preparation for injection.
111 While holding the eye securely in place, the sclera was punctured with the Hamilton
112 needle at the level of the ora serrata to inject 2.5 μL (for P9) or 2 μL (for P4) of desired

113 CTB-AF solution into each eye. After the injection, eye lube was applied, the eye was
114 allowed to move back into the socket, and the eyelids were gently pressed close to protect
115 the eye. Pups were allowed to recover from anesthesia on a heated pad and put back
116 into the cage with the dam.

117 **Monoclonal antibody production and labeling**

118 SV2 hybridoma cells were thawed and seeded in RPMI 1640 medium containing
119 10% FBS and 1% Pen/Strep at 0.3 million cells/ml and cultured in an incubator at 37 ˚C
120 with 5% CO_2. After reaching $1x10^6$ viable cells/ml density, the cells were diluted 1:2 by
121 adding an equal volume of serum free CD Hybridoma medium supplemented with 4%
122 GlutaMax^{Tm} and returned to the incubator. This dilution process was repeated 2 more
123 times so that the cells reached $1x10^6$ viable cells/ml density in a mixed medium containing
124 ~1% FBS. Cell viability obtained was at least 90%. The cells were then spun down at
125 150xG for 10 minutes and resuspended in complete CD Hybridoma medium at $5x10^5$
126 cells/ml density. The cells were further expanded by adding more complete CD
127 Hybridoma medium when cells reach $1x10^6$ cells/ml density. Once the desired total
128 volume is reached (typically 100 ml), cells were cultured for 2 weeks without medium
129 change.

130 Culture supernatant containing SV2 antibody was cleared of hybridoma cells by
131 centrifuging at 1000xG for 10 min. Cleared supernatant was diluted 1:1 with IgG binding
132 buffer and passed through 1 ml of protein A/G agarose bead slurry (ThermoFisher 20421,
133 corresponding to 500 ul of settled resin) packed in a gravity flow column. The column was
134 washed with IgG binding buffer, and SV2 antibody was eluted in five 1 ml fractions using
135 IgG elution buffer and immediately neutralized with 10% volume of 1M Tris-HCl, pH 8.0.

136 Fractions with highest antibody concentration were pooled, desalted with Zeba columns
137 (ThermoFisher 89891), and concentrated to ~1 mg/ml using Amicon centrifuge filters
138 (Millipore UFC801024). After adding glycerol (25% final), antibodies were flash frozen in
139 liquid nitrogen and kept at -80 ˚C.

140 To label the primary SV2 antibodies, we used Alexa Fluor 546 succinimidyl ester.
141 Briefly, we buffer-exchanged and concentrated SV2 IgG to 3 mg/ml using Amicon filters
142 (UFC501024 Millipore Sigma) in phosphate buffered saline that was brought to pH 8.3
143 with 100 mM $NaHCO_3$. Dimethyl sulfoxide-dissolved Alexa Flour 546 succinimidyl ester
144 was gently mixed with the SV2 IgG at 10:1 molar ratio and incubated for two hours at
145 room temperature on a rotating shaker. Alexa Fluor 546 labeled IgG were purified from
146 unreacted succinimidyl esters with the aid of PD MiniTrap Sephadex G-25 column (Cytiva
147 28918007) in PBS^- by gravity flow following the manufacturer's instructions. The degree
148 of labeling was determined by spectrophotometry on Nanodrop One (ThermoFisher) by
149 accounting for the Alexa Fluor 546 extinction coefficient at 554 nm and the corrected
150 protein absorbance at 280 nm. Typically, a degree of labeling of 8-9 mols of dye per mol
151 of protein was obtained. Labeled SV2 were aliquoted and flash-frozen in 25% glycerol for
152 long term storage at -80 ˚C at a final concentration of approximately 0.75 mg/ml.

153 **Immunohistochemistry**

154 The mice were deeply anesthetized in a chamber filled with saturating isoflurane
155 gas and transcardially perfused first with PBS^- and then with paraformaldehyde (PFA)
156 solution (4% w/v in 20.3 mM NaH_2PO_4 and 79.7 mM Na_2HPO_4, pH = 7.4). The brains
157 were removed and post-fixed in 4% PFA solution overnight at 4 ˚C with gentle shaking.

158 Fixed brains were washed 3x15 minutes in PBS^- at room temperature and stored in PBS^-
159 at 4 ˚C. For long term storage, fixed brains were cryoprotected in 30% Sucrose (w/v in
160 PBS^-) for 72 hours and frozen in Tissue-Tek® O.C.T. compound (Sakura) and stored at -
161 80 ˚C.

162 Brains stored in PBS^- were imbedded in 4% agarose, and coronal sections (50 um
163 thick for mice younger than P10 or 40 μm thick for adult mice) were prepared using a
164 vibratome (Leica VT 1200S). For brains frozen in O.C.T. compound, coronal sections
165 were prepared using a cryostat (Leica 3050S). Sections were floated in 24-well plates in
166 PBS^- and stored at 4 ˚C. For antibody staining, free-floating sections were first
167 permeabilized/blocked in 10% normal goat serum containing 0.3% (w/v) triton X-100 for
168 1 hour. The sections were then incubated with primary antibodies diluted in staining buffer
169 (PBS^+ containing 2% BSA w/v and 0.3% triton X-100) at 4 ˚C overnight with gentle
170 agitation. Dilutions of primary antibodies were: anti-cleaved caspase-3, 1:500; anti-GFP,
171 1:2000; anti-MAP2, 1:1000; anti-NeuN, 1:500; anti-Iba1, 1:500; anti-Cd68, 1:500; anti-
172 SV2, dilute to 2.5 μg/ml; anti-Homer1, 1:400. The sections were then washed 3x15
173 minutes in washing buffer (PBS^+ containing 0.1% triton X-100) and stained with
174 appropriate fluorophore-conjugated secondary antibodies diluted in staining buffer for 3
175 hours at room temperature with gentle agitation. Secondary antibodies were always used
176 at 1:500 dilution. The sections were washed 3x15 minutes in washing buffer, rinsed 3x5
177 minutes in PBS^+, and mounted onto glass slides (Fisher, 12-550-15). After air-drying
178 completely, mounted sections were immersed in ProLong™ Gold and coverslipped
179 (Fisher, 12-541-024). The sections were imaged after 24 hours of curing at room
180 temperature. The sections were protected from light during the entire process.

181 To prepare whole-mount retinae, eyes were removed from PFA perfused mice and
182 placed in PBS^-. The cornea was punctured with a #11 scalpel, and several anterior-to-
183 posterior cuts were made on the sclera starting from the puncture. Intact retinae were
184 isolated by tearing and peeling off the sclera along the cuts. 4 to 5 radial cuts were made
185 on each retina to flatten the tissue. Isolated retinae were post-fixed for 15 minutes in 4%
186 PFA solution at room temperature with gentle agitation and washed for 3x5 minutes in
187 PBS^- at room temperature with gentle agitation. Free-floating retinae were then stained
188 with primary (anti-RBPMS antibody, used at 1:200 dilution) and secondary (goat anti-
189 guinea pig Alexa Fluor 594plus) antibodies and mounted onto glass slides as described
190 above.

191 For staining of amyloid-β (Aβ) plaques, a 1% Thioflavin S stock solution (w/v,
192 dissolved in ddH_2O) was diluted 100-fold in 50% ethanol (prepared by mixing pure ethanol
193 and ddH_2O at 1:1 ratio) to create a 0.01% (w/v) working solution. The stock and working
194 solutions were discarded after each use. Free-floating brain sections were dehydrated by
195 washing 2x5 minutes in 50% ethanol, stained in 0.01% Thioflavin S solution for 8 minutes,
196 washed for 2x5 minutes in 50% ethanol, then re-hydrated by washing 3x5 minutes in
197 PBS^+. All staining steps were performed at room temperature with gentle agitation. The
198 sections were protected from light throughout the procedure. Stained sections were then
199 mounted and cured as described above.

200 **Measuring synapse inactivation-induced caspase-3 activity**

201 For experiments associated with Figure 1 and Figure S4, E15 C57Bl/6NCrl mice
202 were injected in the right eyes either with AAV carrying hSyn-mTurquoise2 (control group),
203 or with a 1:1 mixture of AAV carrying hSyn-mTurquiose2 and AAV carrying hSyn-TeTxLC-

204 P2A-mTurquoise2 (synapse inactivation group). At the age of P5, brains of both groups
205 of mice were harvested and sectioned as described above. To quantify caspase-3 activity
206 in the dLGN and the localization of activated caspase-3 relative to TeTxLC-expressing
207 RGC axons (Figure 1), sections were stained with anti-cleaved caspase-3 antibody (using
208 goat anti-rabbit AF594plus as the secondary) and anti-GFP antibody (using goat anti-
209 chicken AF488plus as the secondary). Alternatively, sections were co-stained with anti-
210 cleaved caspase-3 (using goat anti-rabbit AF647plus as the secondary) and anti-MAP2
211 antibody (using goat anti-rabbit AF488plus as the secondary) (Figure S4A), or with anti-
212 cleaved caspase-3 (using goat anti-rabbit AF594plus as the secondary) and anti-NeuN
213 antibody (using goat anti-rabbit AF488plus as the secondary) (Figure S4C).
214 Immunostaining was performed as described above.

215 For experiments associated with Figure 2, E15 C57Bl/6NCrl mice were injected in
216 the left eyes with AAV carrying hSyn-tdTomato and in the right eyes with AAV carrying
217 CAG-eGFP (control group), or in the right eyes with AAV carrying hSyn-mTurquoise2 and
218 AAV carrying hSyn-TeTxLC-P2A-mTurquoise2 (single inactivation group), or in the left
219 eyes with AAV carrying hSyn-tdTomato and AAV carrying hSyn-TeTxLC-P2A-
220 mTurquoise2 and in the right eyes with AAV carrying CAG-eGFP and AAV carrying hSyn-
221 TeTxLC-P2A-mTurquoise2 (dual inactivation group). At the age of P5, brains of all three
222 groups of animals were harvested, sectioned, and stained with anti-cleaved caspase-3
223 antibody and goat antirabbit AF647plus secondary antibodies as described above.

224 To quantify caspase-3 activity in the dLGN (Figure 1B-E), confocal images of
225 dLGNs were acquired on a Leica Stellaris 8 microscope using a 10x/0.4 NA dry objective
226 (Leica HC PL Apo CS2 10x/0.4 dry). The channels were acquired sequentially (line-by-

227 line) with the anti-caspase-3 first and anti-mTurquoise2 second. A 590 nm laser and
228 emission read of 596 nm – 748 nm was used for the anti-cleaved caspase-3 channel, and
229 440 nm and 488 nm lasers and an emission read of 457 nm – 579 nm were used for anti-
230 mTurquoise2 channel. The imaging parameters (laser power, pixel dwell time, signal
231 averaging or accumulation) were set to maximize signal-to-background values while
232 avoiding detector (SiPM type Power HyD S) saturation. Photon detection was set in
233 counting mode and acquired as 12-bit images at 227 nm x 227 nm pixel size. All datasets
234 used for measurement of caspase-3 activity were acquired as Z-stacks (7 slices spaced
235 2.4 μm apart). To measure the total amount of active caspase-3 signal in the 3D stacks
236 of dLGN we used the Labkit (*4*) Fiji plugin to generate and train a pixel classifier through
237 Imaris v. 10 (Oxford Instruments). The same pixel classifier and surface creation settings
238 were applied to data from both the control and the synapse inactivation groups to
239 generate surface objects of active caspase-3 signal. All active caspase-3 objects found
240 within the dLGN area (manually delineated based on mTurquoise2 signal) were selected,
241 and the sum of voxel intensities the active caspase-3 objects was calculated and divided
242 by the area of dLGN. The final values plotted for each mouse are averages of two
243 consecutive sections.

244 To image active caspase-3 signals and TeTxLC-expressing RGC axons at high
245 resolution (Figure 1G), we used a Leica Stellaris 8 confocal microscope and a 63x/1.4 NA
246 oil objective (Leica HC PL APO 63x/1,40 OIL CS2) in “Lightning” mode (in LasX 4.6) set
247 at high resolution grade, which reduces the pinhole size to 0.5 Airy units. Laser and
248 emission settings were identical to those used the previous section that described
249 quantification of active caspase-3 signal in mTurquoise2-labeled dLGNs. 3D image

250 stacks (31.5 um x 31.5 um x 12 um) were acquired at high voxel density (43 nm x 43 nm
251 x 204 nm) in photon counting mode and 4x signal accumulation. Subsequently, the
252 images were processed by iterative deconvolution using a theoretical point spread
253 function informed by the imaging parameters of the microscope and constrained by an
254 "Adaptive" strategy that accounts for local background and signal-to-noise ratio
255 information.

256 Confocal images of MAP2 and active caspase-3 signals in dLGN (Figure S4A)
257 were similarly imaged on a Leica Stellaris 8 microscope with a 63x/1.4 NA oil objective
258 (Leica HC PL APO 63x/1,40 OIL CS2). A 653 nm laser line and an emission read of 662
259 nm – 829 nm were used for caspase-3 channel, and a 499 nm laser line and an emission
260 read of 504nm – 549 nm were used for Map2 channel. The channels were acquired
261 simultaneously at voxel densities of 65 nm x 65 nm x 299 nm. NeuN and active caspase-
262 3 signals in dLGN (Figure S4C) were imaged using a 20x/0.7 NA water objective (Leica
263 HC PL APO 20x/0,7 IMM CORR CS2). A 590 nm laser and an emission read of 595 nm
264 – 750 nm were used for imaging caspase-3 and a 499 nm laser with a 509 nm - 595 nm
265 emission read was used for the NeuN signal. The channels were acquired sequentially
266 (active caspase-3 first) at pixel densities of 142 nm x 142 nm.

267 **Measuring overlap of eye-specific territories in dLGN**

268 For comparison between Casp3$^{+/+}$ and Casp3$^{-/-}$ animals (Figure 3), Casp3$^{+/-}$ males
269 were bred to Casp3$^{+/-}$ females to generate Casp3$^{+/+}$ and Casp3$^{-/-}$ littermate pups. Pups
270 were genotyped at birth. Before intraocular injection, lyophilized CTB-AF488 and CTB-
271 AF594 powders were reconstituted in 1% DMSO in PBS^{-} to a final concentration of 5
272 mg/ml. CTB solutions were aliquoted and stored at -20 °C for later use. Thawed CTB

273 solutions were discarded after each surgery. Intraocular injection of CTB-AF solutions
274 was performed at the age of P9 as described above. CTB-AF488 was injected into left
275 eyes and CTB-AF594 into right eyes. 24 hours after the injection, brains of P10 pups were
276 harvested, and 50 um thick coronal sections prepared as described above.

277 Cured sections were imaged on a Zeiss AxioObserver Z.1 microscope equipped
278 with an LSM 880 Airy scan detector and an EC Plan-Neofluar 10x objective (NA = 0.3). A
279 488 nm laser and a 499-544 nm detection window were used for CTB-AlexaFlour488,
280 and a 594 nm laser and a 597-659 nm detection window were used for CTB-
281 AlexaFlour594. Signals from the two channels were acquired sequentially into 16-bit
282 images with a 0.4 μm x 0.4 μm pixel size. Laser power and detector gain settings were
283 maintained at the same level for most images, with occasional adjustment to avoid
284 saturation. One image per dLGN per section was acquired.

285 To quantify the overlap between contralateral-specific and ipsilateral-specific
286 territories in the dLGN, we selected 7-8 sections per animal that span the majority of left
287 dLGN of and analyzed their images in ImageJ. For each image, a mask for the entire
288 dLGN region and a mask for a background region in the thalamus with no labeling were
289 manually created. Background signal from each channel was estimated as the average
290 signal in the background region and was subtracted from signals in the dGLN region.
291 Then the background-subtracted signals in the dLGN region were normalized to between
292 0 and 1 for each image and each channel. We picked 7 increasing cutoff thresholds (0.1,
293 0.125, 0.15, 0.175, 0.2, 0.225, and 0.25), and for each threshold and each channel,
294 signals that are greater than or equal to the threshold were considered real signals. For
295 each animal (corresponding to 7-8 images of left dLGN) and each threshold, we

296 calculated percentage overlap as the ratio between the total number of pixels with real
297 signals in both channels in all images and the total number of pixels in the entire dLGN
298 region of all images. We plotted the percentage overlap as a measurement of segregation
299 of eye-specific territories in dLGN. Similar analyses were performed on right dGLN
300 images yielding similar results.

301 For overlap analysis presented in Figure S3, E15 mouse embryos were injected in
302 their right eyes either with AAV carrying hSyn-mTurqouise2 (control group) or a 1:1
303 mixture of AAV carrying hSyn-TeTxLC-P2A-mTurqouise2 and AAV carrying hSyn-
304 mTurquoise2 (inactivation group). The left eyes of both groups of mice were injected with
305 AAV carrying the hSyn-tdTomato. At P8, brains from both groups were harvested, and 50
306 μm thick coronal sections were prepared as described above. Only animals that had well
307 labeled dLGNs on both sides were selected for analysis. Mounted and cured sections
308 containing dLGN were imaged in confocal mode on a Leica Stellaris 8 microscope using
309 a 10x/0.4 NA dry objective (Leica HC PL Apo CS2 10x/0.4 dry). A 441 nm laser and a
310 445-548 nm detection window were used for the mTurquoise2 channel, and a 554 nm
311 laser and a 564-721 nm detection window were used for tdTomato channel. The images
312 were acquired at 8-bit depth with a 0.227 μm x 0.227 μm pixel size (at 1 Airy unit for
313 $\lambda = 580$ nm) and at a laser power, pixel dwell time, and signal accumulation sufficient to
314 avoid detector (Power HyD S in counting mode) saturation. One image per dLGN per
315 section was acquired. For each animal, overlap was measured as described above on
316 the left dLGN (the side where mTurquoise2 signal occupied the majority of the dLGN) by
317 averaging from 3 to 5 consecutive sections. The cutoff thresholds used were: 0.050, 0.075,
318 0.1, 0.125, 0.15, 0.175, 0.2.

319 For overlap analysis presented in Figure S5, embryos in the control group were
320 injected at E15 with AAV carrying tdTomato construct in the left eyes, and with AAV
321 carrying the CAG-GFP construct in the right eyes. Embryos in the dual inactivation group
322 were injected at E15 with a mixture (1:1) of AAV carrying hSyn-tdTomato construct and
323 AAV carrying hSyn-TeTxLC-P2A-mTurquoise2 construct in their left eyes, and with a
324 mixture (1:1) of AAV carrying the CAG-GFP construct and AAV carrying the hSyn-TeTxLC-
325 P2A-mTurquoise2 construct in their right eyes. At P10, the brains were harvested and
326 sectioned as described above. Confocal images of dLGN were acquired on a Leica
327 Stellaris 8 microscope using a 10x/0.4 NA dry objective (Leica HC PL Apo CS2 10x/0.4
328 dry). A 488 nm laser line with a 488 nm notch filter and a 485-559 nm detection window
329 were used for the GFP channel, and a 554 nm laser and a 559-701 nm detection window
330 were used for the tdTomato channel in sequential line mode to avoid any cross-excitation
331 (with tdTomato channel acquired first). The images were acquired at 12-bit depth with a
332 0.248 μm x 0.248 μm pixel size (at 1 Airy unit for $\lambda = 580$ nm) and at a laser power, pixel
333 dwell time, and signal accumulation that avoided detector (Power HyD S in counting mode)
334 saturation. One image per dLGN per section was acquired. For each animal overlap was
335 measured as described above on the right dLGN (the side where tdTomato signal
336 occupied the majority of the dLGN) by averaging from 5 consecutive sections.

337 **Quantification of RGC densities in the retina**

338 To estimate the density of RGCs in the retina (Figure S6), retinae of P10 *Casp3*$^{+/+}$
339 and *Casp3*$^{-/-}$ mice were harvested and stained with anti-RBPMS antibody as described
340 above. We imaged 4 large square regions of interest (1.16 mm x 1.16 mm) in each retina
341 on four sides of the optic disc. The images were acquired with a Leica TCS SP8 Laser

342 Scanning Microscope using the 10x/0.4 NA dry objective (Leica HC PL Apo CS2 10x/0.4
343 dry), a 594 nm laser line, and an emission window of 607 nm to 694 nm, at a pixel
344 sampling of 302 nm x 302 nm. To account for tissue unevenness, we collected a stack of
345 3 Z-slices (2.4 μm apart). To count RGCs, we sampled 3 subregions of a size of 100 μm^2
346 from each large region of interest. The subregions were selected to be at similar distances
347 from the optic disc and in areas devoid of tissue tears. Cells were modeled to spots by
348 fitting them to ellipsoid objects (XY size = 8 μm; Z size = 16 μm, with background
349 subtraction) in Imaris 9.6 (Oxford Instruments). Densities of spots for each region were
350 averaged and reported as number of RGC per 100 μm^2 of retina.

351 **Whole-cell patch-clamp recording in acute brain slices**

352 To characterize electrophysiological properties of retinogeniculate synapses in
353 *Casp3*$^{+/+}$ and *Casp3*$^{-/-}$ mice (Figure 4), the mice (aged p28 – p32) were decapitated under
354 deep isoflurane anesthesia, and the brain was removed and quickly transferred to an ice-
355 cold dissection solution containing (in mM): 194 sucrose, 30 NaCl, 2.5 KCl, 1.2 NaH2PO4,
356 26 NaHCO3, 10 D-Glucose, 1 MgCl2 (pH 7.4, oxygenated with 95% CO2 and 5% O2).
357 Parasagittal brain slices containing the optic tract and dLGN were prepared using a
358 vibratome (Leica VT 1200S) as previously described (*5, 6*). The slices were recovered at
359 35.5°C in an incubation chamber (BSC-PC, Warner Instrument, USA) filled with artificial
360 cerebrospinal fluid (ACSF) containing (in mM): 124 NaCl, 2.5 KCl, 1.2 NaH2PO4, 26
361 NaHCO3, 10 D-Glucose, 2 CaCl2, 1 MgCl2 (pH 7.4, oxygenated with 95% CO2 and 5%
362 O2, osmolarity ~310). After ~30 minutes of recovery, the chamber was maintained at room
363 temperature.

364 All recordings were performed with a MultiClamp 700B amplifier (Molecular
365 Devices) and signals were filtered at 2 kHz and digitized at 20 kHz with via USB-6343
366 (National Instruments) under the control of WaveSurfer software
367 (https://wavesurfer.janelia.org). All recordings were carried on slices submerged in the
368 recording chamber of an upright microscope (BX61WI; Olympus, Tokyo, Japan) equipped
369 with IR-DIC (infrared-differential interference contrast) microscopy and a water-immersion
370 objective lens (60X, 1.00 NA; Olympus). Slices were maintained under continuous
371 perfusion of oxygenated ACSF at 29-30°C. Patch pipettes were pulled from thin-wall
372 single-barrel borosilicate glass (TW150-6, WPI), resulting in electric resistance of 2 ~ 5
373 MΩ when filled with an intracellular solution contained the following (in mM): 120 cesium
374 methane sulfonate, 5 NaCl, 10 tetraethylammonium chloride, 10 HEPES, 4 lidocaine N-
375 ethyl bromide, 1.1 EGTA, 4 magnesium ATP, and 0.3 sodium GTP, with pH adjusted to
376 7.2 with CsOH and osmolality set to ~290 mOsm.

377 Whole-cell voltage-clamp recordings of relay neurons in the dLGN were performed
378 as previously described (Figure 4A-C) (*6*). The slices were submerged in ACSF
379 containing 20 uM bicuculline to inhibit $GABA_A$ receptors, and a bipolar concentric
380 stimulation electrode (FHC) was placed on the surface of the optic tract to deliver stimuli
381 with intensities ranged from 0 – 100 μA (200us duration) with an inter-trial interval of 40 –
382 60 s. In the whole-cell configuration (series resistance < 20 MΩ), the membrane potential
383 of the neuron was clamped at -70 mV to measure evoked excitatory postsynaptic current
384 (EPSC) mediated by activation of AMPA receptors, and then at +40 mV to measure
385 evoked EPSC mediated by activation of NMDA receptors. The stimulus intensity was
386 systemically increased until a response to the stimulus was observed, and then was

387 reduced to a previous level where no response was detected. From that level, the stimulus
388 intensity was increased by 0.5 μA steps to recruit single inputs which were putative single
389 fiber (SF) amplitudes. When the EPSC amplitude reached a plateau, it was considered a
390 putative maximum response. If the EPSC amplitude dropped while the stimulation
391 intensity increased, data from that relay neuron was discarded.

392 To measure paired pulse ratio (PPR) (Figure 4D-E), the slices were submerged in
393 the ACSF containing 20 uM bicuculline and 50 uM cyclothiazide to inhibit AMPAR
394 desensitization, and the stimulation electrode was placed on the optic tract. In the whole-
395 cell configuration, the membrane potential was clamped at -70 mV. After confirming the
396 stimulation intensity that evoked the maximum response, two consecutive electrical
397 stimuli of that intensity (300 μs duration) were delivered at 50, 150, 250, 500, and 1000
398 ms inter-stimulus intervals. Each pair of stimuli constitutes one trial, and two consecutive
399 trials were separated by an interval of 40 s. For each inter-stimulus interval, two trials
400 were performed and averaged. PPR was calculated as the maximum amplitude of the
401 second EPSC over the maximum amplitude of the first EPSC. If in any trial except for the
402 first trial the first EPSC dropped significantly in amplitude compared to the first EPSC of
403 the first trial, data from that dLGN relay neuron was discarded.

404 **Measuring microglia- and astrocyte-mediated synapse engulfment *in vivo***

405 To measure microglia-mediated synapse engulfment *in vivo* (Figure 5 and Figure
406 S10), we bred *Casp3*$^{-/-}$ males to *Casp3*$^{+/-}$; *Cx3ct1-Gfp*$^{+/-}$ females to generate *Casp3*$^{-/-}$;
407 *Cx3ct1-Gfp*$^{+/-}$ and *Casp3*$^{+/-}$; *Cx3ct1-Gfp*$^{+/-}$ littermate pups. To measure astrocyte-
408 mediated synapse engulfment *in vivo* (Figure S11), we bred *Casp3*$^{-/-}$ males to *Casp3*$^{+/-}$;
409 *Aldh1l1-Gfp*$^{+/-}$ to generate *Casp3*$^{-/-}$; *Aldh1l1-Gfp*$^{+/-}$ and *Casp3*$^{+/-}$; *Aldh1l1-Gfp*$^{+/-}$ littermate

410 pups. P4 pups with desired genotypes were injected with 2 μL of CTB-AF555 in left eyes
411 and 2 μL of CTB-AF647 in right eyes as described above. 24 hours later, the brains were
412 harvested, sectioned, and mounted as described above.

413 To analyze engulfment of synapses, the sections were imaged using a Leica TCS
414 SP8 Laser Scanning Microscope equipped with an HC Plan Apo CS2 40x (NA = 1.3) oil
415 objective and a White Light Laser Unit. The 3D multichannel stacks with a voxel size of
416 0.075 x 0.075 x 0.312 μm for microglia samples or 0.048 x 0.048 x 0.2 μm for astrocytes
417 samples were acquired as 16-bit images with 4x line averages for microglia or 2x for
418 astrocytes at 400 Hz scanner speed. The stacks were set to collect a volume of 20
419 micrometers in the Z dimension and 387.5 micrometers in XY dimensions for microglia or
420 288 μm in XY for astrocytes. The pinhole was set at 1 Airy unit for 520 nm
421 wavelength. The excitation lasers and detection windows were set to minimize crosstalk
422 and bleed-through as well as the saturation of detectors while simultaneously imaging the
423 three channels. A 478 nm laser and a detection window of 488 nm – 537nm were used
424 for the GFP channel, a 550 nm laser and a detection window of 596 nm – 629 nm were
425 used for CTB-AF555, and a 651 nm laser and a detection window of 665 nm to 750 nm
426 were used for CTB-AF647. Imaris 9.6 (Oxford Instruments) was used to segment
427 microglia, astrocytes, ipsilateral RGC axon terminals, and contralateral RGC terminals
428 from the 3D stacks using the Surface Creation module with background subtraction. For
429 segmentation of RGC axon terminals and astrocytes, all parameters used were left at
430 default values (auto). For segmentation of microglia, we set the threshold manually at the
431 highest inflection curve in the histogram of voxel intensities, which in our experience
432 provided a good trade-off for good segmentation of cell bodies and major processes while

433 keeping the adjustment consistent across different image datasets. A background
434 subtraction ball size of 1 μm was used for microglia, a ball size of 1.4 μm was used for
435 astrocytes, and a ball size of 0.5 μm was used for AF555 and AF647 labeled axonal
436 materials. The segmented signal of AF555 and AF647 was each converted to a binary
437 mask of 0 and 1 voxels. Finally, the sum of the segmented volume (i.e. sum of ones) of
438 AF555 and or AF647 in each microglia or astrocyte was either directly plotted or
439 normalized to the microglia or astrocyte volume and plotted. To control the inherent signal
440 variability across LGN, only microglia and astrocytes present in the ipsilateral region of
441 the 3 middle sections of the left dLGN of each mouse were included in the analysis. Also,
442 only microglia or astrocytes whose soma and proximal processes were contained in the
443 volumetric stack were included in the final analysis. All littermate pups of the same
444 genotype were pooled together.

445 **Measuring activity-dependent engulfment of synapses by microglia**

446 To investigate the role of caspase-3 in activity-dependent synapse elimination
447 (Figure 6 and Figure S12), we used C57Bl/6J wildtype mice as controls and bred *Casp3*$^{-}$
448 $^{/-}$ males with *Casp3*$^{+/-}$ females to generate *Casp3*$^{-/-}$ mice. Note that C57Bl/6J and *Casp3*$^{-/-}$
449 mice used in this experiment are not littermates and should not be directly compared with
450 each other. C57Bl/6J and *Casp3*$^{-/-}$ embryos were injected at E15 in their right eye either
451 with AAV carrying hSyn-TeTxLC-P2A-mTurqouise2 or AAV carrying hSyn-mTurquoise2
452 as described above. To label the RGC axons, at P4, the pups were injected with 2 μL of
453 CTB-AF555 in left eyes and 2 μL of CTB-AF647 in right eyes as described above. At P5,
454 the brains were harvested and sectioned. Two 50 μm sections that spanned the central

455 part of the dLGN were stained with anti-Iba1 antibody and goat anti-rabbit AF488
456 secondary (as described above) to label microglial cell bodies.

457 Mounted and cured sections were then imaged on Leica Stellaris 8 confocal
458 microscope using a 63x/1.4 NA oil objective (Leica HC PL APO 63x/1,40 OIL CS2). Four
459 stitched 3D-stacks were acquired for each left dLGN (the side where CTF-AF647 and
460 mTurquoise2 occupied the majority of the dLGN) to generate a 3D volume of 366 μm x
461 366 μm in XY and approximately 20 μm in the Z dimension, with a voxel size of 64 nm x
462 64 nm x 299 nm. The channels were acquired sequentially: first using a 499 nm laser with
463 an emission window of 507-556 nm together with a 653 nm laser with an emission window
464 of 663-750 nm for Iba1-AF488 and CTB-AF647 signal, respectively, then using a 553 nm
465 laser with an emission window of 558-663 nm for the CTB-AF555 signal. Images acquired
466 were collected as 12-bit datasets, and care was taken to set the laser power, signal
467 accumulation, and pixel dwell time to avoid detector saturation. Only animals whose
468 dLGN areas were fully labeled with both AF555 and AF647 as well as the mTurquoise
469 signals were imaged and analyzed. Animals in which CTB signal appeared widespread
470 throughout the brain parenchyma were excluded from the analysis as these labeling
471 patterns were likely due to surgical mistargeting or issues with tissue integrity.

472 To segment volumes corresponding to microglia and CTB-AF555 and CTB-AF647
473 labeled RGC axon terminals, we utilized the Surface Creation module with machine
474 learning segmentation of Imaris 10.1.1 (Oxford Instruments). We first trained for several
475 rounds a pixel classifier for each channel using two independent image files and saved
476 the classifiers along with the other settings (smoothing grain size of 100 nm and
477 discarding volumes smaller than 10 voxels) as “Favorite Creation Parameter”.

478 Subsequently, the same Favorite Creation Parameters were applied to all data sets, with
479 the rare instances when microglia segmentation was slightly tuned via the same pixel
480 classier to better capture some of the cell border areas. Similar to the previous analyses
481 (Figure 5), the segmented signals of CTB-AF647 and CTB-AF555 were converted to
482 binary images (0 or 1 voxels), and the total volume of CTB-AF647- or CTB-AF555-positive
483 voxels in each microglia was extracted, converted to fraction of the microglia volume, and
484 plotted. Only the cells whose body and major processes were bound within the 3D stack
485 and present within the middle area of dLGN (where the ipsilateral signal is present) were
486 included in the analysis. Data from the same genotype and treatment were pooled
487 together. Either one or two sections were analyzed for each animal.

488 **Measuring microglia activation**

489 To measure if lack of caspase 3 causes microglia activation (Figure S9), we bred
490 *Casp3*$^{+/-}$ males with *Casp3*$^{+/-}$ females to generate *Casp3*$^{-/-}$ and Casp3$^{+/+}$ littermates. After
491 genotyping, at P5, the brains were harvested and sectioned coronally as described above.
492 Two 50 μm sections that spanned the central part of the dLGN were stained with anti-
493 Iba1 antibody (detected by goat anti-rabbit AF488 secondary) to label microglial cell
494 bodies and anti-CD68 antibody (detected by donkey anti-rat AF555 secondary) to detect
495 CD68 protein. Mounted and cured sections were imaged on Leica Stellaris 8 confocal
496 microscope using a 63x/1.4 NA oil objective (Leica HC PL APO 63x/1,40 OIL CS2). A 3D
497 image stack of 185 μm x 185 μm in XY and approximately 20 μm in the Z dimension, with
498 a voxel size of 72 nm x 72 nm x 299 nm was acquired for each dLGN. The channels were
499 acquired in photon counting mode simultaneously: a 499 nm laser with an emission
500 window of 504-548 nm together with a 553 nm laser with an emission window of 560-650

501 nm for Iba1-AF488 and CD68-AF555. To eliminate any fluorescence emission bleed-
502 trough between channels, the photon arrival times were gated to 3 - 5 ns for Iba1-AF488
503 and to 0 - 1.5 ns for Iba1-AF555 channels, respectively. Images acquired were collected
504 as 8-bit datasets, and care was taken to set the laser power, signal accumulation, and
505 pixel dwell time to avoid fluorophore bleaching or detector saturation.

506 For segmentation of microglia and CD68 signals, we utilized the Surface Creation
507 module with machine learning segmentation of Imaris 10.1.1 (Oxford Instruments). We
508 first trained for several rounds a pixel classifier for each channel then saved the classifiers
509 along with the other settings (smoothing grain size of 145 nm and discarding volumes
510 smaller than 10 voxels) as “Favorite Creation Parameter”. Subsequently, the same
511 Favorite Creation Parameters were applied to all data sets, with the rare instances when
512 microglia segmentation was slightly adjusted via the same pixel classier to better capture
513 some of the cell border areas. Similar to the previous analyses (Figure 5), the segmented
514 signals of CD68-AF555 were converted to binary images (0 or 1 voxels), and the total
515 volume CTB-AF555-positive voxels in each microglia was extracted, converted to fraction
516 of the microglia volume, and plotted. For measurement of relative CD68 intensity, the sum
517 of CD68 signal was divided by the microglia volume. Only the microglia whose body and
518 major processes were confined within the 3D stack were included in the analysis. All
519 staining, imaging and analysis parameters were identically applied to all sections. Two
520 sections were analyzed for each animal. Data from the same genotype and were pooled
521 together.

522

523 **Characterization of *App/Ps1* transgenic mice**

524 To detect Aβ deposition (Figure S13A), brains of 6 month-old female *App/Ps1*$^{-/-}$
525 mice, 5 month-old and 6 month-old male and female *App/Ps1*$^{+/-}$ mice, and 6 month-old
526 female *Casp3*$^{-/-}$; *App/Ps1*$^{+/-}$ mice were harvested, sectioned, and stained with Thioflavin
527 S as described above. Stained sections were imaged on a Leica Stellaris 8 microscope
528 using a 10x/0.4 NA dry objective (Leica HC PL Apo CS2 10x/0.4 dry). A 460 nm laser line
529 was used for excitation and a window of 469 nm - 600 nm was used for emission. Tile
530 images (pixel size: 284nm x 284 nm) were collected and merged into one image spanning
531 an entire coronal section in Las X 4.6 Navigator. To quantify the level of amyloid deposition
532 in 6 month-old female *App/Ps1*$^{+/-}$ and *Casp3*$^{-/-}$; *App/Ps1*$^{+/-}$ mice (Figure S13B), the
533 number of Thioflavin S-positive plaques was manually counted in a total of 3 sections per
534 animal and averaged.

535 To investigate the role of caspase-3 in Aβ-induced synapse loss (Figure 7), *Casp3*$^{-}$
536 $^{/-}$ mice were bred to *App/Ps1*$^{+/-}$ mice to create *Casp3*$^{-/-}$; *App/Ps1*$^{-/-}$ and *Casp3*$^{-/-}$; *App/Ps1*$^{+/-}$
537 mice. Brains of 6 month-old female *App/Ps1*$^{-/-}$ and *App/Ps1*$^{+/-}$ littermates as well as *Casp3*$^{-}$
538 $^{/-}$; *App/Ps1*$^{-/-}$ and *Casp3*$^{-/-}$; *App/Ps1*$^{+/-}$ littermates were harvested, sectioned, and stained
539 with anti-SV2 antibody (conjugated to AF546) and anti-Homer1 antibody (using goat anti-
540 rabbit AF647 as the secondary) to label presynaptic and postsynaptic compartments,
541 respectively. Stained sections were imaged on a Leica Stellaris 8 confocal microscope
542 using a 63x/1.4 NA oil objective (Leica HC PL APO 63x/1,40 OIL CS2). To acquire a
543 representative dataset, we focused on the molecular layer of the dentate gyrus of the
544 hippocampus from both the left and right side of the brain and sampled 3 regions from
545 each side, as shown in Figure S14. 3D-stacks (61.5 μm x 61.5 μm x 20 μm) were acquired
546 with a voxel size of 64 nm x 64 nm x 298 nm. 561 nm and 638 nm laser lines were used

547 for excitation, 555 nm – 635 nm and 642 nm – 792 nm windows were used for emission
548 reading, and appropriate notch filters were used for blocking the exciting laser lines. The
549 channels were acquired as 8-bit data sets with detectors set in counting mode, and the
550 lasers power, signal accumulation, and pixel dwell time set at levels that avoided detector
551 saturation. To measure synapse number per unit volume, we first trimmed the raw 3D
552 stacks to a stack of approximately 3.5 μm thickness on the side closest to the coverslip
553 (to avoid any signal depletion the middle part of the section due to antibody penetration
554 issues) and cropped out regions where large gaps (corresponding to blood vessels)
555 devoid of Sv2 or Homer1 staining were present. The punctate signals of SV2 and Homer1
556 were fit in Imaris 10.1 (Oxford Instruments) to ellipsoids (500 nm in XY and 850 nm in Z
557 for SV2; 400 nm in XY and 800 nm in Z for Homer1) with background subtraction ("Spot
558 Creation"). Then we designated as "synapses" all Homer1 ellipsoids that were within 300
559 nm of a SV2 ellipsoid (center-to-center distance). For each animal, the total number of
560 synapses in all 3D-stacks analyzed was divided by the total volume of all stacks analyzed
561 and plotted as a single value.

562 To detect Aβ-induced microglia activation (Figure S16), brains of 6 month-old
563 female *App/Ps1*$^{-/-}$, *App/Ps1*$^{+/-}$, and *Casp3*$^{-/-}$; *App/Ps1*$^{+/-}$ mice were harvested, sectioned,
564 and stained with anti-Iba1 antibody (using goat anti-rabbit AF647plus as the secondary)
565 and anti-Cd68 (using goat anti-rat AF555plus as the secondary) as labels of microglia cell
566 body and microglial activation, respectively. Stained sections were imaged on a Leica
567 Stellaris 8 confocal microscope using a 20x/0.7 NA water objective (Leica HC PL APO
568 20x/0,7 IMM CORR CS2). Tile images spanning the hippocampus were acquired at voxel
569 sizes of 142 nm x 142 nm x 300 nm. A 548 nm laser line and a 554 nm – 634 nm emission

570 window were used for the CD68-AF555 channel, and a 653 laser line and a 663 nm –
571 748 nm emission window were used for the Iba1-AF647 channel. Microgliosis could be
572 detected as clusters of microglia with stubby processes and strong intracellular Cd68
573 signals (Figure S16).

574 To quantify Aβ-induced caspase-3 activity (Figure S17), brains of 4 month-old, 5
575 month-old and 6 month-old female *App/Ps1*$^{-/-}$ and *App/Ps1*$^{+/-}$ littermates were harvested,
576 sectioned, and stained with anti-cleaved caspase-3 antibody (using goat anti-rabbit
577 AF555plus as the secondary). Stained sections were imaged on a Leica Stellaris 8
578 confocal microscope using a 63x/1.4 NA oil objective (Leica HC PL APO 63x/1,40 OIL
579 CS2). We sampled at least 2 regions of interest from the molecular layer of the dentate
580 gyrus of the hippocampus on each side of the brain. 3D-stacks (92.26 μm x 92.26 μm x
581 22 μm) were acquired with a voxel size of 81 nm x 81 nm x 299 nm. A 561 laser line was
582 used for excitation and an emission window of 550 nm – 728 nm was used for the active
583 caspase-3 channel. To measure the number of caspase 3 objects in the dataset, we first
584 trimmed the 3D stacks to a volume where the signal is uniformly distributed (i.e. in focus)
585 and segmented the objects using the "Surface creation" analysis in Imaris 10.1 (Oxford
586 Instruments). The dataset was first smoothed by a two-pixel filter, then a ball size of 400
587 nm was used to find the objects with background subtraction. Only objects bigger than 10
588 and smaller than 2000 voxels were kept. Finally, the number of caspase 3 objects was
589 divided by the volume of the 3D stack analyzed and reported per brain side (left or right)
590 for each animal.

591 To measure the relative density of granule cells in the dentate gyrus (Figure S16), brains
592 of 6 month-old female *App/Ps1*$^{-/-}$, *App/Ps1*$^{+/-}$, *Casp3*$^{-/-}$; *App/Ps1*$^{-/-}$, and *Casp3*$^{-/-}$; *App/Ps1*$^{+/-}$

593 mice were harvested, sectioned, and stained with anti-NeuN antibody (using goat anti-
594 mouse AF594plus as the secondary) to label neuronal nuclei. Stained sections were
595 imaged on a Leica Stellaris 8 confocal microscope using a 20x/0.7 NA water objective
596 (Leica HC PL APO 20x/0,7 IMM CORR CS2). 3D stacks of the dentate gyrus (581 μm x
597 581 μm x 30 μm) were acquired at voxel sizes of 160 nm x 160 nm x 1000 nm for each
598 section and side (left and right) using a 594 nm laser and an emission window of 597 nm
599 to 750 nm. The channels were acquired as 8-bit images with the detector set in counting
600 mode, and the lasers power, signal accumulation, and pixel dwell time set at levels that
601 avoided detector saturation. To count the number of nuclei, images were first rotated to
602 position vertically the cortical side of the dentate gyrus. A maximum projection of the
603 brightest two Z-slices was extracted from each 3D stack, and NeuN+ nuclei were
604 manually counted within a rectangular region of interest (89 μm x 150 μm) that was
605 positioned on the granule cell layer at 300 μm away from the tip of the gyrus.

606 **References**:

607 1. J. Goedhart *et al.*, Structure-guided evolution of cyan fluorescent proteins towards a
608 quantum yield of 93%. *Nat Commun* **3**, 751 (2012).
609 2. D. Grimm *et al.*, In vitro and in vivo gene therapy vector evolution via multispecies
610 interbreeding and retargeting of adeno-associated viruses. *J Virol* **82**, 5887-5911
611 (2008).
612 3. M. Yasuda, S. Nagappan-Chettiar, H. Umemori, In utero intraocular AAV injection for
613 early gene expression in the developing rodent retina. *STAR Protoc* **2**, 100742 (2021).

4. J. D. M. Arzt, C. Schmied, T. Pietzsch, D. Schmidt, P. Tomancak, R. Haase, F. Jug, LABKIT: Labeling and Segmentation Toolkit for Big Image Data. *Frontiers in Computer Science* **4**, (2022).

5. J. P. Turner, T. E. Salt, Characterization of sensory and corticothalamic excitatory inputs to rat thalamocortical neurones in vitro. *J Physiol* **510 (Pt 3)**, 829-843 (1998).

6. C. Chen, W. G. Regehr, Developmental remodeling of the retinogeniculate synapse. *Neuron* **28**, 955-966 (2000).